BETA-DECAY STUDIES OF ^{78}Ni AND OTHER NEUTRON-RICH NUCLEI IN THE ASTROPHYSICAL R-PROCESS

By

Paul Thomas Hosmer

A DISSERTATION

Submitted to
Michigan State University
in partial fulfillment of the requirements
for the degree of

DOCTOR OF PHILOSOPHY

Department of Physics and Astronomy

2005

ABSTRACT

BETA-DECAY STUDIES OF ^{78}Ni AND OTHER NUCLEI IN THE ASTROPHYSICAL R-PROCESS

The β-decay properties of several neutron-rich nuclei including the doubly-magic ^{78}Ni were studied. A low-energy neutron detector NERO was designed and calibrated for use in these measurements. β-decay measurements, especially those that combine both half-life and neutron-emission probability measurements, can offer first tests of nuclear theories of neutron-rich nuclei. In addtion, ^{78}Ni is an important waiting-point in the astrophysical r-process. The results of the measurements are compared to several nuclear models, and the astrophysical implications are explored.

By

Paul Thomas Hosmer

for my family

ACKNOWLEDGMENTS

I would like to thank my collaborators at Notre Dame, University of Mainz, and University of Maryland. Karl-Ludwig Kratz, Bernd Pfeiffer, Bill Walters, Paul Reeder, and Andreas Woehr have been very helpful and always willing to sit down and discuss things.

I would like to thank the entire Notre Dame Nuclear Structure Laboratory for their time and assistance. They are both professional and fun.

I would like to thank the staff at the NSCL for all of the help and advice. Some of these people include Len Morris, Jeanine Honke, Dave Sanderson, John Yurkon, Barb Pollack.

The A1900 people have always been extremely helpful, both during experiments and with any other questions and problems: Andreas Stolz, Mattias Steiner, Tom Ginter have always done above and beyond.

I would like to thank the NSCL professors for their advice and help. They have always had an open door. I would particulary like to thank Bill Lynch and Betty Tsang for treating me and the other group members like family.

I would like to thank Paul Mantica. He and his entire group have always been extremely helpful and a pleasure to work with during experiments.

I would like to thank my committee members for their time and willingness to put up with meetings and shifting schedules.

I would like to thank my advisor Hendrik Schatz for his advise and help on all matters.

I would like to thank all my group members, especially: Thom Eliott, Fernando Montes, Alfredo Estrade.

I would like to thank my fellow graduate students, including, but not limited to, Mark Wallace, Michael Crosser, Bill Peters and Michal Mocko.

Contents

List of Figures

List of Tables

Chapter 1

Introduction

1.1 Neutron-rich Nuclei and the Doubly-magic ^{78}Ni

This work studies the β-decay properties of the neutron-rich nuclei around the doubly-magic nucleus ^{78}Ni. Doubly-magic nuclei with completely filled proton and neutron shells are of fundamental interest in nuclear physics. The simplified structure of these nuclei and their direct neighbors allows one to benchmark key ingredients in nuclear structure theories such as single-particle energies and effective interactions. Doubly-magic nuclei also serve as cores for shell model calculations, dramatically truncating the model space, thus rendering feasible shell model calculations in heavy nuclei. In this way, neutron-rich doubly-magic nuclei such as ^{132}Sn and ^{78}Ni serve as "launching points" to extend shell-model calculations to neutron-rich nuclei [1].

In addition to the magic ^{78}Ni, β-decay measurements of neutron-rich nuclei in general can offer first tests of nuclear theories that try to predict the changing nuclear structure as one moves farther from stability toward the neutron drip-line.

1.2 Astrophysical Significance

Neutron rich nuclei play a central role in the astrophysical rapid neutron-capture process (r-process) [2,3]. The r-process is a rapid neutron-capture process that occurs in an environment of large neutron flux were nuclei can experience neutron captures faster than the competing β-decay even for very neutron-rich nuclei. Within an isotopic chain, photodisintigration competes against neutron capture and according to the waiting-point approximation, an (n,γ),(γ,n) equillibrium is established. In this situation, most of the abundance within an isotopic chain is concentrated on one nucleus. The relative abundances are determined by the Saha Equation:

$$\frac{Y(Z,A+1)}{Y(Z,A)} = n_n \frac{G(Z,A+1)}{2G(Z,A)} \left(\frac{A+1}{A}\frac{2\pi\hbar^2}{m_u kT}\right)^{3/2} exp\left(\frac{S_n}{kT}\right) \tag{1.1}$$

where $Y(Z,A)$ is the abundance of nucleus with proton number Z and mass number A, G are the partition functions, T is the temperature, and S_n is the neutron separation energy. The process must then wait for this nucleus (called a waiting-point) to β-decay to the next isotopic chain, where again the (n,γ),(γ,n) equillibrium is established, and so the process moves up to heavier elements. This process will continue until the neutron flux diminishes, at which point the exotic nuclei will decay back to stability by β-decay and β-delayed neutron emission. In the waiting-point approximation, neutron-capture rates and photodisintigration rates are not required. Only the neutron separation energies of the isotopic chain, the β-decay half-lives of the waiting-point nuclei, and the P_n values of the nuclei between the r-process path and stability are required to understand the process (see Figure 1.1).

The r-process process produces roughly half the elements heavier than iron, yet its astrophysical site is still unknown. A leading candidate for the astrophysical site is the neutrino-driven wind off a hot, newborn neutron star following core-collapse supernovae [4]. While this site has the r-process starting around $A = 90$, with lighter nuclei being produced as less neutron-rich species in an α-rich freeze-out thereby

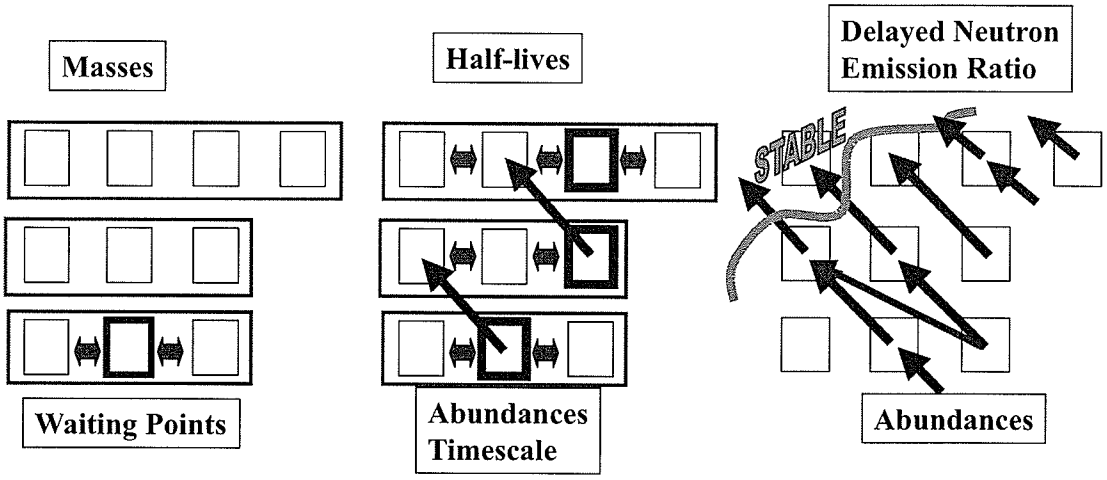

Figure 1.1: The r-process in the waiting-point approximation. The masses (S_n) determine the waiting points and define the r-process path. The half-lives of the waiting points affect the time-scales and the final abundances. The P_n values modify the abundances after freeze-out by shifting on mass unit per neutron emission.

rendering nuclei in the region around ^{78}Ni less significant, the site exhibits several problems. The α-rich freeze-out fails to accurately reproduce the observed abundances for nuclei with $A = 80-90$ [5], and the corresponding r-process itself is unable to produce sufficient amounts of the heaviest r-process nuclei around A =195 [6].

Several r-process scenarios try to address these problems. Examples of these scenarios include models that assume nonstandard neutron star masses [7], or that are based on a supernova triggered by the collapse of an ONeMg core in an intermediate mass star [8]. In these scenarios, neutron-capture process begins at lighter nuclei, and ^{78}Ni becomes an important r-process waiting point.

In addition, recent observations of the element abundances produced by single (or very few) r-process events as preserved in the spectra of old, very metal-poor stars in the Galactic halo suggest the possibility of two distinct r-processes producing the light r-process nuclei below $A < 130$ [9, 10]. Accurate nuclear data in the light r-process region will be important in disentangling the contribution of these different neutron-capture processes in different astrophysical sites, and the properties of nuclei around ^{78}Ni to ^{80}Zn will again play a critical role.

For the nuclei that participate directly in the r-process, β-decay half-lives are of particular importance (see [11]). For example, in the scenarios where the lighter neutron-rich nuclei participate in the r-process, the half-life of ^{78}Ni becomes a direct input into r-process calculation and, together with the other already known waiting points, ^{79}Cu and ^{80}Zn, sets the r-process timescale through the $N = 50$ bottleneck towards heavier elements, and also determines the formation and shape of the associated $A = 80$ abundance peak in the observed r-process element abundances. Figure 1.2 shows the current status of β-decay measurements in the r-process.

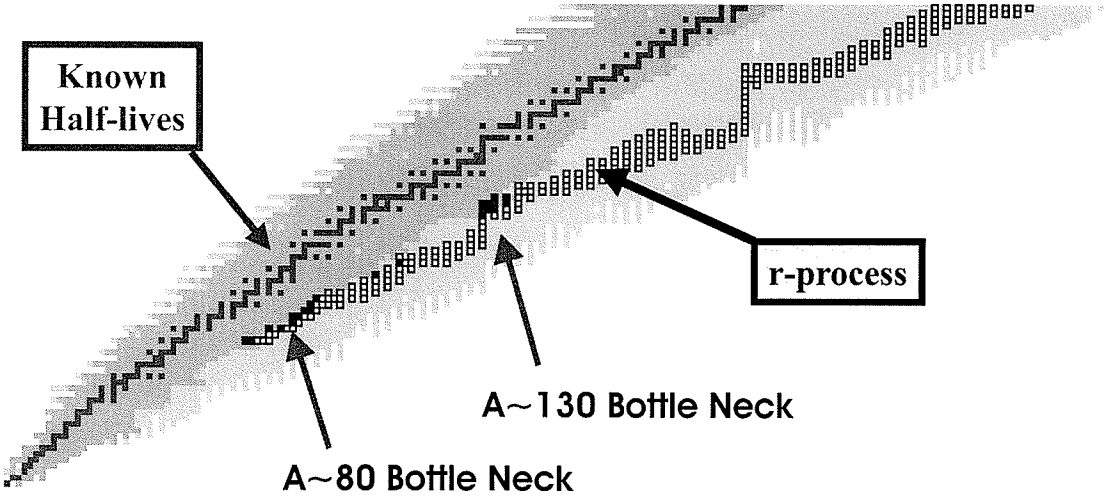

Figure 1.2: The current situation for β-decay measurements in the r-process.The white boxes represent the r-process path. The blue boxes represent nuclei for which half-lives have been measured. The dark blue boxes represent the nuclei in the r-process path for which the half-lives have been measured.

For the isotopes not directly in the r-process path but that are between the path and stability, the P_n values are important since they affect the processing after freeze-out and thereby affect the final abundance pattern.

1.3 Previous Work

The first measurements of nuclear properties in the r-process occured in 1986 at not one but two bottle-necks: ^{80}Zn and ^{130}Cd [12–14]. These are measurements of the half-

lives of waiting points at closed neutron shells. These nuclei are particularly important because they are the locations of the bottle necks and so there is strong interest in these regions. These nuclei are also the most easily accessible to experimenters because at the closed shells, the r-process comes closest to stability and so are most accessible to study.

1.3.1 N=82 shell region

The importance of the N=82 magic neutron shell chain to the r-process was already stated in B^2FH [15]. Here, the breakout was predicted at ^{131}I, making the half-life of ^{130}Cd an important bottleneck. The isotope ^{130}Cd was identified at CERN/ISOLDE in 1986 [12]. Consequently, the properties of other bottleneck nuclei in this chain, such as ^{129}Ag half-life [11] and ^{128}Pd were measured.

1.3.2 N=50 shell region

Another bottleneck region is the region of ^{80}Zn. The half-life, Q_β and a decay scheme of ^{80}Zn was first measured in 1986 at TRISTAN [13] and also at OSIRIS [14].

Progress toward the other N=50 bottlenecks, ^{79}Cu and ^{78}Ni continued. In 1985-86, the SOLAR Neutron Counter (SNC) was used to measure the first half-lifes and P_n values of $^{75\text{-}76}$Cu at the TRISTAN facililty through delayed-neutron counting techniques [16, 17]. $^{70\text{-}74}$Ni and $^{74\text{-}77}$Cu were first produced as extremely light products of thermal neutron (low energy) fission of ^{235}U at Grenoble, France and separated by the recoil spectrometer Lohengrin [18]. Though the yield was low, β-decay half-lives were later reported for $^{71\text{-}74}$Ni and remeasured for ^{75}Cu and also ^{74}Cu [19], which had since been produced and a half-life measured in 1989 by neutron induced fission of ^{235}U at TRISTAN where the half-life was also measured [20]. The following year ^{76}Cu was produced by the same method at TRISTAN. The half-life was remeasured, and isomers were found [21]. Meanwhile in 1988 at OSIRIS, $^{74\text{-}76}$Cu and ^{78}Cu were

observed and half-lives were measured [22].

Finally in 1991, the next N=50 r-process bottleneck, ^{79}Cu, was produced at CERN-ISOLDE using a proton beam on a ^{238}U-graphite target and a half-life (188 ± 25ms) and P_n (55 ± 17) were measured [23]. The half-life of ^{80}Zn (537 ± 29ms) was remeasured. This experiment also remeasured the half-lives of $^{74\text{-}76}$Cu, ^{78}Cu, ^{79}Zn, and provided the first half-lives of ^{77}Cu, ^{81}Zn (290 ± 50ms), and first P_n of $^{79\text{-}81}$Zn (1.3 ± 0.4, 1.0 ± 0.5 and 7.5 ± 3.0 respectively).

With ^{79}Cu and ^{80}Zn measured, this left ^{78}Ni as the only nucleus in the N=50 bottleneck region for which no measurements existed.

In 1992, $^{75\text{-}76}$Ni were produced by projectile fragmentation of a 500 MeV/u ^{86}Kr beam from the heavy-ion synchrotron SIS on a Be target and separated in the projectile-fragment separator FRS at GSI [24]. The half-lives of ^{75}Ni and ^{76}Ni were reported, but with large uncertainties.

In 1995, 12 ^{77}Ni and 3 ^{78}Ni were produced at GSI by fission of a ^{238}U projectile on a Be target [25–27]. The isotopes were seperated "in-flight" by the FRS fragment separator. For these, only the production cross-sections were measured.

Work on β-decay properties continued in this region. Half-lives were reported in 1998 for $^{70\text{-}72}$Co and $^{73\text{-}76}$Ni from measurements of ^{86}Kr fragmentation at GSI [28]. Also in 1998, proton-induced fission of ^{238}U at LISOL at Leuven produced half-lives and gamma spectroscopy of $^{68\text{-}74}$Ni [29]. But the question of the half-life of ^{78}Ni remained.

1.4 This Work

This work extends the nuclear physics data to ^{78}Ni and examines the influence of these new measurements on our understanding of nuclear structure and the r-process in this mass region.

In order to measure the P_n values, a new detector, the low-energy neutron detector NERO (Neutron Emission Ratio Observer) was developed. The developement and

design of NERO are described in Chapter 2. The calibration of NERO is described in 3. The experiment to measure the $t_{1/2}$ and P_n of nuclei in the vicinity of ^{78}Ni is described in Chapter 4. The analysis of this experiment is described in Chapter 5. We will show how this information can help to constrain theories that try to predict properties of even more exotic nuclei. This is done in Chapter 6. The results are applied to a model of the astrophysical r-process, and the effects of the new results on the process are shown. (also in Chapter 6.)

Chapter 2

Neutron Detector NERO

2.1 Introduction

For the purpose of measuring neutron emission probabilities, the neutron detector NERO (Neutron Emission Ratio Observer) was designed and built at the NSCL at Michigan State University and calibrated at the Nuclear Structure Laboratory at Notre Dame University.

2.2 Neutron Detection

Because they are electrically neutral, the detection of neutrons presents special problems that are not encountered in charged-particle detection. Unlike charged particles, neutrons are generally not detected by "direct" methods involving coulomb interactions. Rather, most neutron detection methods depend on a two-step process. In the first step, the neutron interacts with the detector via a nuclear interaction. This interaction initiates a secondary process that involves charged particles, which are then detected by the standard detection methods utilizing the coulomb force.

2.2.1 Fast and Slow Neutrons

In the context of detection, neutrons are generally classified into two groups based on their energy: fast and slow. Neutrons with energies above about 0.5 eV (which is known as the "cadmium cutoff") are considered "fast," and those below that energy are considered "slow." [30]. (Neutrons of energies around 0.025 eV are considered "thermalized".) Different methods are employed in the detection of neutrons from these two catagories.

For slow neutrons, neutron-induced nuclear reactions which create secondary radiation that is subsequently detected is the primary detection technique. At the slow neutron energies, elastic scattering on charged particles does not impart enough energy to the charged particles for this interaction to be useful in detection. The scattering does however serve to reduce, or moderate, the neutrons.

For fast neutrons with energies above around 0.5 MeV, collisions with charged particles, usually protons, result in high enough proton energies to use proton-recoil detectors such as plastic scintillators efficiently. Since the resulting spectra of these protons spans from the complete neutron energy all the way to zero, the efficiency of these detectors drops off at lower neutron energies usually due to the necessity to discrimate the low-energy protons from other low-energy signals such as gamma-ray signals or photomultiplier noise.

For fast neutron energies up to some point, moderating material (material that reduces a neutron's energy) can be employed to reduce fast neutrons to slow neutrons which can then be detected using the slow neutron methods. Since the process of moderation essentially loses information on the energy of the neutron, this moderator-slow-neutron-detector combination would be employed if only the number and not the energy of the neutrons impinging on the target is desired.

The neutrons emitted by the neutron-rich nuclei around ^{78}Ni are predicted to have energies ranging from about 0.1 to 1 MeV: too slow to be detected efficiently by plastic scintillators, but too fast for direct slow-neutron techniques. Therefore,

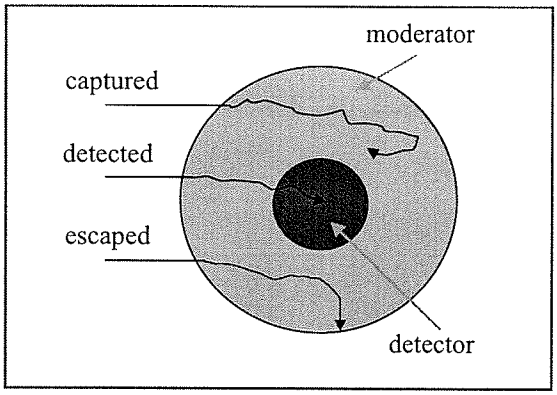

Figure 2.1: Finding the correct moderator size and configuration is a balance between moderation, detection, capture, and loss (Figure based on Figure 15.1 of Reference [30].

if high efficiency is required, a moderating system in conjunction with slow-neutron detection is the only choice.

2.2.2 Neutron Moderation

The best moderating material (the material that reduces the neutron energy in the most efficient manner) is that which contains hydrogen because of their comparable size. A neutron loses the most energy in a collision with a proton as they split momentum almost equally. Detectors with hydrogen-based moderators therefore allow for compact size, which also means smaller number of counters.

The disadvantage of hydrogen is that it also has a fairly large neutron capture cross section. The challenge for the design is to balance moderation needed to increase the detection efficiency with losses due to absorption in the moderator. The maximum efficiency possible is therefore limited to about 40%. From this point of view, heavy water or carbon would be better moderators, but would increase the detector size dramatically. We therefore chose hydrogen for our moderating material.

One cannot generally use a moderator composed completely of hydrogen, since this would be either a gas, and so not very dense, or would be liquid or solid, and so have to be maintained at extremely low temperatures. Therefore, one generally

uses materials made of compounds which contain a relatively high density of protons, and at the same time are physically manageable. Some examples are water, paraffin, and various other types of organic compounds such as plastics. Water is generally inconvenient to handle, especially around electronics. Paraffin melts easily and is flammable. Plastics on the other hand are easily fashioned and managed.

2.2.3 Proportional Counters

Proportional counters have been used successfully as high-efficiency slow-neutron detectors. Proportional counters are tubes filled with a gas, with a cathode (anode) wire running down the middle. The gas is selected for two properties, corresponding to the two steps involved in neutron detection mentioned above. First, the gas is selected to have a high cross section for an (n, p) or (n, α) reaction. Second, the gas must serve to support the cascade of electrons that cause a signal in the cathode (anode). Generally the gas has a high cross section for slow neutrons, and the efficiency quickly drops off as a function of neutron energy for the detection of faster neutrons. For fast neutron detection, therefore, proportional counters are used in conjunction with moderating material.

Two common proportional counters are the ^{3}He and Boron Triflouride (BF_3) detectors. BF_3 detectors make use of the ^{10}B(n,α)^{7}Li reaction. In this reaction, the Li can be left in the first excited state, which happens about 94% of the time for thermal neutrons (Q-value = 2.792 MeV to ground state, 2.310 MeV to first excited state) [30]. The ^{3}He detectors take advantage of the ^{3}He(n,p)^{3}H reaction (Q-value = 0.764 MeV). In both cases, since the neutron energy is small compared to the Q-value of the reaction, the charged reaction products essentially split the Q-value of the reaction, and any knowledge of the neutron energy is lost. The charged reaction products are detected through the cascading gas and record an energy equal to the Q-value of the respective reaction. By momentum conservation, the charged products split the energy inversely by mass. If one of the charged particles strikes the wall of the

counter, the energy recorded by the detector is smaller by the amount of energy that particle carried. This result is known as the wall effect and results in the spreading of the energy spectrum detected below the Q-value of the reaction.

2.3 NERO Development

2.3.1 General Design Considerations

There were several experimental criteria considered in determining the optimal configurtaion for NERO. A high efficiency is required since the rates for β-delayed neutrons that will be studied with NERO are generally low. The energies of the neutron-rich nuclei of interest are generally not known, so the efficiency must remain high for a range of neutron energies. The efficiency curve must also be as flat as possible in order to minimize the uncertainty in the final result due to uncertainty in neutron energy. Lastly, the detector must work in conjunction with existing β-detectors and beamline requirements.

The NERO design was based on existing detectors, most directly the Mainz neutron detector (References [31] or [32] for example). NERO and the Mainz detector are of a class of detectors that utilize moderating material in conjunction with a slow-neutron detector as mentioned previously. Many variations of slow-neutron detector types, shapes, sizes, as well as moderating matrix type, shape, size and configurations have been used in the past. Some well-known styles of detectors of this kind are the spherical dosimeters and the long counters.

Long counters are proportional tubes embedded in a moderating matrix and generally possess an axial symmetry. The long counters were designed to give a flat efficiency response as a function of neutron energy. However, one drawback of this design is that the detector is designed to accept neutrons only at one face. For the situation for which NERO is to be used– neutron emitters implanted in a target and emitting isotropically– this design would start with a detection efficiency of less

than 50% simply due to geometrical considerations. A design where the target is surrounded by detecting material is more advantageous from a geometrical efficiency point of view.

A sort of quasi-long counter which features almost 4π coverage is sometimes refered to in the literature simply as 4π detectors, or sometimes 4π long counters. These detectors feature a relatively flat efficiency dependence on the neutron energy, as with a long counter. They are also generally axially symmetric as the long counters. However, instead of accepting neutrons impinging on one face, they contain a hole to allow insertion of a neutron source or implant beam into the center, thus affording almost 4π coverage. The flat efficiency is then acheived by a creative arrangement of rings of detectors. The NERO and Mainz detectors are examples of such detectors. Some other examples are found in References [23, 33–36].

Multiple rings also allow for the possibility of extracting some energy information, which may be desirable since otherwise most of the energy information of the neutron is lost in moderation. (see References [37, 38] for example)

The 4π design was adopted for NERO. The configuration allows for a beamline to pass into the core of the detector where beams of neutron-rich nuclei can be implanted into a β detector system, and the neutron source will therefore have close to 4π coverage. This design also can afford, with the proper arrangement of moderator and proportional tubes, a flat efficiency response.

Because of the size of fast-fragment beams and the need for insertion of an entire segmented implantation detector, the beamline hole for NERO was required to be larger than is usually encountered with these types of detectors. The minimum clearance for the intended implant target and β-detection system– specifically the NSCL Beta Counting System– was about 11 cm. To have such a large beamline hole and still maintain a high efficiency was a special challenge and one of the primary reasons why a redesigned detector was required. The larger the beamline hole, the farther away the tubes are and therefore the less solid-angle coverage the same number of

tubes can provide. For comparison, the beamline hole for the Mainz 4π detector is 5.5 cm. Beamline holes for other similar detectors are for example 4.48 cm [37] and 5.1 cm [34]. The detector in Reference [35] had an 11.5 cm $\times$ 11.0 cm beam hole, but reports a maxiumum efficiency of less than 25%.

2.3.2 MCNP Modeling

The code MCNP (Monte Carlo N-Particle) (http://laws.lanl.gov/x5/MCNP/index.html) was used to model NERO during the design phase. MCNP has been used in the past for modelling of 4π neutron detectors (see Reference [35] and references therein, and Reference [34] for example). MCNP tracks a neutron's path and interactions through material. The proportional counters used for NERO are both Boron Trifloride gas (BF_3) and ^{3}He gas. The moderating matrix choice was polyethelyne. A general configuration composed of the above counters arranged in concentric circles in the polyethelyne matrix was the starting point of the design. This configuration, with an isotropic neutron source, was input into MCNP. Then several parameters were varied in MCNP: the position and number of proportional tubes, the size and shape of the matrix, and the central hole size. All of these parameters were tested over a range of neutron energies from 1 keV to 5 MeV. The parameters were adjusted to produce the highest efficiency curve with the flatest energy dependence possible. The constraints were the type of tubes available, and the large minimum beamline hole diameter required to fit the NSCL Beta Counting System. The effects of variations in external shielding were also taken into account.

The design is a balance between moderation and absorption. For example, inside the first ring there needs to be just enough moderator to moderate the lowest energy neutrons for detection, but not so much that a large fraction are absorbed inside the moderating material (see Figure 2.2). The same is true for higher-energy neutrons, which must encounter enough moderating material before and after the inner ring to be detected in the second ring, but must not encounter too much moderator that they

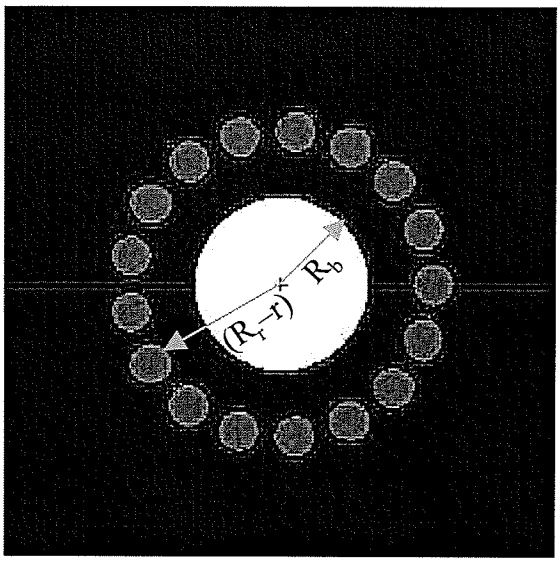

Figure 2.2: An optimization of NERO parameters. R_b is the beamline hole radius. R, the amount of polyethylene moderator along the inside radius of the ring. $R = (R_r - r) - R_b$ where r is the radius of an individual counter, and R_r is the radius to the detector ring, defined as the distance to the center of any counter in the ring.

are captured in the moderator before arriving at the second ring. The same is true for the third ring. Eventually the efficiency curve must drop off however for higher neutron energies as more and more moderation is required and so the probability for neutron capture in the moderator via (n,γ) increases. In addition, spacing between counters in the same ring must be optimized. If the detectors are too close together, not enough moderator will be present to get the optimum efficiency. If the detectors are too far apart, the probability for a moderated neutron to find a counter decreases. A certain amount of moderating material is also required beyond the last ring since neutrons can pass the last ring and then diffuse back to the detectors. Without the moderator beyond the outer ring, all of the neutrons that passed the ring would escape. The amount of moderating material at the ends of the detectors are important for similar reasons, and the amount of that material was also optimized.

The MCNP efficiency curve for the final NERO design is shown in Figure 2.5. As can be seen from the plot, the calculated efficiency is relatively constant at about 45% from 1 keV to 500 keV, dropping off to around 26% by 5 MeV.

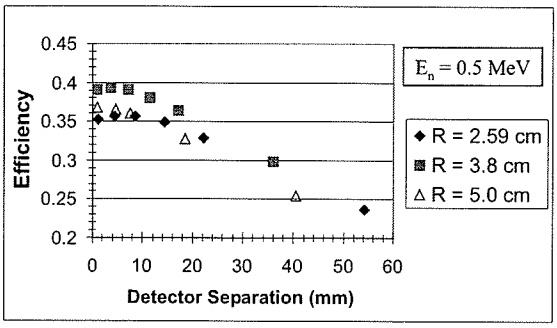

Figure 2.3: A study of the optimal detector separation.

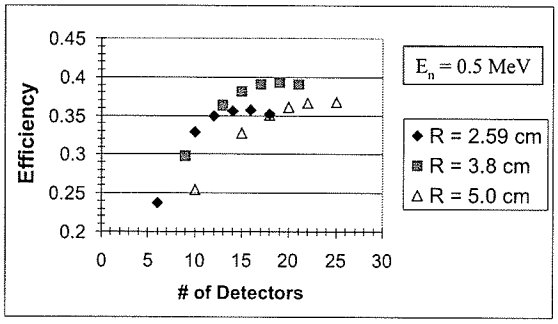

Figure 2.4: A study of the optimal detector number.

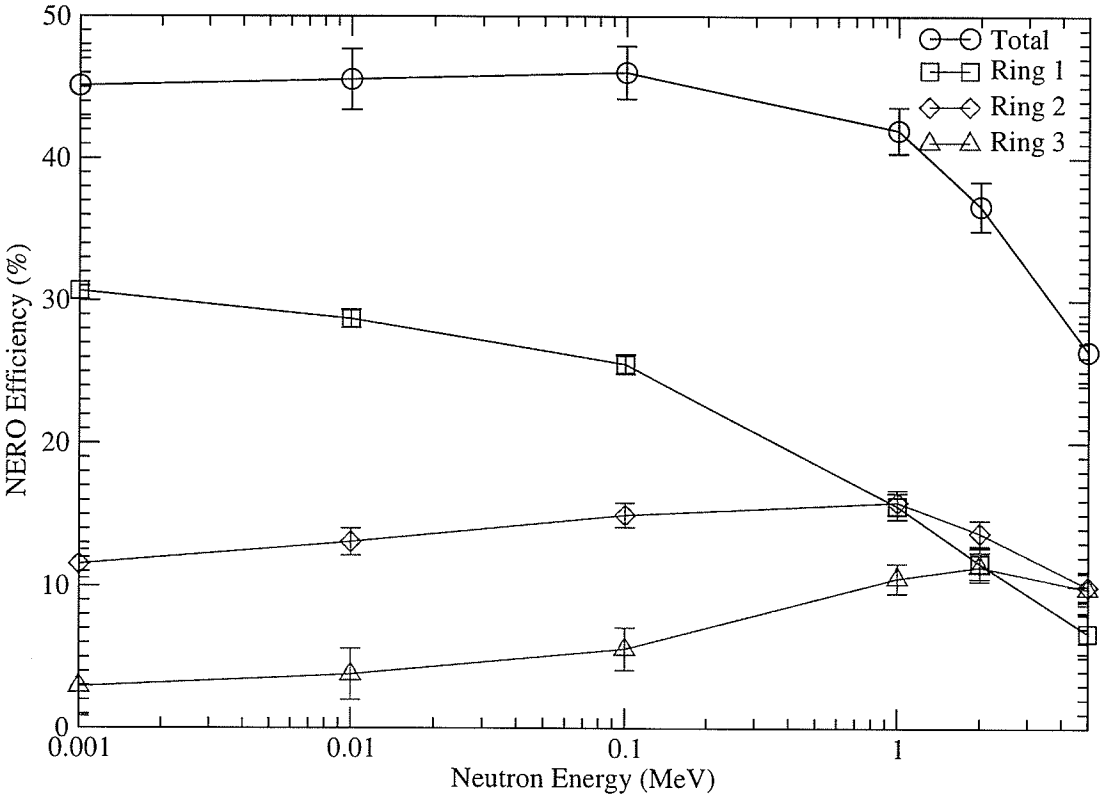

Figure 2.5: NERO efficiency vs. neutron energy as calculated in the code MCNP. The plot includes the total NERO efficiency, as well as the efficiencies of each of the three rings of proportional tubes. Ring 1 is the inner ring and is composed of 16 ^{3}He detectors. Ring 2 is the middle ring and is composed of 20 BF_3 detectors. Ring 3 is the outer ring and is composed of 24 BF_3 detectors.

Table 2.1: Reuter-Stokes ^{3}He Counter Part Numbers Used in NERO (Part X-#).

5434	5458	5463	5468
5448	5459	5466	5473
5454	5462	5467	5476

Table 2.2: Mainz ^{3}He Counter Part Numbers Used in NERO.

849
850
851
852
853

2.3.3 NERO Design

Based on the MCNP optimization, the details of the final design of NERO are as follows. The polyethylene moderating matrix is 60 cm by 60 cm by 80 cm, being longer along the beam axis. The detector contains 60 proportional counters: 16 ^{3}He and 44 BF_3 tubes, arranged in three concentric rings. The inner ring has a radius of 13.6 cm and contains 16 ^{3}He tubes. The second ring has a radius of 19.2 cm and contains 20 BF_3 tubes. The outer ring has a radius of 24.8 cm, containing 24 BF_3 tubes. The rings are all concentric around the cylindrical beamline hole of radius 11.2 cm running the length of the detector along the beamline direction.

Two models of ^{3}He counters were used in NERO. Twelve of the ^{3}He counters are Reuter-Stokes model RS-P4-0814-207, on loan to the NSCL from Pacific Northwest National Laboratory. These tubes have two external connectors at the end of a Cu cap which are connected inside the cap to the anode wire, for the purpose of "daisy-chaining" the detectors, although this feature was not exploited in NERO. The connectors are SMC standard. Table 2.1 lists the part numbers of these counters. The remaining four ^{3}He detectors are models obtained from the University of Mainz, Germany. Table 2.2 lists the part numbers of these counters. All of the BF_3 tubes are Reuter-Stokes model RS-P1-1620-205, on loan to the NSCL from Pacific Northwest National Laboratory. They are 100% BF_3 gas enriched in ^{10}B to greater than 96%.

Table 2.3: Reuter-Stokes BF_3 Counter Part Numbers Used in NERO (Part V-#).

3988	4021	4056	4079	4102
3989	4029	4062	4080	4107
3992	4030	4063	4081	4111
3994	4032	4069	4082	4112
3995	4034	4070	4084	4113
3996	4043	4072	4086	4116
4004	4046	4073	4091	4117
4007	4048	4074	4092	4118
4010	4050	4076	4096	4119
4013	4052	4078	4097	4120

Table 2.4: Proportional Tube Data.

Detector	Active Length (in)	Inactive Length (in)	Radius (in)	Nominal Pressure (atm)
Mainz ^{3}He	9.84	10.24	0.5	5.732
PNNL ^{3}He	14	17	0.5	4
PNNL BF3	20	22	1	1.18

The casing is 304 Stainless Steel. Table 2.3 lists the part numbers of the tubes. The dimensions and nominal pressures for the various types of proportional counters used in NERO can be found in Table 2.4.

The moderating polyethelyne block was divided into two halves, upper and lower. In addition, each half was cut into 6 equal pieces so that the the entire moderating block can be dissassembled into 12 pieces for transportation. When assembled, the pieces are held together by 8 stainless steel bolts which run the length of NERO and which were included in the simulations. During assembly, first the blocks are arranged, the bolts are inserted, and then the counters are inserted into the counter holes, which are drilled from the downstream end of NERO, so that they are centered about the target position.

A boron carbide shield was added around the outer faces of NERO. The boron carbide shield was fabricated by mixing boron carbide powder in epoxy and pouring the mix into a frame. Inside the sheet is layed fiberglass ribbons to provide added support.

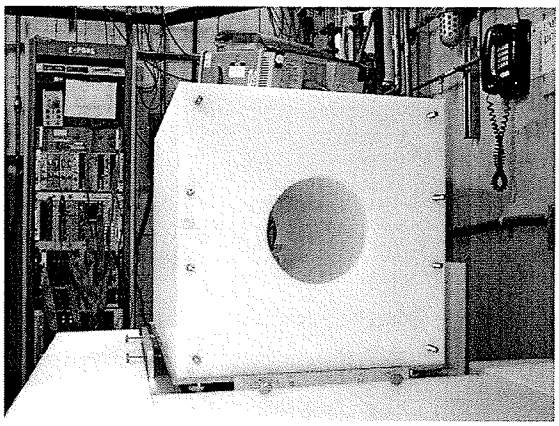

Figure 2.6: NERO polyethelene moderating matrix (view looking along beamline direction.

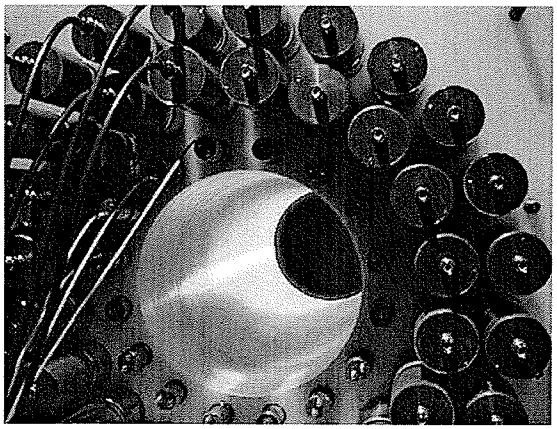

Figure 2.7: Close view of NERO with tubes inserted. The hole is the beamline hole for insertion of beamline and Beta Counting System.

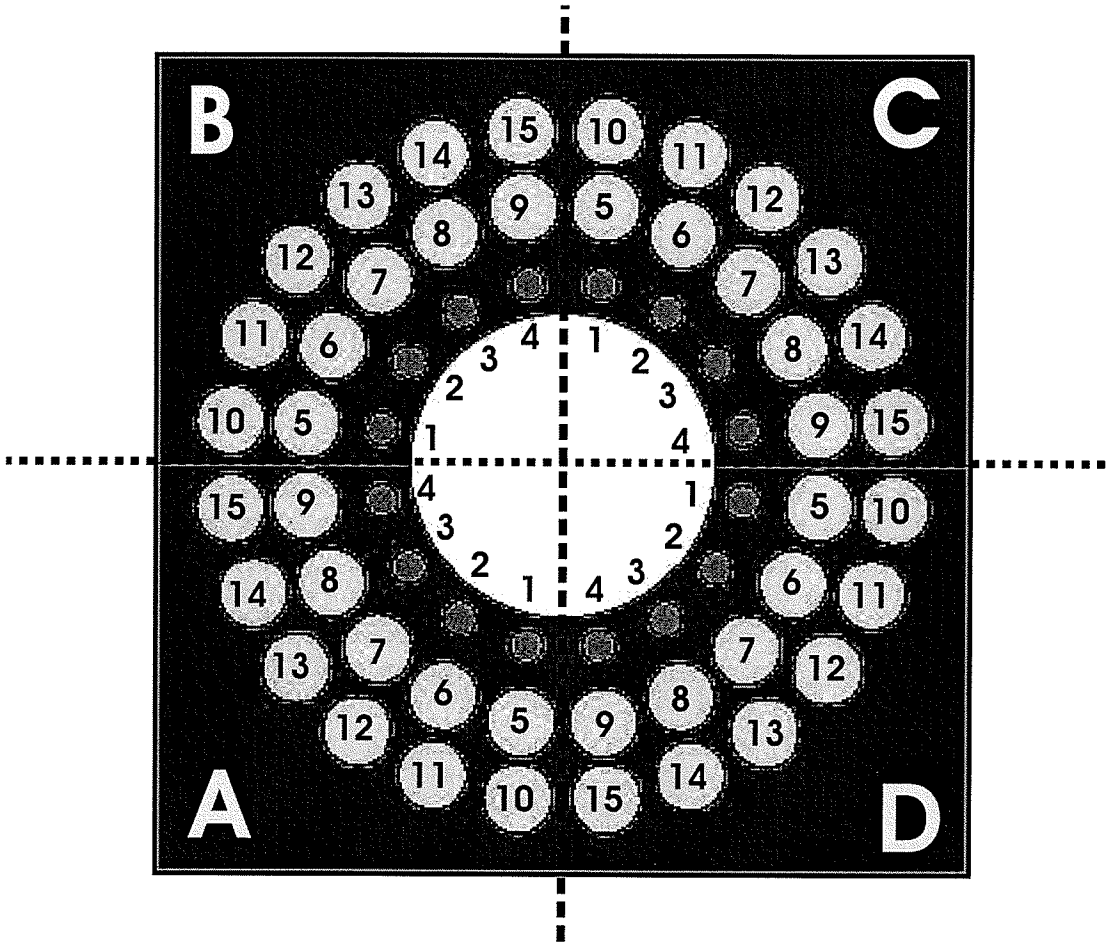

Figure 2.8: Diagram of NERO quadrant and detector labeling. The beam is coming out of the page.

2.3.4 NERO Electronics

For the purpose of electronics, NERO was divided into four quadrants, and the detectors were numbered according to quadrant (See Figure 2.8). A diagram of the NERO electronics can be found in Figure 2.9.

High Voltage and Preamplification

All counters from a given quadrant are connected via high-voltage cables (Figure 2.10) to one dedicated preamplifier box designed specifically for the NERO detector (Figure 2.11), which contains 16 individual preamp chips, leaving one spare channel

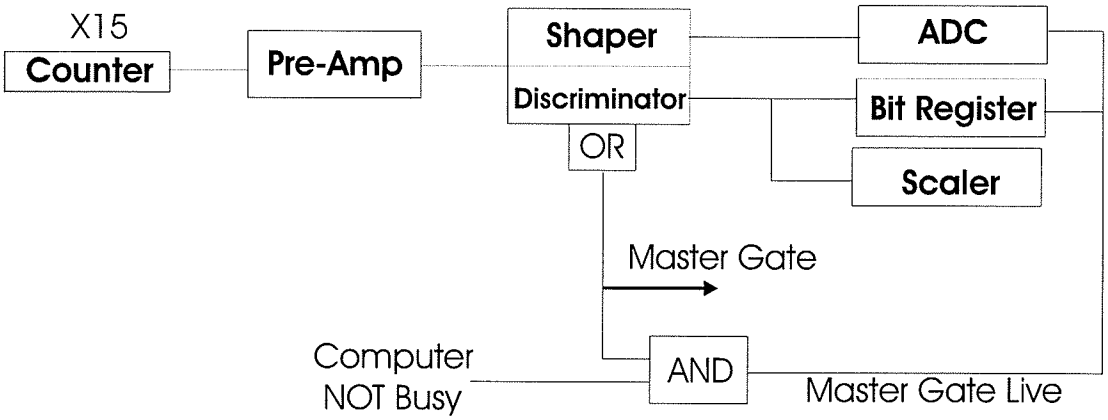

Figure 2.9: Diagram of NERO electronics for one quadrant.

Table 2.5: Proportional Counter High Voltage Requirements.

Detector	High Voltage (V)
Mainz ^{3}He	$\sim$+1300
PNNL ^{3}He	+1050 – +1100
PNNL BF3	$\sim$+2600

per preamp box. The high-voltage requirements for the counters is given in Table 2.5. The preamp chips are powered by $\pm$9 Volts which comes into the box through one connector and is split inside the box to each of the chips. The preamp box has two high-voltage inputs. The first high-voltage input is sent inside the box to the first four channels, and the second high-voltage input is sent inside the box to the remaining 12 channels, so that the different tubes can be held at different voltages. The preamplifer chips inside the preamp box are Cremat CR-101D miniature charge sensitive preamplifiers designed specifically for nuclear detection instrumentation. These are mounted on a board designed and fabricated at the NSCL.

Shaping and Discriminating

The signals for a given quadrant are sent out of the preamp box via a 34-wire ribbon cable to a dedicated double-wide CAMAC 16-channel shaper/discriminator module designed by Pico Systems (see Figures 2.12). Inside the double module, the signal goes through the discriminator, and then is split. One signal proceeds on through

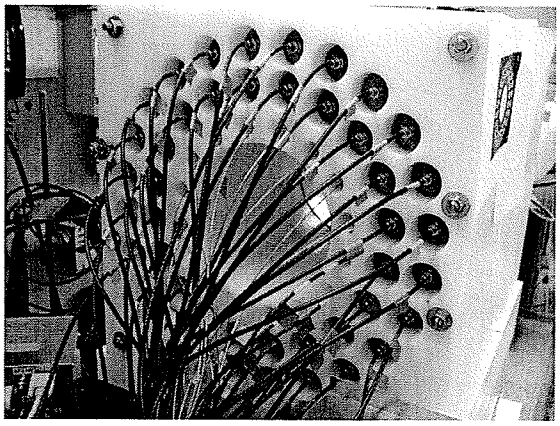

Figure 2.10: High voltage cables coming out of the proportional tubes to the preamp boxes.

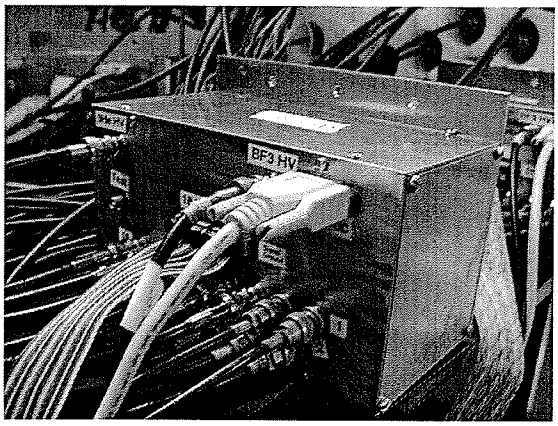

Figure 2.11: Preamp box for one NERO quadrant.

Figure 2.12: Pico Systems Shaper/Discriminator (Photograph from http://pico-systems.com).

the shaper, while the other goes out of the discriminator to be used for fast timing purposes. The discriminator thresholds and shaper gains for individual channels can be changed remotely through software.

Timing, Triggering, Digitalization

The discriminator outputs go to a bit register and a scaler. The shaper signal goes to an ADC for readout of energies. The discriminator also features an OR signal output of all 16 channels. This signal serves as the master gate/trigger. It is ANDed with triggering logic for computer NOT busy, and the result is the master gate/trigger LIVE. This signal serves as the gate for the ADC and bit register.

2.3.5 NERO Support Table

Because of the weight of NERO when fully assembled, a special support table was designed to allow relatively easy position adjustment and alignment. The table includes four screw feet for height adjustment. The table also features a plate which rides freely on top of large ball bearings. Indvidual screws are adjusted against the plate resulting in orientation adjustments in the x-y plane.

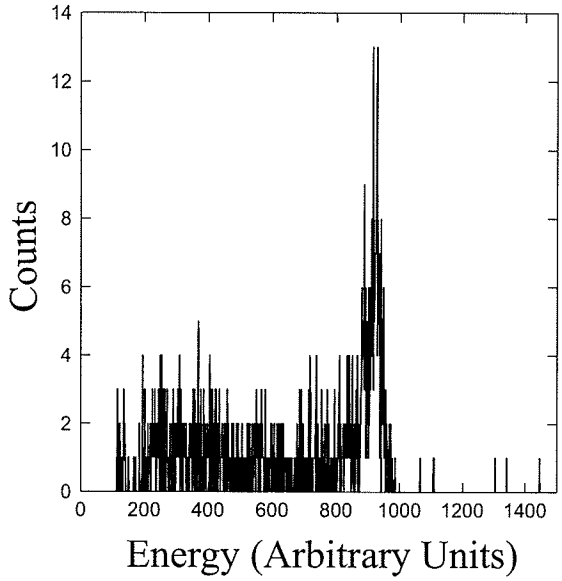

Figure 2.13: NERO background spectrum in a typical ^{3}He counter. The characteristic shape for neutron detection is clearly identifiable.

2.3.6 NERO Background

Background simulations were conducted with various shielding configurations and background measurements were taken with and without shielding. Figure 5.11.2 shows a common NERO neutron background spectrum. The signature neutron spectrum can clearly be seen indicating that the background is in fact real neutrons. Real neutron background can originate from cosmic rays. During the Calibration at the Notre Dame Nuclear Structure Laboratory, the detector was shielded by water jugs, and the background rate was around 15-20 counts per second for the entire detector. Before experiment 02028 at the NSCL experimental vault, the unshielded background rate was 5 per second for the entire detector. Consequently, water jugs were not used for shielding during experiment 02028.

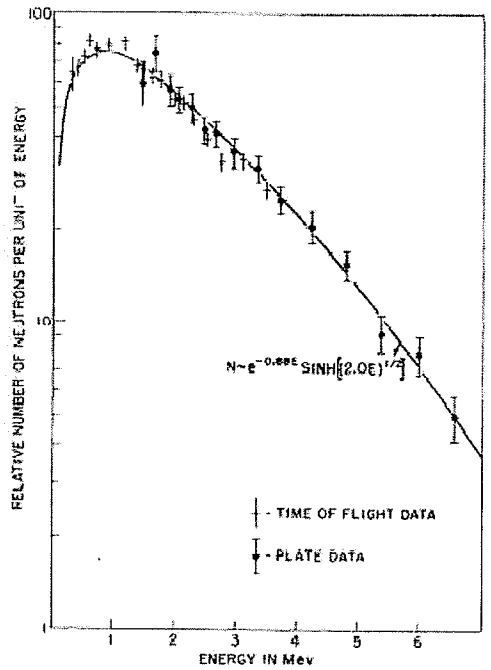

FIG. 2. Experimentally determined energy spectrum of Cf^{252} fission neutrons.

Figure 2.14: Neutron energy spectrum from the spontaneous fission of ^{252}Cf (Figure 2 of Reference [39])

2.3.7 Tests with ^{252}Cf

Efficiency

^{252}Cf, a spontaneous-fissioning neutron emitter with a half-life of 2.638 years, is a readily available neutron source that has been used often for calibration of neutron detectors (see for example References [31, 35, 37]). When it fissions, ^{252}Cf emits neutrons with a broad range of energies at 0.116 neutrons/s/Bq (Reference [30], p. 20). The ^{252}Cf neutron energy spectrum is shown in Figure 2.14. The average neutron energy is 2.35 MeV.

We obtained a ^{252}Cf source at the NSCL. The specific source information is found in Table 2.6. An uncertainty in the activity at the time of calibration was not given. One could assume the figure quoted is to the least significant figure, which would result in an uncertainty 1 μCi or 2%. However, a conservative 5 % uncertainty was

Table 2.6: ^{252}Cf source information

Company	Isotope Products Lab, Burbank, CA
Catalogue #	FF-252-4
NSCL Source #	N-355
Capsule Type	FF Holder
Cover	50 μg Au
Active Diameter	5 mm
Activity	50 μCi
Calibrated On	Nov. 19, 1990

assumed. The current activity was calculated from the known initial activity. This activity was multiplied by the neutrons/s/Bq from Ref. [30] to obtain a calculated neutron rate. This was compared to the neutron rate measured by NERO with the source located at the target position. The efficiency was calculated to be 26.4 ± 1.5 %.

Peak Efficiency Position

The ^{252}Cf source was also used to locate the axial position within the beamline hole which has the maximum neutron efficiency. During experiments, this should be considered the target position. By design, the target position should be at the midpoint of the beamline hole. This assumption was validated by the ^{252}Cf study (see Figure 2.17). It can also be seen in the figure that the efficiency function along the axial direction is fairly symmetric for small displacements around the target position.

NERO Neutron Moderation Time Measurements

The NERO neutron moderation time was also studied with the ^{252}Cf source. In the fission of ^{252}Cf, γ-rays are emitted in coincidence with neutrons. A ^{252}Cf source was placed on the bottom surface of the NERO beamline hole 3 in. from the end. A BaF_2 gamma detector was inserted in the NERO beamline hole from the up-beamline direction.next to the source. The detection of a gamma by the BaF_2 was sent to a TAC with a delay as a start, and the detection of a neutron by NERO served as a

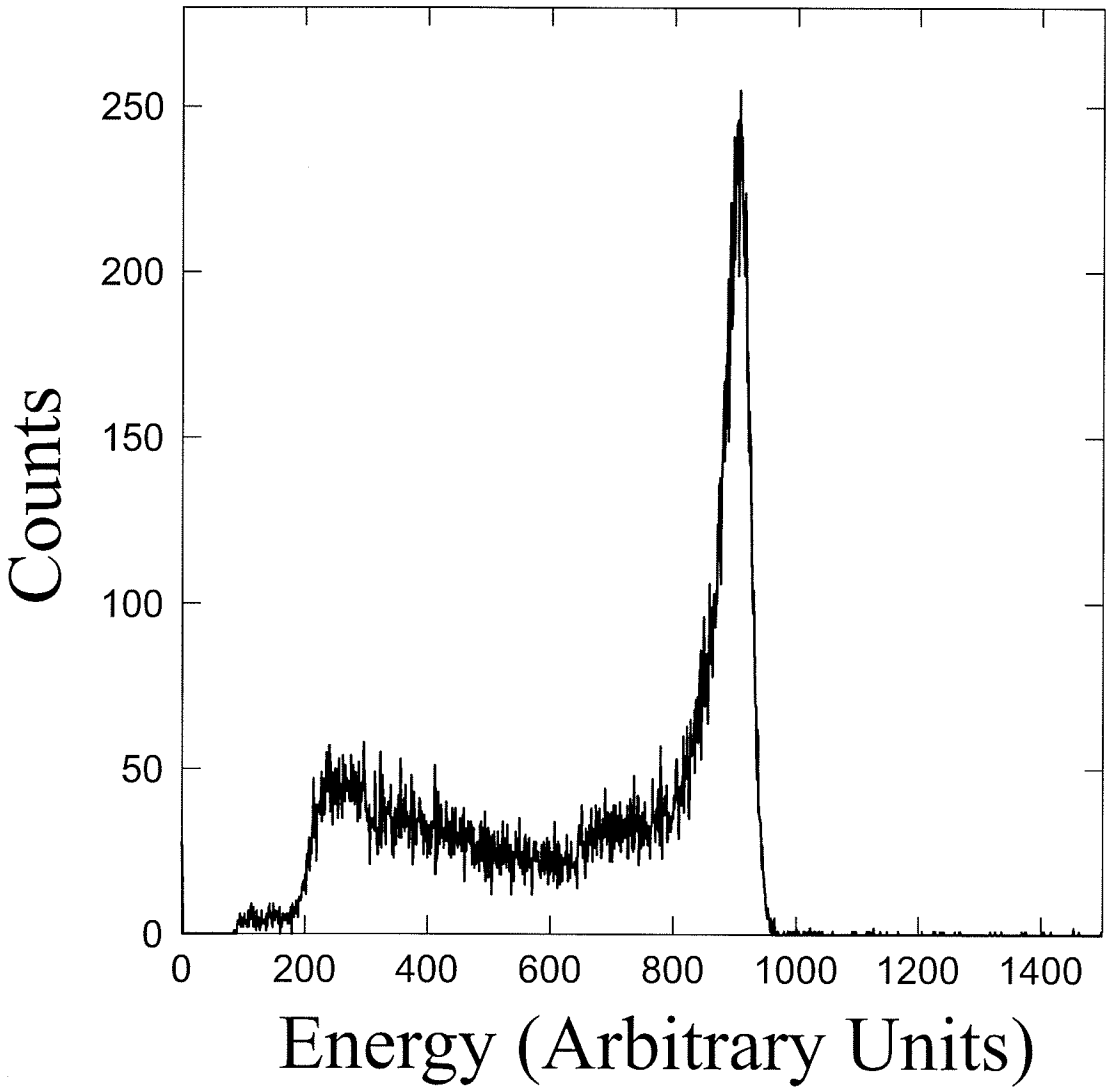

Figure 2.15: Typical NERO ^{3}He neutron spectrum from ^{252}Cf source.

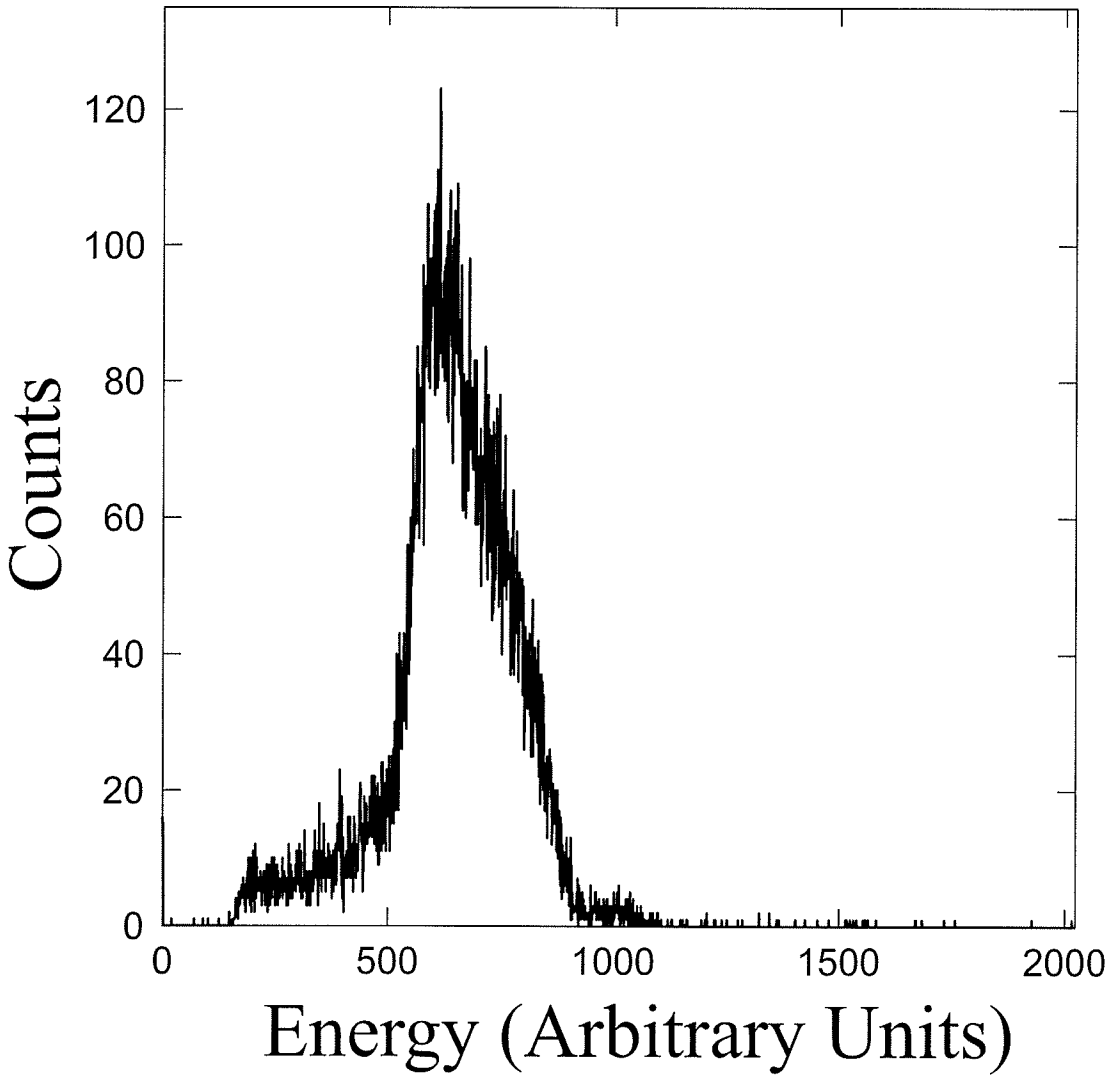

Figure 2.16: Typical NERO BF_3 neutron spectrum from ^{252}Cf source.

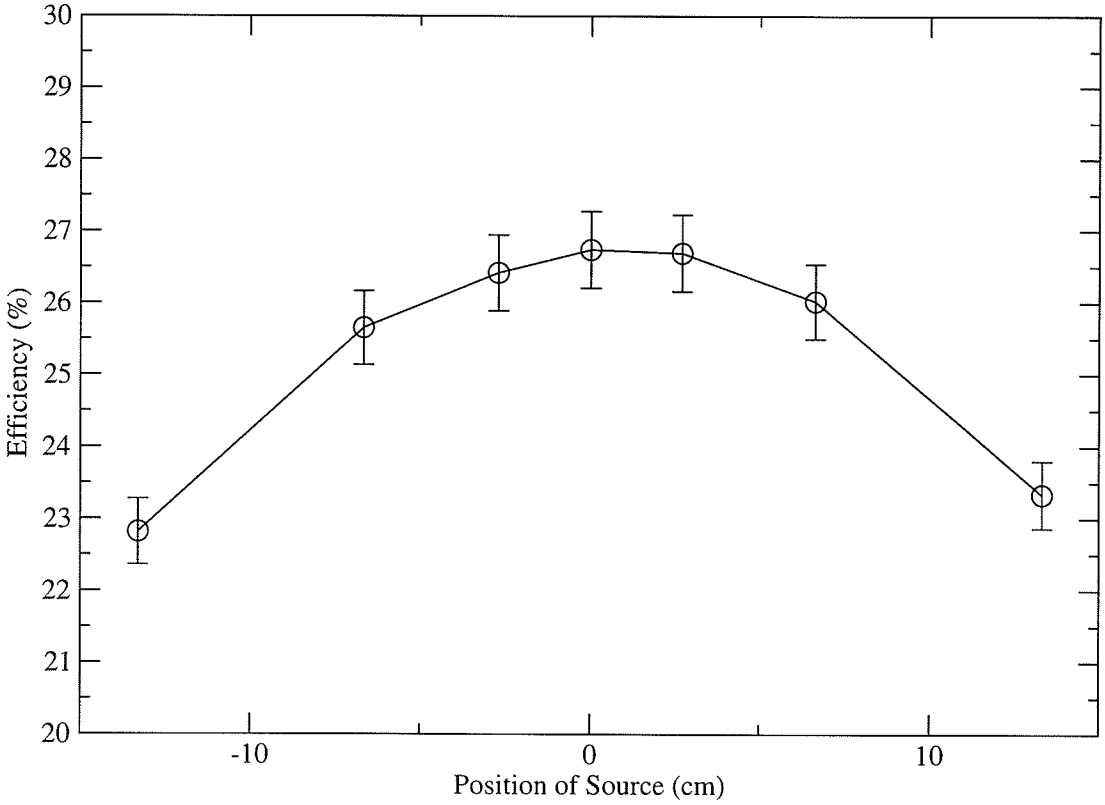

Figure 2.17: Variation of NERO efficiency in the beamline hole as a function of position along the beamline axis. Zero is the NERO target position. Larger negative numbers are up the beamline direction.

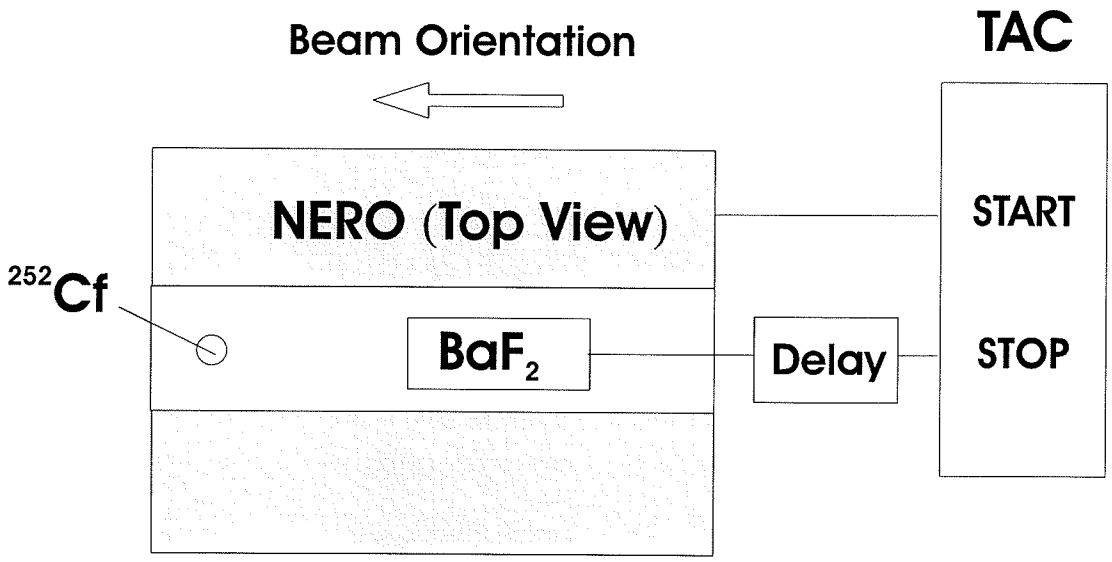

Figure 2.18: Schematic for NERO neutron moderation time measurement.

Table 2.7: Moderation Time for Neutrons in NERO.

Time (μs)	Percent of Neutrons Moderated
50	52
100	80
150	93

stop (see Figure 2.18). The results of this test can be found in Table 2.7 and the moderation time spectrum can be found in Figure 2.19. Almost all of the detected neutrons are moderated within about 200 μs.

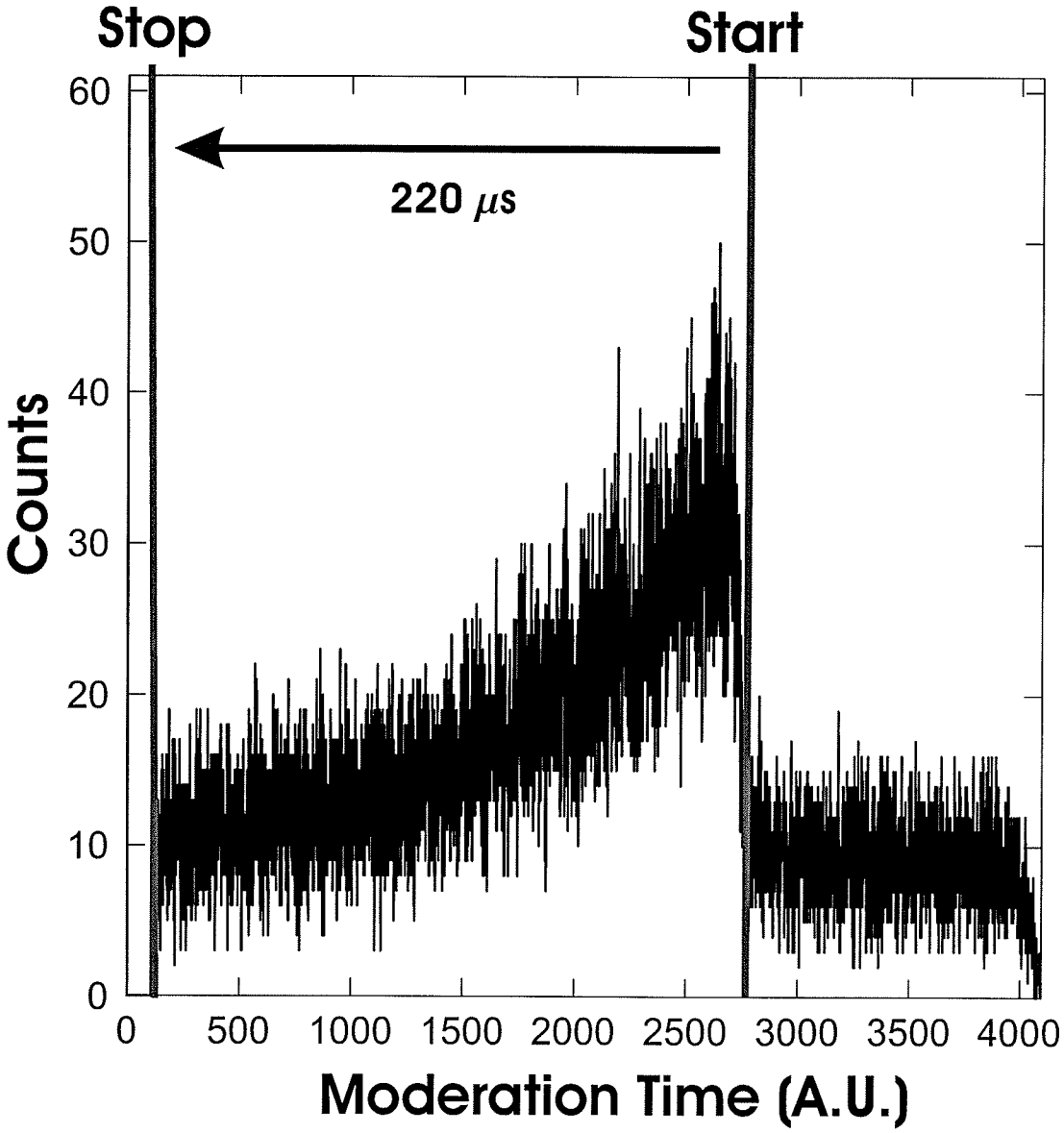

Figure 2.19: BaF_2 Moderation timing measurement with ^{252}Cf source. The start and stop for the TAC were inverted.

Chapter 3

NERO Efficiency Calibration

3.1 Introduction

To test the theoretical efficiency curve produced by the MCNP code, a calibration of the NERO detector was carried out at the University of Notre Dame Nuclear Structure Laboratory.

Using the KN Van de Graaff accelerator to accelerate α and proton beams into targets in the NERO target position, $^{13}C(\alpha, n)$, $^{11}B(\alpha, n)$, $^{51}V(p, n)$ reactions were used to produce neutrons at several well-defined energies. The detected neutron rates were compared to calculated rates based on known quantities, and the efficiency was thus calculated at several energies. For ^{13}C and ^{11}B, resonant reactions were used. For ^{51}V, non-resonant reactions were used.

The NERO efficiency in percent was calculated as follows.

$$\epsilon = 100 \times \frac{N'_d}{N_p} \tag{3.1}$$

where N'_d is the number of neutrons detected by NERO, corrected for background, and N_p is the number of neutrons produced. N_p is calculated based on known information about the reaction.

1. SNICS Ion Source
2. HIS Ion Source
3. FN Van de Graaff Accelerator
4. Gamma Spectroscopy Beamline
5. Spectrograph Beam Line
6. R2D2 Beam Line (1 m scattering chamber)
7. Weak Interaction Beam Line
8. RNB Beam Line
9. Neuton Detection Wall
10. Conference Room
11. Accelerator Control Consoles
12. ECR Ion Source Test Setup
13. KN Van de Graaff Accelerator
14. JN Van de Graaff Accelerator
15. ORTEC Scattering Chamber
16. Windowless Gas Target Beam Line
17. Gamma Table

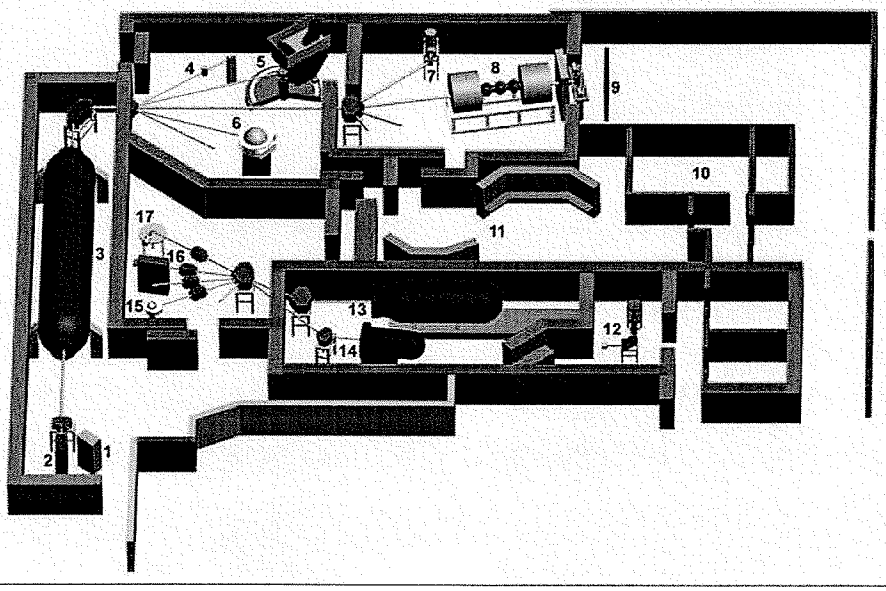

Figure 3.1: Layout of the Notre Dame Nuclear Structure Laboratory. The protons or α-particles were accelerated in the KN Van de Graaff accelerator (13), then were directed into the experimental vault to the location of the Gamma Table (17) which was replaced by a special stand for NERO (Image from http://www.nd.edu/~nsl/).

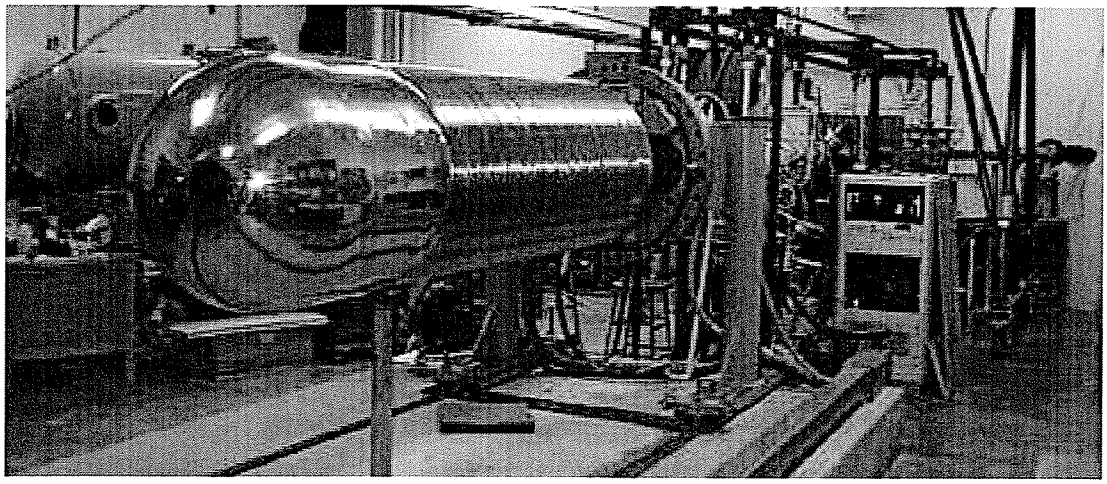

Figure 3.2: The KN Van de Graaff accelerator at the Notre Dame Nuclear Structure Laboratory. (Image from http://www.nd.edu/~nsl/)

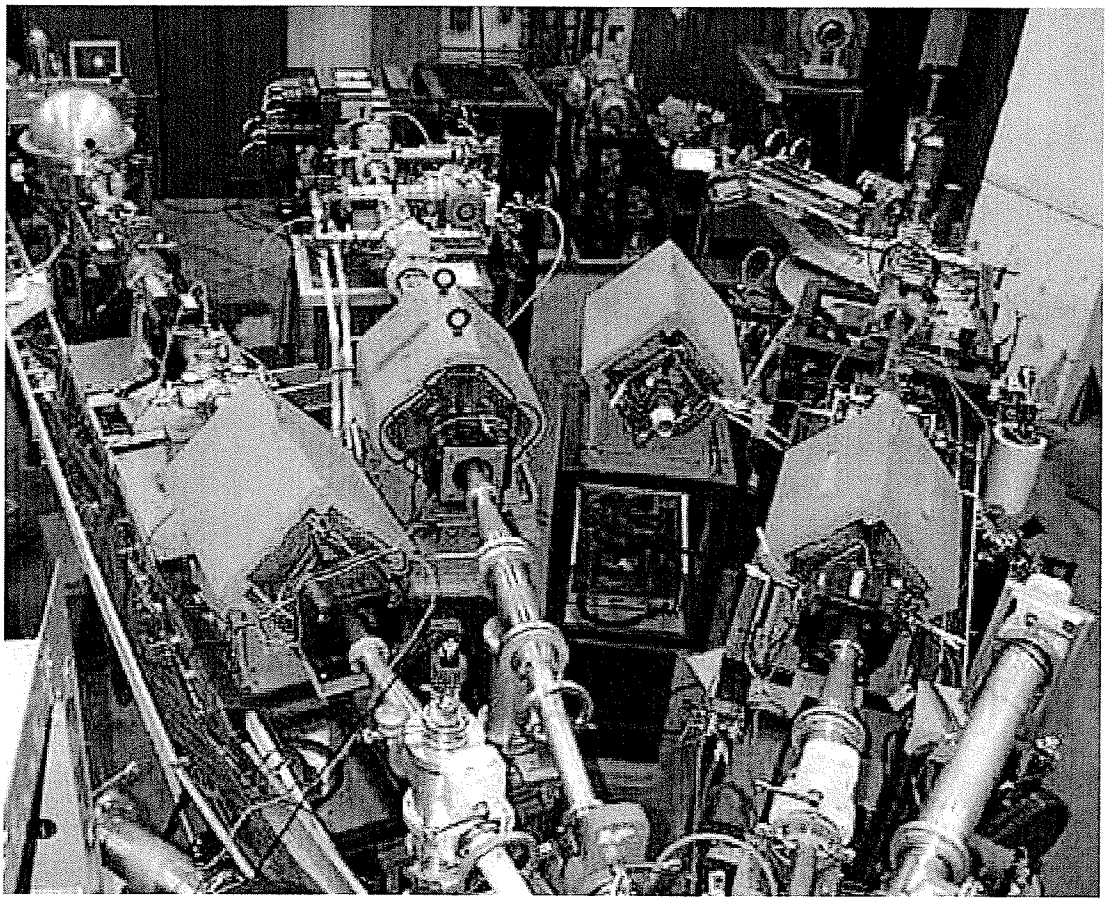

Figure 3.3: View of the experimental vault beamline. NERO was located in the place of the Gamma Table (top right), which was removed for the experiment (Image from http://www.nd.edu/~nsl/).

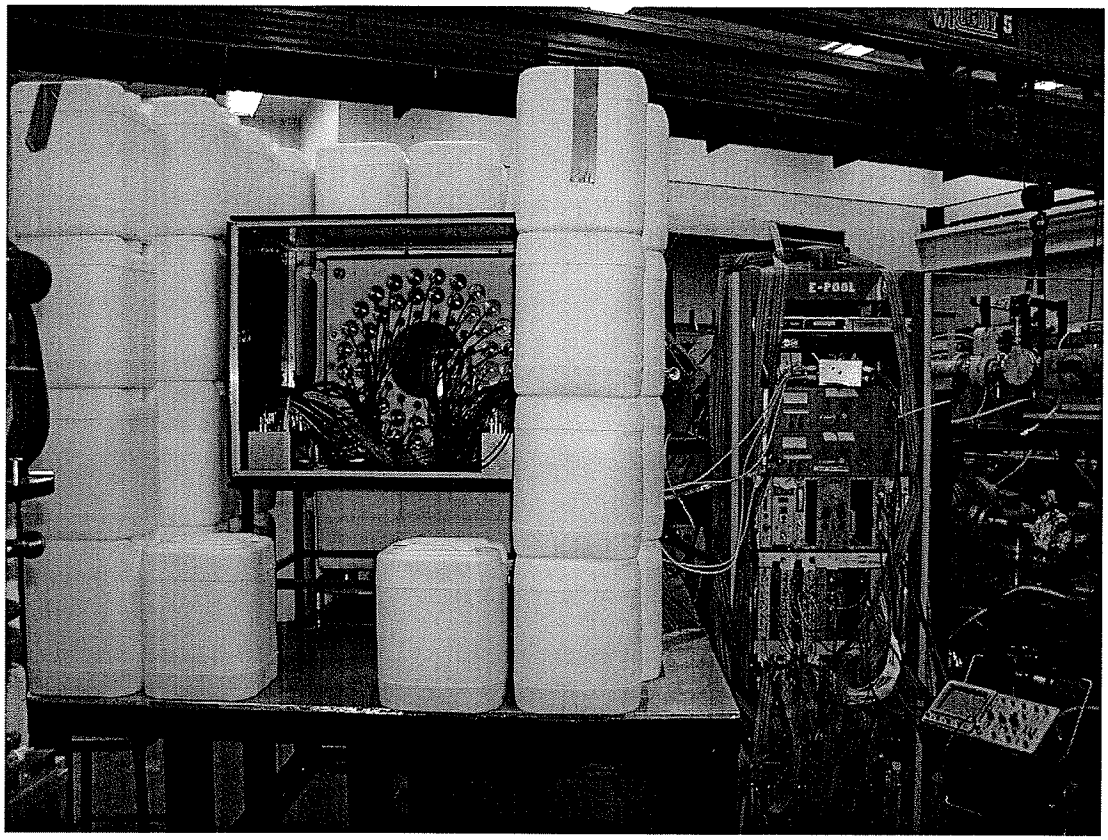

Figure 3.4: NERO set up at Notre Dame. View is up the beamline.

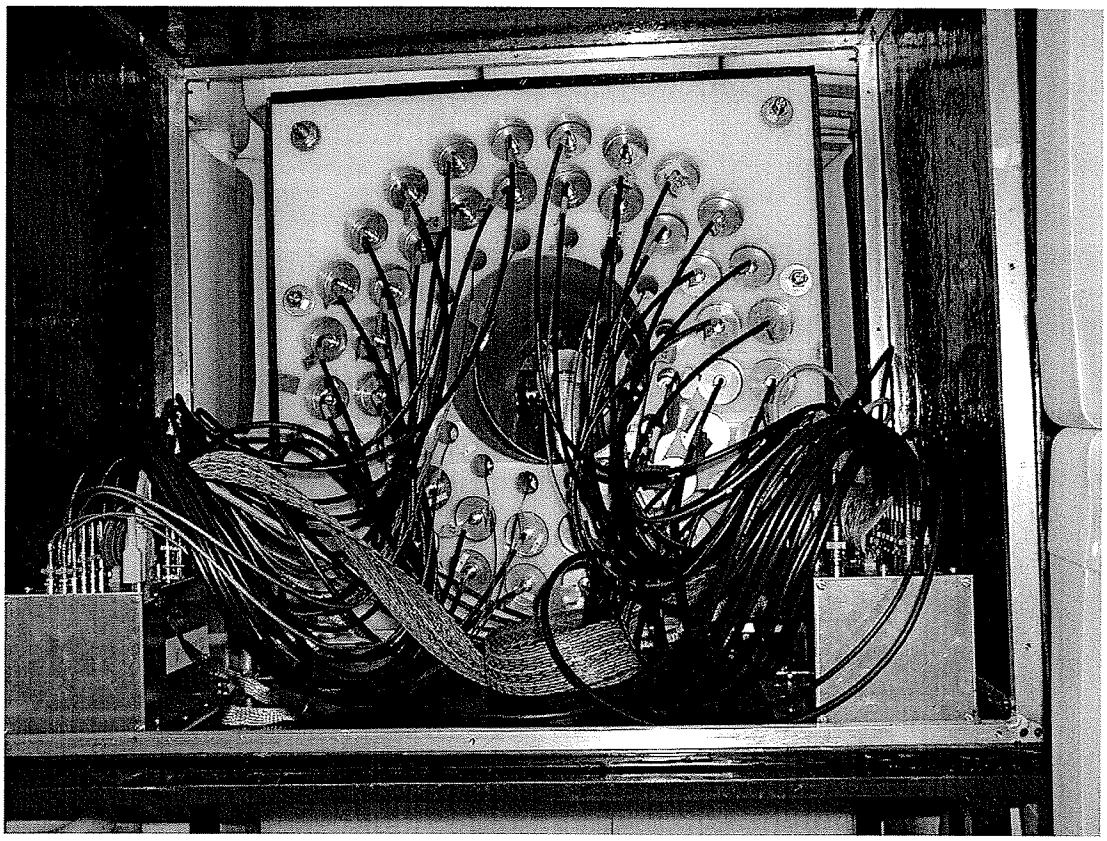

Figure 3.5: A close-up of NERO set up at Notre Dame. The ^{252}Cf source stand is inside the beamline hole, in front of the target holder.

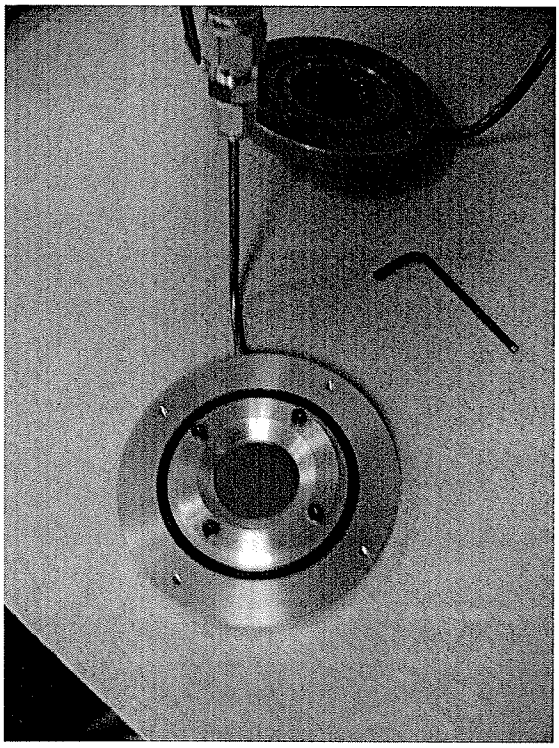

Figure 3.6: Target holder for Notre Dame calibration.

3.2 Resonant Reactions

For the $^{13}C(\alpha, n)$ and $^{11}B(\alpha, n)$ reactions, resonances were used. Setting the beam energy on resonances is adventageous for several reasons. On the resonance, the production of neutrons is dramatically increased, allowing many more counts in a shorter time, and overcoming background. Also, as long as the thickness of the target is much greater than the width of the resonance, the thickness of the target does not enter the calculation of the neutron production, and so the target thickness does not have to be known to extreme precision.

Two resonances each were chosen for ^{13}C and ^{11}B. The resonance energy partly defines the resulting neutron energy (see Figures 3.9 and 3.10). The center-of-mass neutron energy is calculated by:

$$E_n^{cm} = E_x - S_n \tag{3.2}$$

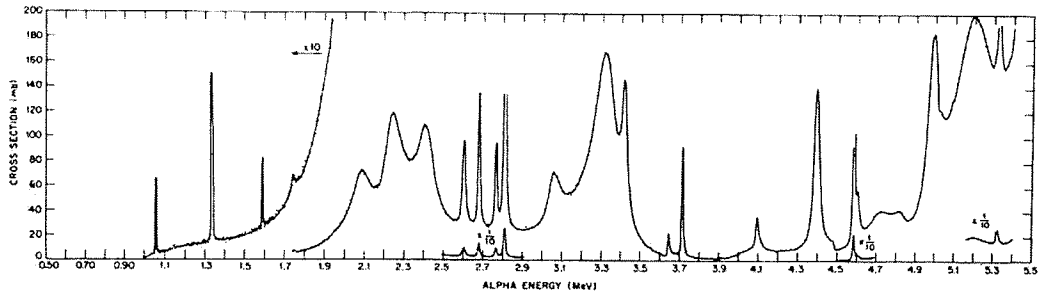

FIG. 3. These data show the $^{13}C(\alpha,n)^{16}O$ total neutron cross section. The target consisted of a layer of cracked (enriched) acetylene on a platinum backing. The target thickness was measured to be approximately 5 keV at the 1.057-MeV resonance. The energies are in the laboratory system and are corrected for target thickness. The cross-section scale is based on measurements made on the 1.057-MeV resonance using infinitely thick targets, of both enriched and natural elemental carbon, in conjunction with thin target measurements over this resonance and the wide resonance at about 2.4-MeV energy.

Figure 3.7: Figure 3 from p. 1358 Blair and Haas, 1973 (Reference [40]) showing total neutron cross section for ^{13}C.

where E_x is the excitation level in the compound nucleus to which the select resonance energy corresponds, and S_n is the neutron separation energy of the compound nucleus. The energies of the resonances were selected to provide appropriate points in the efficiency vs. energy graph. The resonances were also desired to be narrow and well-separated from other resonances in order to simplify the calculations required. For ^{13}C, the resonances at center-of-mass α-energies of 1.0563 MeV and 1.59 MeV were chosen, and for ^{11}B, the resonances at 0.606 MeV and the 2.063 MeV. (See Figures 3.7 and 3.8). Due to equipment problems during the 2.063 MeV ^{11}B resonance runs, good data was not collected, and this resonance could not be analyzed.

The above reactions have been studied previously, so the energies, widths, and strengths of these resonances are known, all of which enter into the calculation of the neutron production (see Table 3.3).

Targets of ^{13}C were produced of thickness 14 ± 2 $\mu g/cm^2$. Targets of ^{11}B were produced of thickness 12^{+4}_{-2} $\mu g/cm^2$. The targets were 1.5 in^2 squares of ^{13}C and ^{11}B evaporated on Ta backing. The ^{13}C target was enriched to 99% ^{13}C, and the ^{11}B was enriched to 99.71% ^{11}B.

The energy of the α beam was adjusted to scan across the resonance in order to map the resonance and locate the maximum yield. The beam was then set to the maximum yield for a certain amount of time. The incident beam current was

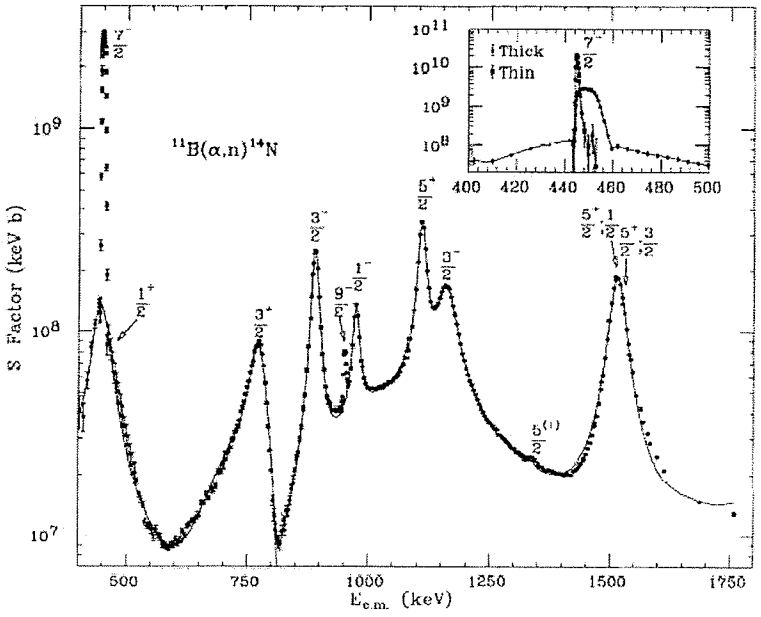

FIG. 2. S factor versus center-of-mass energy for the $^{11}B(\alpha,n)^{14}N$ reaction. The solid line above 820 keV represents a fit using six Breit-Wigner resonances plus a linear background, while the solid line below 820 keV represents a fit to the S factor using three Breit-Wigner resonances plus a linear background (see text). The solid lines in the inset are just a link of data points. The $J^{\pi};T$ assignments of the resonances are from Ajzenberg-Selove (Ref. 21), except for the $\frac{7}{2}^-$ state determined in the present work.

Figure 3.8: Figure 2 from p. 886 of Wang, Vogelaar and Kavanagh, 1991 (Reference [41]) showing S-factor for ^{11}B(α,n).

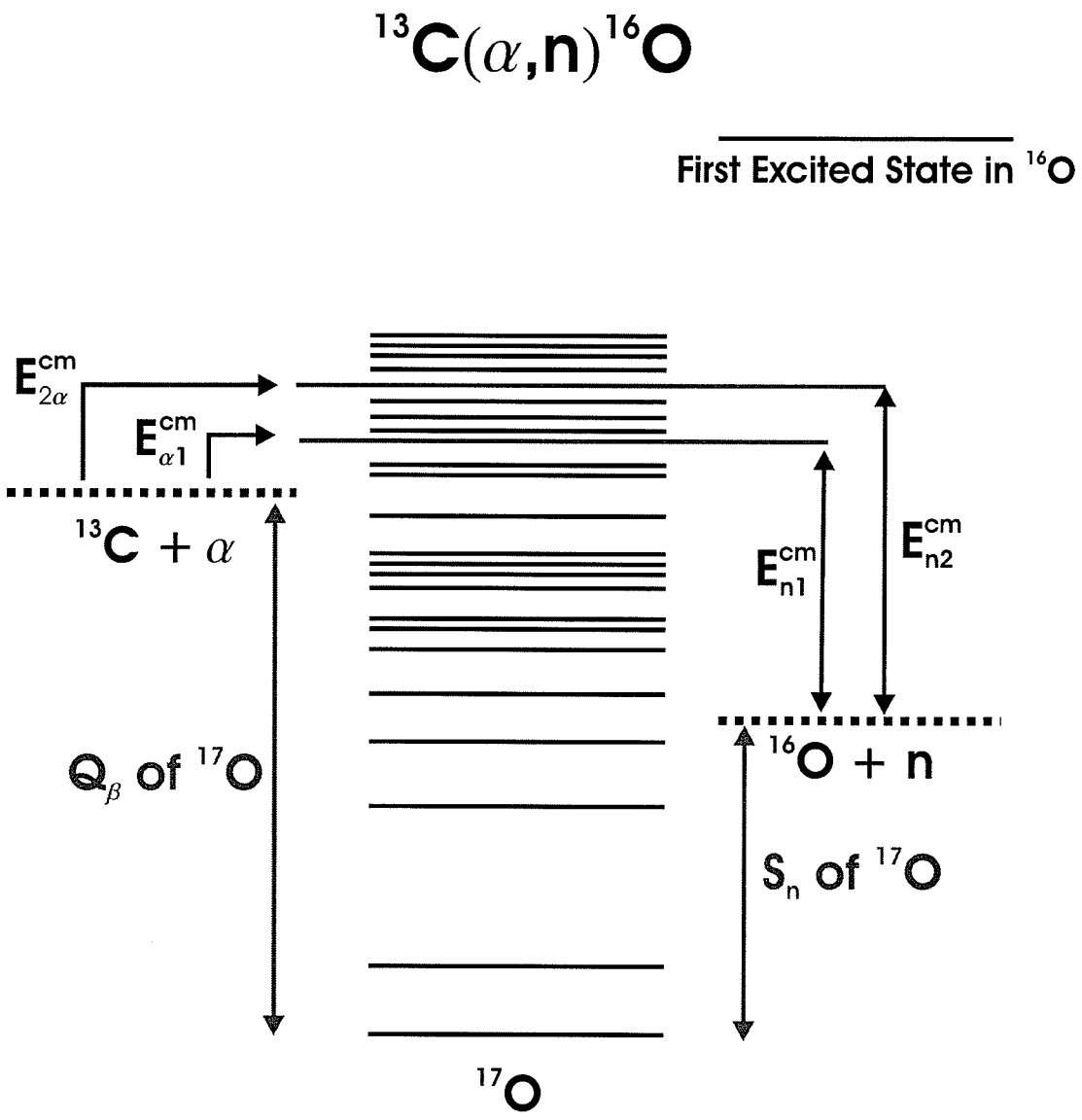

Figure 3.9: Energy diagram of the $^{13}C(\alpha,n)^{16}O$ reaction.

$^{11}B(\alpha,n)^{14}N$

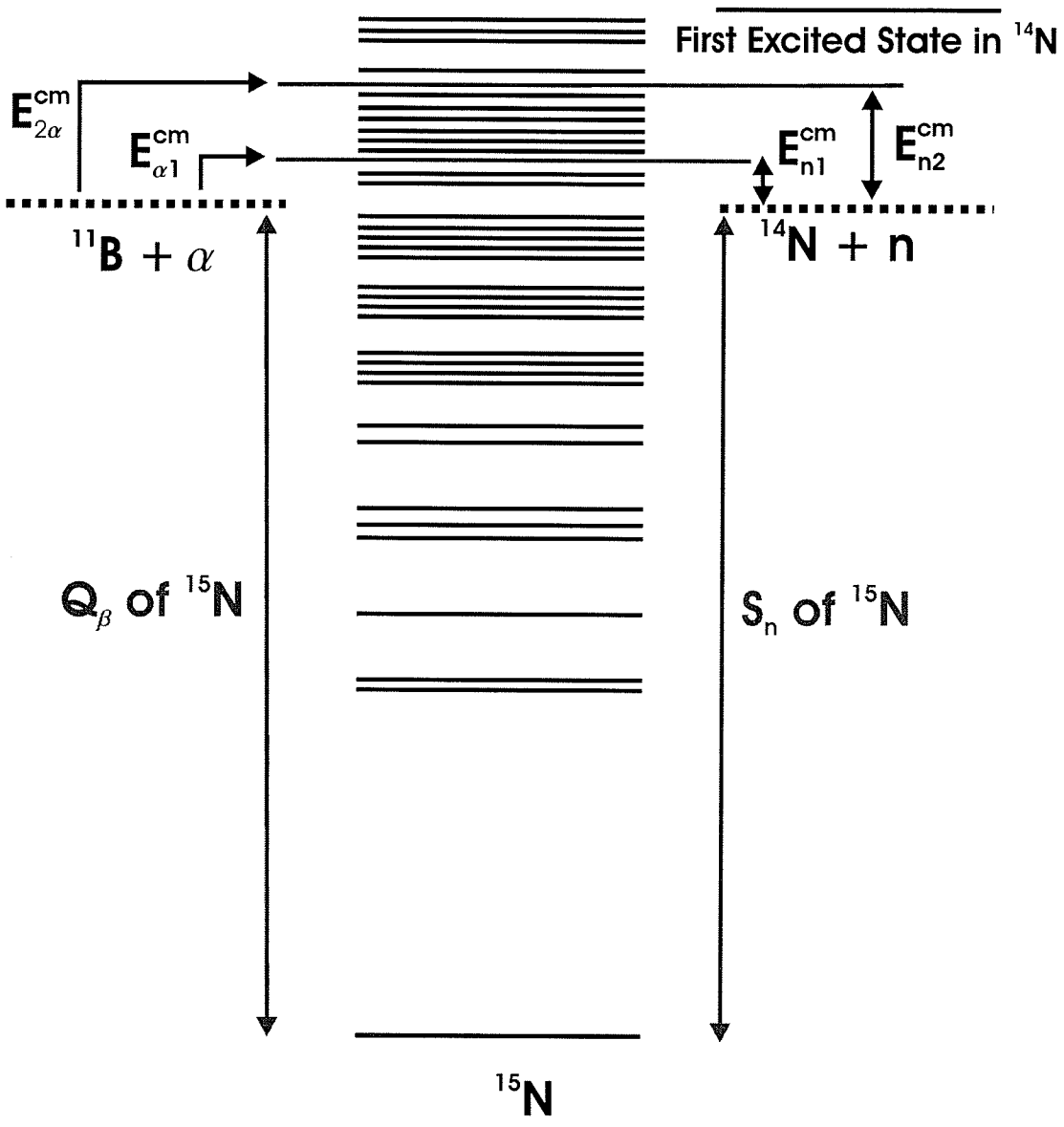

Figure 3.10: Energy diagram of the $^{11}B(\alpha,n)^{14}N$ reaction.

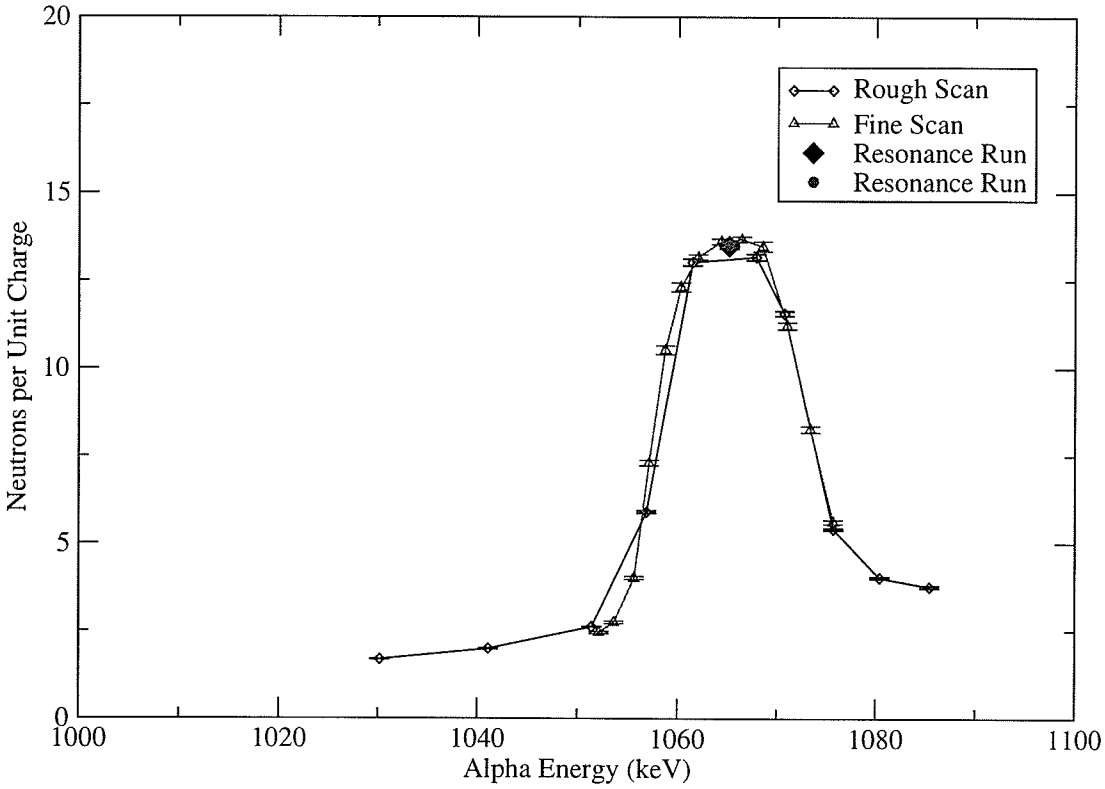

Figure 3.11: Scanning over the 1.053 MeV resonance in ^{13}C

measured on an isolated plate with electron suppression behind the target, providing a measurement of the incident rate.

3.2.1 Resonance Analysis

To derive the NERO efficiency, one needs the number N_d of neutrons detected at the resonance energy, and a calculation of the number of produced neutrons N_p. The background-corrected N'_d is simply:

$$N'_d = N_d - N_b \tag{3.3}$$

where N_b is the number of background neutrons. To find N_b, the resonances were scanned from well below to well above the resonance peak. Then a linear background was fit underneath the resonance peak and the background was subtracted from the

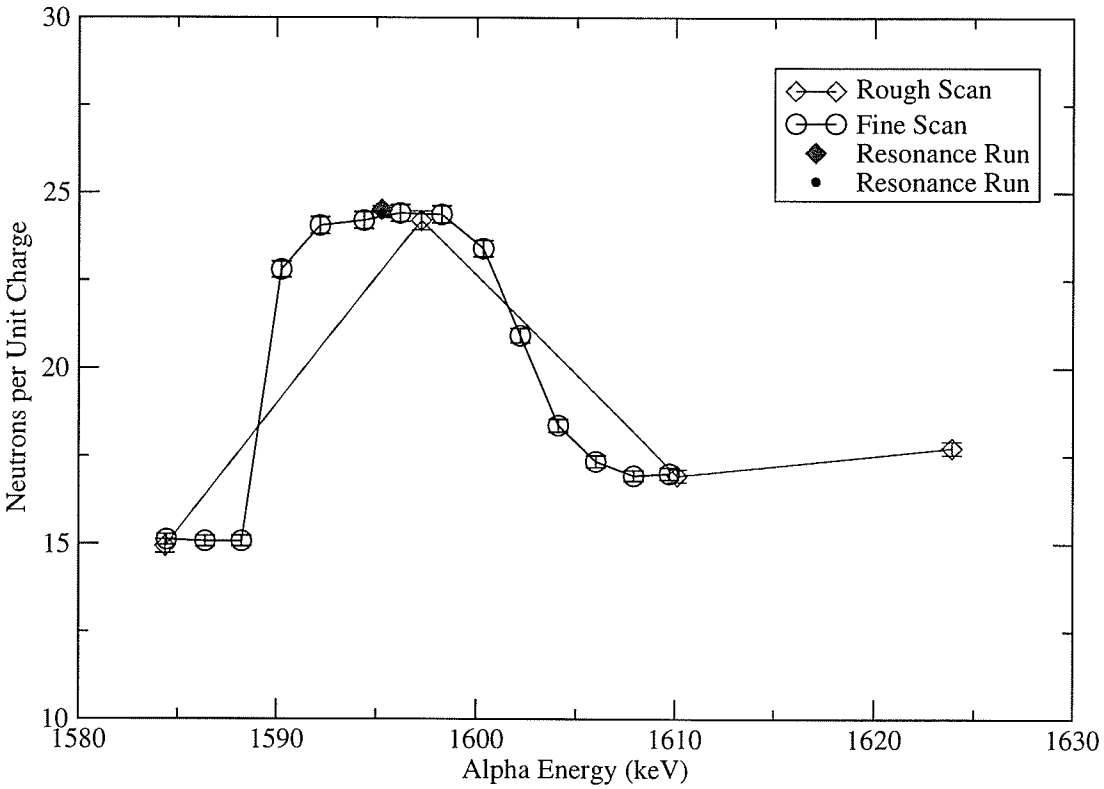

Figure 3.12: Scanning over the 1.5857 MeV resonance in ^{13}C

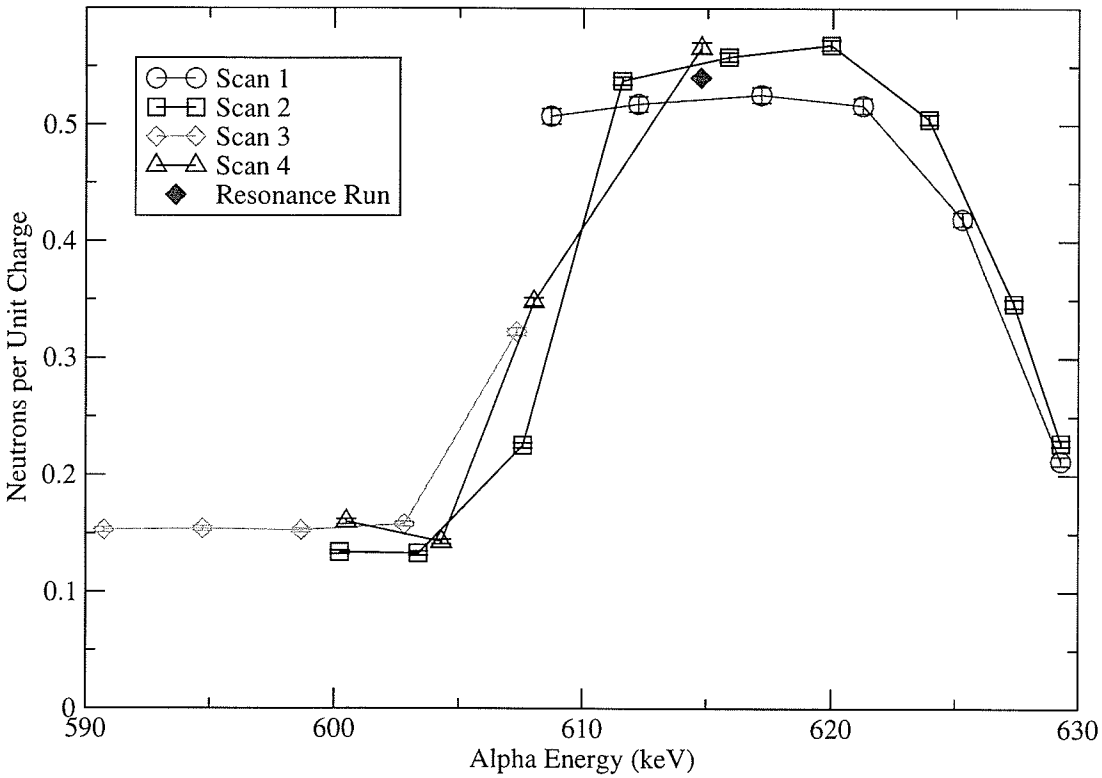

Figure 3.13: Scanning over the 0.606 MeV resonance in ^{11}B

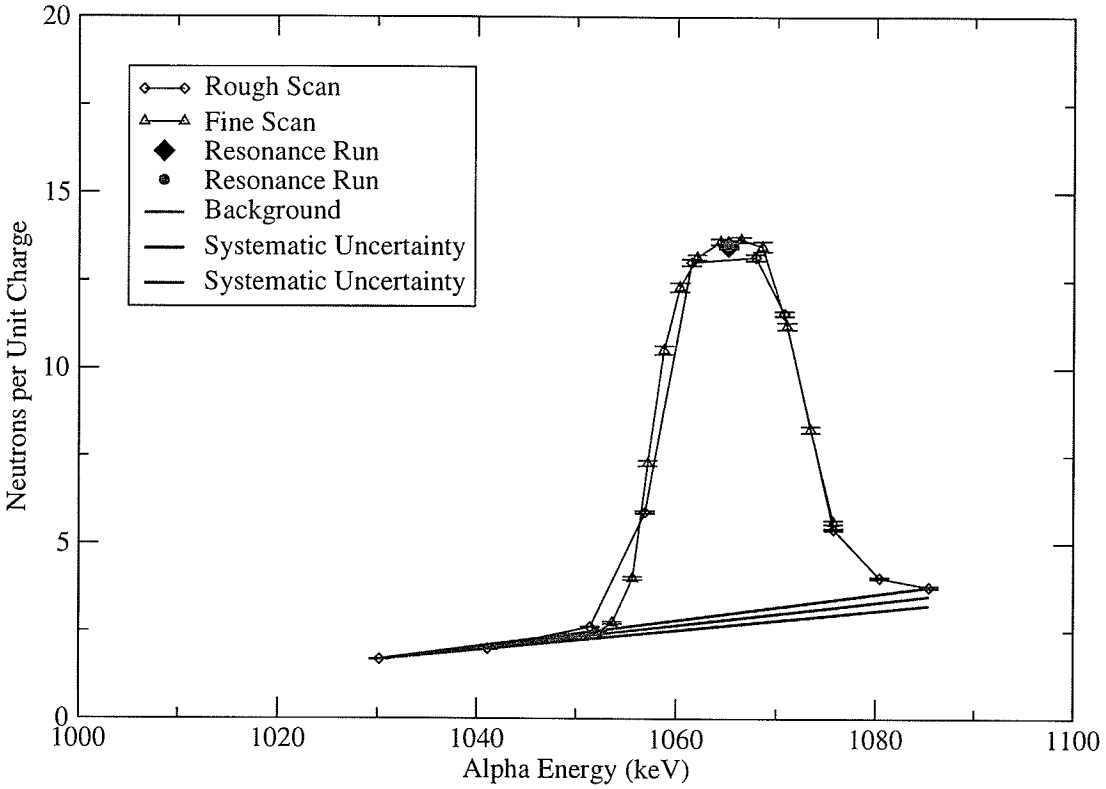

Figure 3.14: Linear Background subtraction for the 1.053 MeV resonance in ^{13}C

peak. This fitting removes both background and non-resonance counts, which must not be included in order to use the resonance peak formalism to calculate the number of neutrons produced by sitting on a resonance.

The number of produced neutrons, N_p, was calculated using the equation (see Reference [42]):

$$N_p = N_I \sigma n_a = N_I \sigma n t \tag{3.4}$$

where N_I is the number of incident particles, σ is the cross-section for the reaction, n_a is the areal target density, or number of target nuclei per unit area, n is the target number density, or number of nuclei per unit volume, and t is the thickness of the target. σ depends on the energy of the beam and therefore on depth x in the target, since the beam loses energy as it passes through the target. The number of neutrons

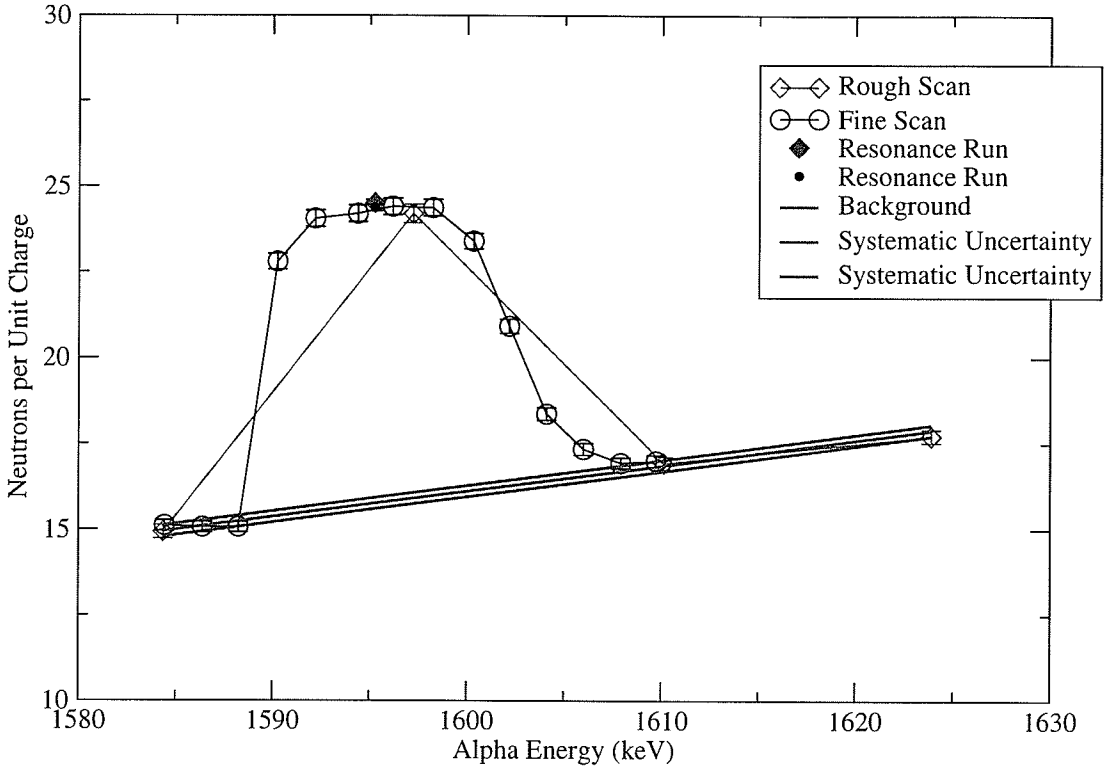

Figure 3.15: Linear Background subtraction for the 1.5857 MeV resonance in ^{13}C

produced at a particular depth x in the target is:

$$dN_p = N_I \sigma(E) n dx \tag{3.5}$$

where E is the energy at depth x. The number of neutrons produced through the target is:

$$N_p = \int dN_p = N_I n \int_{x=0}^{x=t} dx \sigma(E) \tag{3.6}$$

This can be expressed as an integration over energy. Changing variables of integration gives:

$$N_p = N_I n \int_{E_o}^{E_t} dE \frac{dx}{dE} \sigma(E) \tag{3.7}$$

where $\frac{dE}{dx}$ is the stopping power of the target material. In the "thin target approximation" [43], the stopping power is essentially constant in E or x, and so it can be pulled out of the integral, leaving the integral:

$$I = \int_{E_o}^{E_t} dE \sigma(E) \tag{3.8}$$

to be calculated.

One must remember to use the stopping power in the appropriate frame (see Section 3.2.2). Here we chose to calculate in the center-of-mass since the resonance strength is usually given in center-of-mass.

3.2.2 Narrow Resonances

If the resonance is broad relative to the target thickness, the integral I must be carried out over the thickness of the target, and the result is then sensitive to the limits of integration. If the resonance is narrow relative to the target (narrow being defined as the width of the resonance is much less than the energy loss in the target), then the

Table 3.1: Stopping Power of Targets.

Target	E_{res} LAB (MeV)	$\frac{dE}{dx}_{LAB}$ (MeV/mg/cm2)	$\frac{dE}{dx}_{CM}$ (MeV/mg/cm2)
^{13}C	1.053	1.722	1.318
^{13}C	1.585	1.451	1.110
^{11}B	0.606	2.087	1.531

Table 3.2: Target thickness compared to resonance widths.

Target	E_{res} lab (MeV)	t (mg/cm2)	t_{CM} (keV)	Γ_{cm} (keV)	Narrow Resonance?
^{13}C	1.053	0.014	18	1.5 ± 0.2	yes
^{13}C	1.585	0.014	16	≤ 1	yes
^{11}B	0.606	0.012	18	$(2.5 \pm 0.5) \times 10^{-3}$	yes

integral becomes simply (see Ref. [43], p175):

$$I = \frac{\pi^2\hbar^2}{\mu E_R cm}\omega\gamma_{cm} \tag{3.9}$$

Then

$$N_p = \frac{N_I \rho N_A \pi^2 \hbar^2 c^2 \omega\gamma_{cm}}{\frac{dE}{dx}\mu c^2 m_a E_{Rcm}} \tag{3.10}$$

To see if the narrow resonance rules apply in our cases, the target thickness in energy was calculated using the program SRIM 2000, and these values were compared to the experimentally determined widths of the resonances from the literature. These values are found in Table 3.3. The SRIM-calculated target thicknesses are shown in Figure 3.16. The comparison is shown in Table 3.2. As can be seen from the table, both resonances in ^{13}C and the 0.606 MeV resonance in ^{11}B are narrow relative to the targets.

The values for the resonance energies and strengths were taken from experimentally derived values from the literature: the resonance energies and strenghts for ^{13}C from [44] and widths from [40], and the energies, strengths and widths for ^{11}B from [41]. (See Table 3.3).

The stopping power $\frac{dE}{dx}$ was calculated in SRIM 2000. The stopping power must

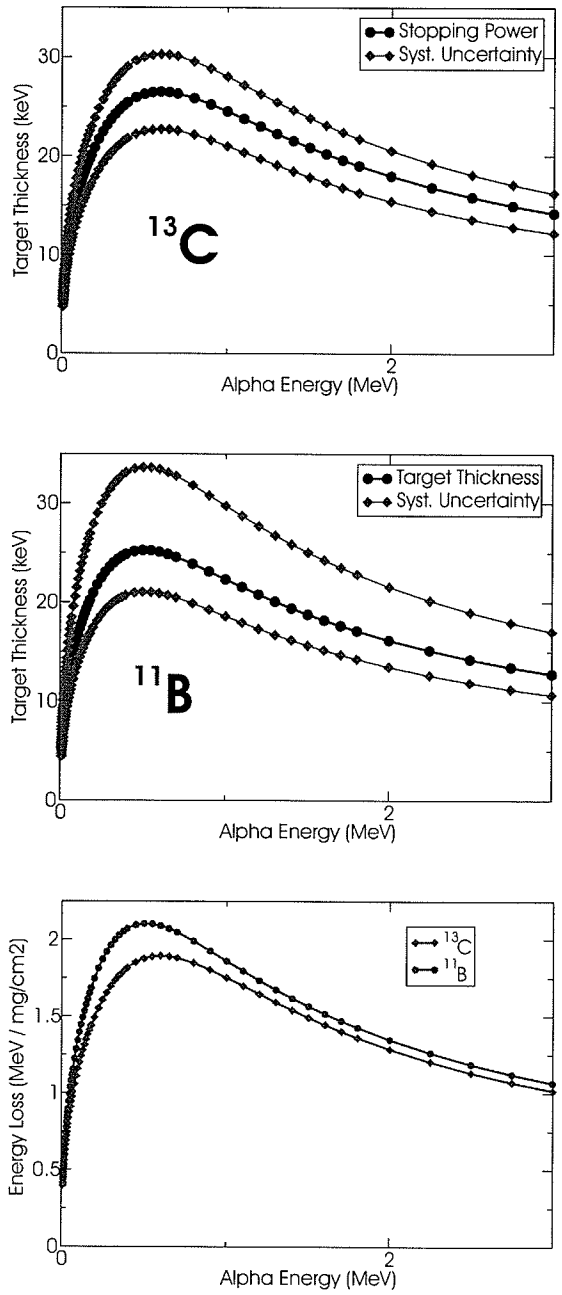

Figure 3.16: SRIM-calculated target thicknesses and energy-losses of the ^{13}C and ^{11}B targets in terms of the energy of the α projectile.

Table 3.3: Resonance Information Used in Calculations.

Target	E_α lab (keV)	E_α cm (keV)	Γ cm (keV)	$\omega\gamma$ cm (ev)	E_n cm (keV)
^{13}C	1053.18(18)		1.5 ± 0.2	11.9(6)	3022.37(83)
^{13}C	1585.7(15)		≤ 1	10.8(5)	3433(2)
^{11}B	606.0 ± 0.5	444.4 ± 0.4	$(2.5 \pm 0.5) \times 10^{-3}$	0.175 ± 0.010	604.3(7)
^{11}B	2063.7 ± 1.0	1513.5 ± 0.7	39 ± 4	$(7.9 \pm 0.7) \times 10^3$	1660(4)

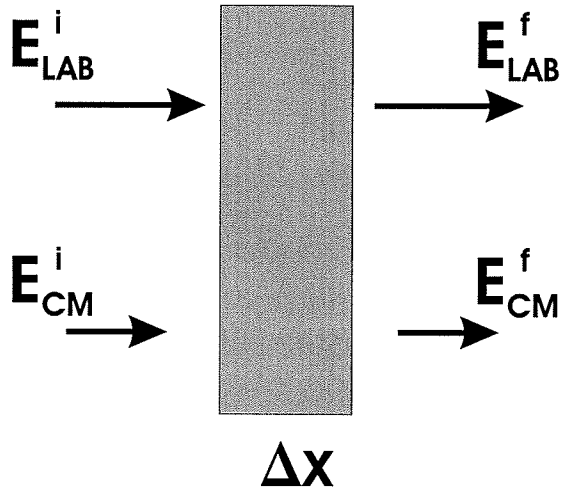

Figure 3.17: Stopping power of a target of thickness Δx in LAB and CM frames.

be in the center-of-mass frame if the integral is also calculated in center-of-mass. One does not take the curve from Figure 3.16 and find the stopping power at the center-of-mass energy of the incident α-particle. Rather, one uses the stopping power at the lab energy and converts it into a center-of-mass stopping power. Consider:

$$\left(\frac{dE}{dx}\right)_{LAB} = \frac{E^f_{LAB} - E^i_{LAB}}{\Delta x} \tag{3.11}$$

and

$$\left(\frac{dE}{dx}\right)_{CM} = \frac{E^f_{CM} - E^i_{CM}}{\Delta x} \tag{3.12}$$

Since

$$E^i_{CM} = F E^i_{LAB} \tag{3.13}$$

and

$$E^f_{CM} = FE^f_{LAB} \tag{3.14}$$

then

$$\left(\frac{dE}{dx}\right)_{CM} = \frac{FE^f_{LAB} - FE^i_{LAB}}{\Delta x} = F\frac{E^f_{LAB} - E^i_{LAB}}{\Delta x} = F\left(\frac{dE}{dx}\right)_{LAB} \tag{3.15}$$

where

$$F = \frac{m_{target}}{m_{target} + m_{projectile}} \tag{3.16}$$

3.2.3 Neutron Energy

The energies produced via the resonance reactions were calculated based on Equation 3.2. The center-of-mass energies were converted to lab frame energies. The central value was taken to be the lab frame energy at 90^o relative to the beam axis. The uncertainty included the uncertainties in the excitation energy and neutron seperation energy of the compound nucleus. In the lab frame, the energy of the neutron depends on the angle at which the neutron is emitted. Since the information on the angle of emission of the neutrons is lost in NERO, an additional uncertainty in the lab-frame energy range was taken as the lab frame value from 0^o to 180^o.

3.3 Summary of Resonance Analysis

Table 3.4 gives the neutron energies and corresponding NERO efficiencies for the resonance analysis. In the case of the two ^{13}C resonances, more than one measurement was taken. The result given is the weighted average of the various measurements.

Table 3.4: Results of Resonance Analysis.

Target	Resonance (MeV)	Neutron Energy (lab) MeV	Efficiency %
^{11}B	0.606	0.6 ± 0.2	33.2 ± 2.5
^{13}C	1.053	3.0 ± 0.4	24.4 ± 1.3
^{13}C	1.585	3.4 ± 0.6	27.6 ± 1.5

3.4 Non-resonant cross section: ^{51}V(p,n) reaction

This method does not depend on a calculation of neutron production from information about resonances, but rather is a more direct counting method. This method has been used previously for neutron detector calibrations [45, 46].

A proton beam was accelerated at the KN and impinged on the ^{51}V targets at the target position of NERO. For this reaction, an area of the known cross-section curve was chosen where there are no resonances. Neutrons produced in the reaction are counted by NERO.

For every ^{51}V(p,n)^{51}Cr reaction that occurs in the target, a radioactive ^{51}Cr isotope is created. Consequently, the number of neutrons produced is equal to the number of ^{51}Cr produced. ^{51}Cr decays by the emission of gamma rays. Therefore, if the activity of the target after irradiation is measured, then one can calculate the number of neutrons that were produced. ^{51}V was specifically chosen because ^{51}Cr has a relatively long half-life of 27.7025(24) days (NuDat). Once the target was irradiated, it was removed from NERO and taken to an offline gamma counting station where the activity was measured. ^{51}Cr decays by electron capture (EC). It emits several X-rays, and one gamma-ray, at 320.0824(4) keV (NuDat), with a branching to that gamma-ray of 9.92% (NuDat).

For this calibration, three beam energies were used: 1.8, 2.14, and 2.27 MeV (See Table 3.10 for the corresponding neutron energies). A new target was used for each energy.

The offline detector was an HPGe detector. The irradiated target was placed on a plastic backplate and mounted in front of the Ge detector at a specific distance,

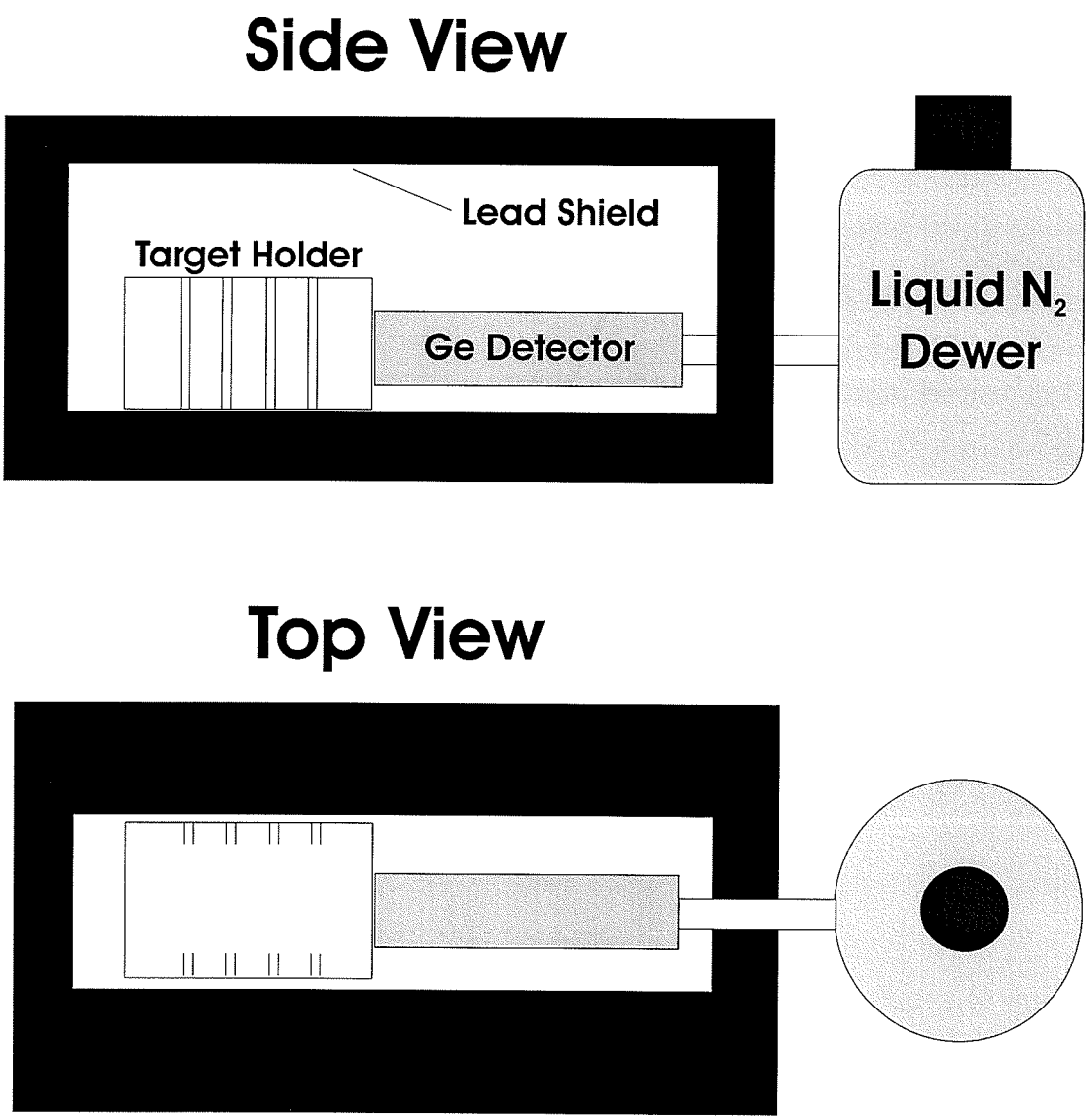

Figure 3.18: Schematic drawing of the offline counting station.

Table 3.5: Irradiation of ^{51}V targets.

Target	E_p lab (MeV)	Irradiation Time (s)	Integrated Current (C)	Neutrons Detected
1	1.8	30256	6.93×10^{-2}	111493686
2	2.14	13546	4.03×10^{-2}	154921397
3	2.27	11359	2.56×10^{-2}	266224751

Table 3.6: Offline counting of ^{51}V targets.

Target	E_p lab (MeV)	γ measuring live-time (s)	Detected γs
1	1.8	14892	1028
2	2.14	29224	3138
3	2.27	78586	13712

surrounded by lead shielding (See Figure 3.18). The activity of the target was measured once for a duration of several hours. Irradiation times, the time between the end of the irradiation and the beginning of the off-line counting (less than 4 hours) and the off-line counting times were short compared to the ^{51}Cr half-life, and any decay losses can therefore be neglected. The number of neutrons produced, N_p, can then be calculated simply with:

$$N_p = N_{Cr} = \frac{A_{Cr}}{\lambda_{Cr}} \tag{3.17}$$

where A_{Cr} and λ_{Cr} are the activity and decay constant of ^{51}Cr. The activity is found by:

$$A_{Cr} = \frac{P_{320keV}}{\lambda_{Cr} t_L b_{320keV} \epsilon_\gamma} \tag{3.18}$$

where P_{320keV} and b_{320keV} are the area under, and the branching to the 320 keV ^{51}Cr gamma peak in the offline counting, and t_L is the live time of the offline counting. The X-rays from the decay are at too low energies to enter the detector through the detector end-cap. ϵ_γ is the efficiency of the gamma detector.

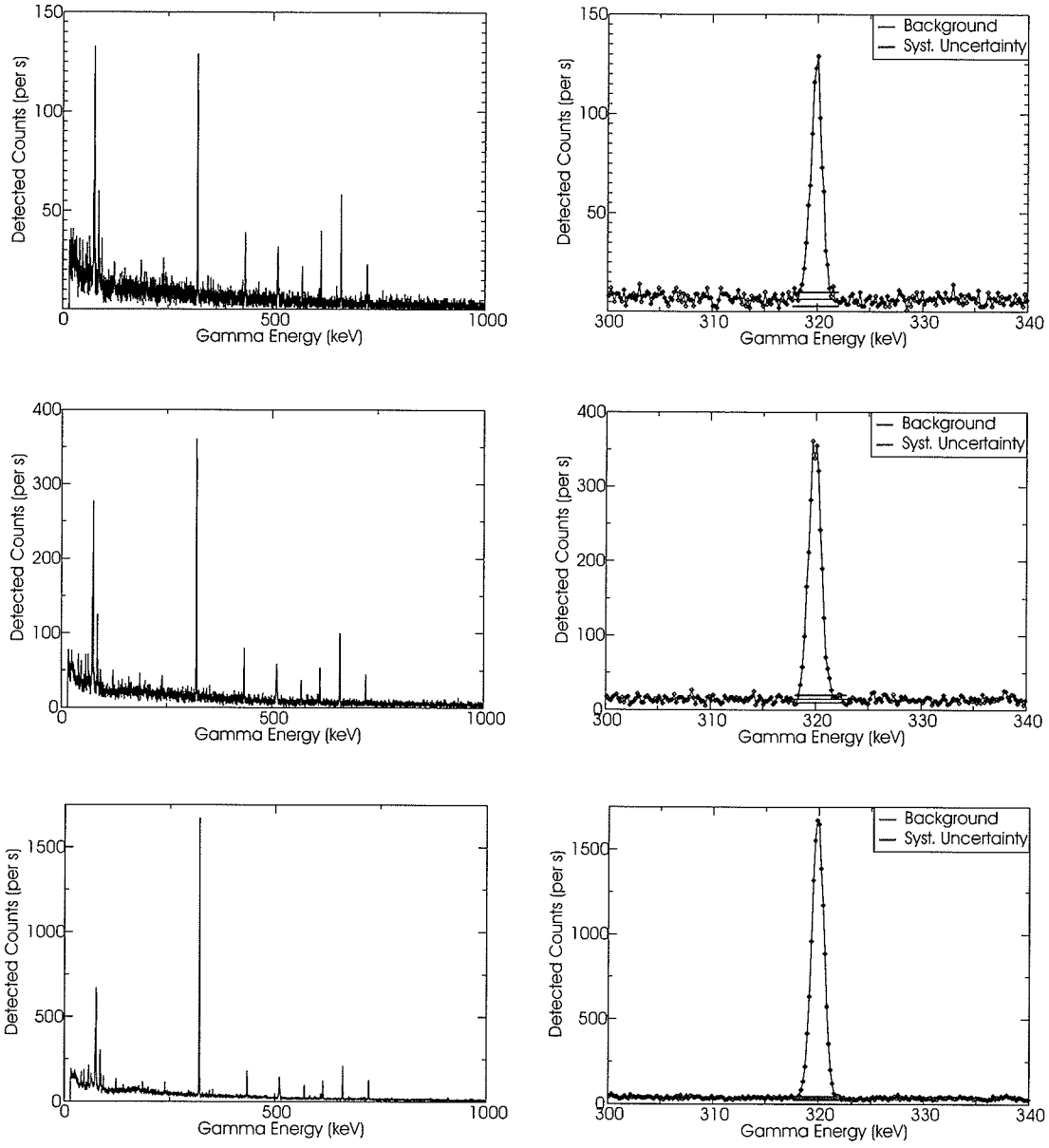

Figure 3.19: The ^{51}Cr gamma spectra and 320 keV peaks from targets irradiated by 1.8, 2.14, and 2.27 MeV protons.

3.4.1 Offline Counting Ge Detector Efficiency

The efficiency of the gamma detector depends both on distance from the source to the detector, and on the energy of the γ-ray. We determined the efficiency of the detector for a 320keV gamma ray at a specific distance by means of a calibation source.

The calibration source used was ^{133}Ba. The activity of this source had been measured precisely on April 1, 1981, 1200 GMT to be 11.65μCi with a 4.8% uncertainty. The current activity was found using

$$A(t) = A_o e^{-\lambda t} \tag{3.19}$$

The calibration source was placed at the same location as the active targets were placed. The efficiency was measured for several energies (the energies corresponding to the energies of the γ-rays of the calibration source). Since ^{133}Ba has gamma energies just above and below 320keV, the efficiency for 320keV could then be linearly interpolated between the 302keV and 356keV γ-rays from ^{133}Ba.

$$\epsilon_\gamma = \frac{N_{Detected}}{N_{Calculated from Known Activity}} \tag{3.20}$$

Since ^{133}Ba has multiple γ-rays (see Figure 3.20), some in cascades, the effects of summing had to be quantified.

Summing in a gamma detector occurs when there are cascades of γ-rays in the decay of the source. In this case, multiple γ-rays would be emitted almost simultaneously. If the detector detects both of them, it will interpret them as one photon with an energy equal to the sum of the two photons.

Both the 302 keV and 356 keV gammas are part of cascades so it is necessary to quantify summing corrections for both. We follow Debertin and Helmer [47] for this correction. For simplification in notation, we also follow the numbering convention in that reference (see Table 3.7). Reference [47] derived C_8, the summing correction for

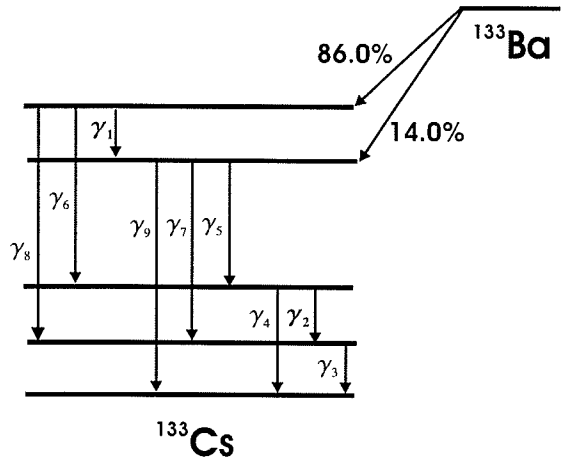

Figure 3.20: Decay diagram for ^{133}Ba. Diagram and numbering convention as found in Figure 4.25 of Reference [47].

Table 3.7: Numbering of ^{133}Ba γ-rays.

Number	Energy (keV)
1	53
2	80
3	81
4	161
5	223
6	276
7	303
8	356
9	384

$\gamma_8 = 356$ keV already. We take their expression, neglecting terms involving detection of X-rays, since the X-rays do not have enough energy to enter our detector. Our correction factor C_8 is then:

$$\frac{1}{C_8} = [1 - \frac{\epsilon_{t3}}{1+\alpha_3}] \times [1 + \frac{p_6 f_{62} \epsilon_2 \epsilon_6 + p_1 f_{17} \epsilon_1 \epsilon_7}{p_8 \epsilon_8}] \tag{3.21}$$

where α_i is the total internal-conversion coefficient, ϵ_i is the peak efficiency for the ith gamma, ϵ_{ti} is the total efficiency for the ith gamma, p_i is the gamma emission

probability for transition i, and

$$f_{62} = \frac{p_2}{p_2(1+\alpha_2) + p_4(1+\alpha_4)} \tag{3.22}$$

and

$$f_{62} = \frac{p_7}{p_5(1+\alpha_5) + p_7(1+\alpha_7) + p_9(1+\alpha_9)} \tag{3.23}$$

The factor C_7, the summing correction for γ_7 (303 keV) was derived based on similar arguments as those found in Ref. [47] for deriving C_8.

$$\frac{1}{C_7} = [1 - \frac{p_1}{p_7}\epsilon_{t1} - \frac{\epsilon_{t3}}{1+\alpha_3}] \times [1 + \frac{p_5 f_{52}\epsilon_5\epsilon_2}{p_7\epsilon_7}] \tag{3.24}$$

The total efficiencies ϵ_t were calculated as in [47].

$$\epsilon_t = \frac{1}{4\pi}\int(1 - e^{-\mu x})d\Omega \tag{3.25}$$

where μ is the attenuation coefficient of the detector material. The integration is over the solid angle subtended by the detector. In terms of the dimensions of the setup where R=radius of the crystal, t=thickness of the crystal, and d=distance from the source to the front face of the crystal:

$$\epsilon_t = [\frac{1}{4\pi}\int_0^{2\pi}\int_0^{\theta_2} d\Omega] - \frac{1}{2}[\int_0^{\theta_1} e^{-\frac{\mu t}{\cos\theta}}\sin\theta d\theta + \int_{\theta_1}^{\theta_2} e^{-\frac{\mu R}{\sin\theta}+\frac{\mu d}{\cos\theta}}\sin\theta d\theta] \tag{3.26}$$

where

$$\theta_1 = \arctan(\frac{R}{d+t}) \tag{3.27}$$

and

$$\theta_2 = \arctan(\frac{R}{d}) \tag{3.28}$$

Essentially, this efficiency is the solid-angle coverage of the detector, minus some loss due to gamma rays passing completely through the detector. Except for the sec-

Table 3.8: Ge crystal dimensions.

Dimension	Measurement (mm)
Diameter	55.9 ± 1
Crystal Length	52.7 ± 1
Front of Endcap to Crystal	0.3 ± 1
Source Holder to Endcap	746 ± 2

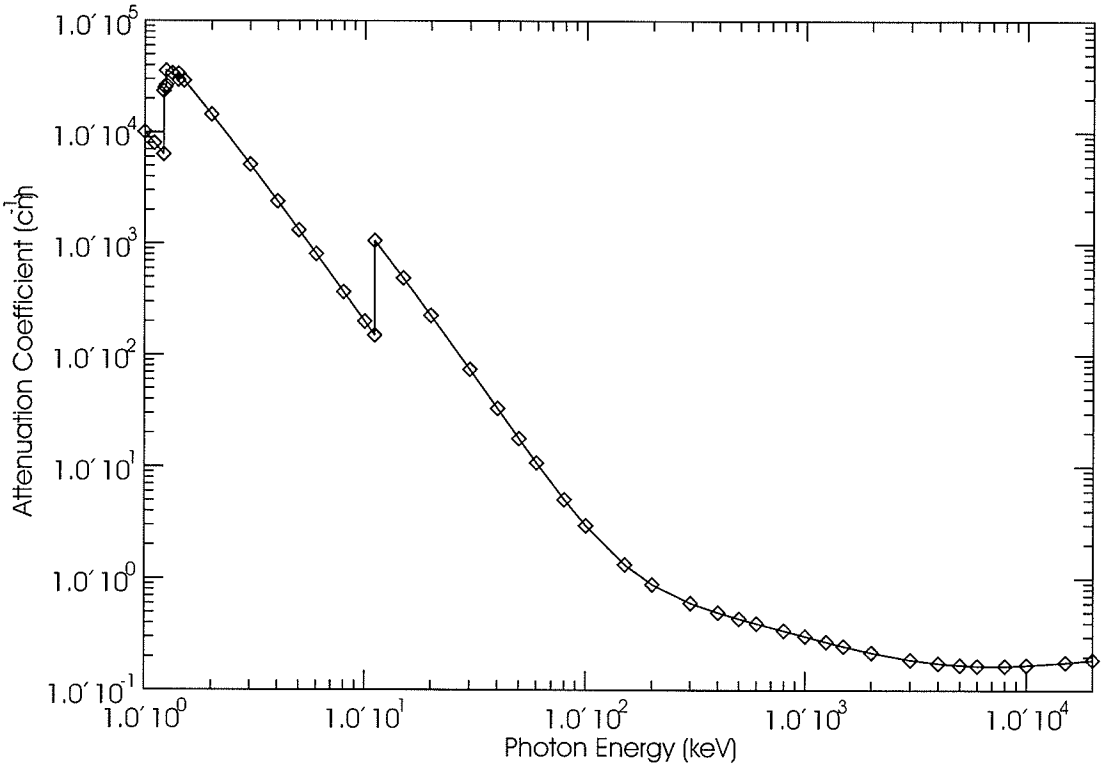

Figure 3.21: Germanium X-ray mass-attenuation coefficient μ from Ref. [48].

ond part, it is basically a geometrical calculation based on the dimensions of the detector and the distance to the source. For our energy range and setup, solid angle was by far the most important contribution. For this geometric calculation we used crystal dimensions from Table 3.8. The attenuation coefficients were taken from Reference [48]. The values from the reference were converted to units of cm^{-1} using a Ge density of $\rho = 5.323$ g/cm^3 and are plotted in Figures 3.21 and 3.22. The values at specific energies were linearly interpolated (See Table 3.9).

The calculated curve of total efficiency ϵ_t of the Ge as a function of photon energy

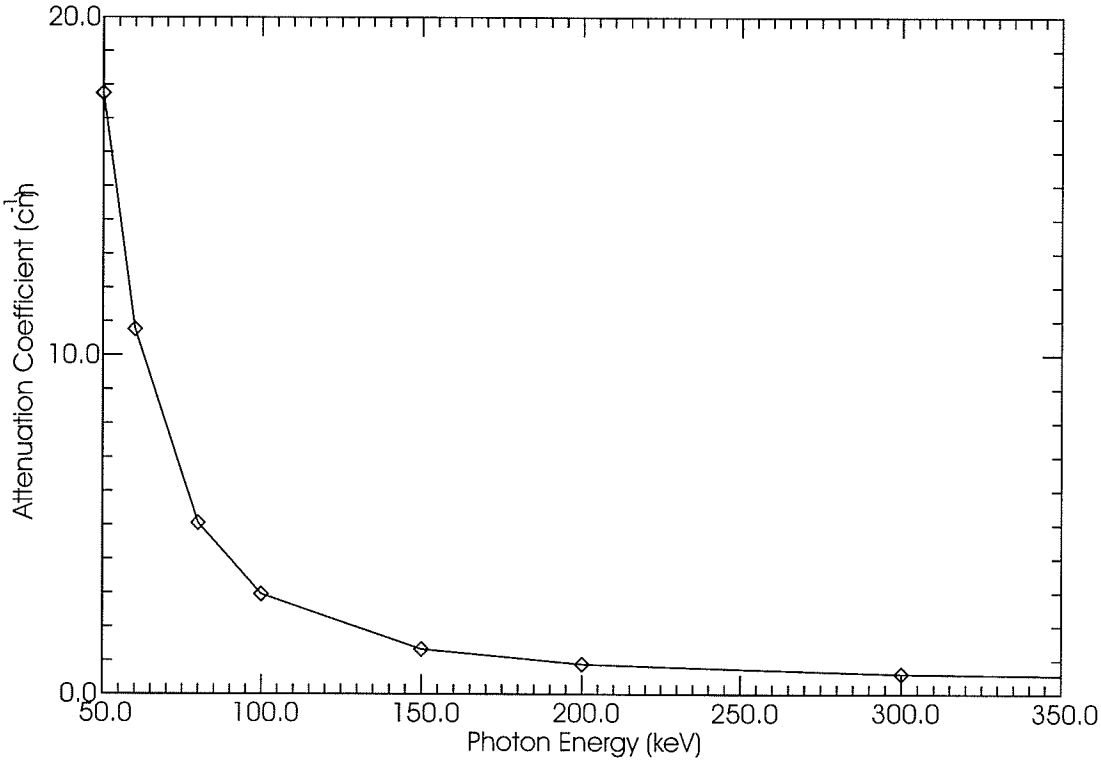

Figure 3.22: Germanium X-ray mass attenuation coefficient μ from Ref. [48], zoomed-in on region relevent to the calculation

Table 3.9: Germanium X-ray mass attenuation coefficients.

Photon Energy (keV)	Attenuation Coefficient μ (cm^{-1})
80	5.06
161	1.2318
223	0.81914
276	0.66968
303	0.59882
356	0.54264
384	0.51296

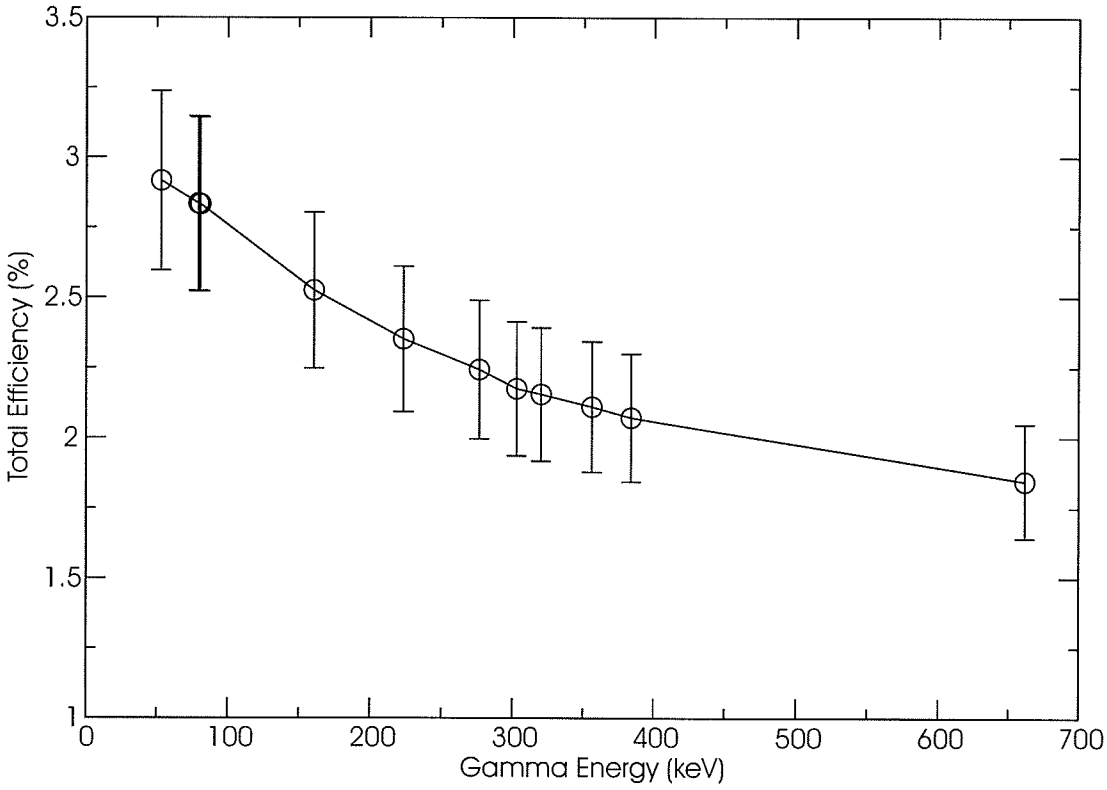

Figure 3.23: Total Efficiency curve for the Ge with the specific geometry of the offline counting station.

for our specific detector geometry is shown in Figure 3.23. The systematic uncertainty is due to the uncertainty in the crystal dimensions and source-crystal distance. The contribution to the efficiency of the term containing the mass attenuation coefficient is only on the order of 1%.

The peak efficiencies were determined experimentally by simply finding the background corrected counts in the various gamma peaks and comparing them to the

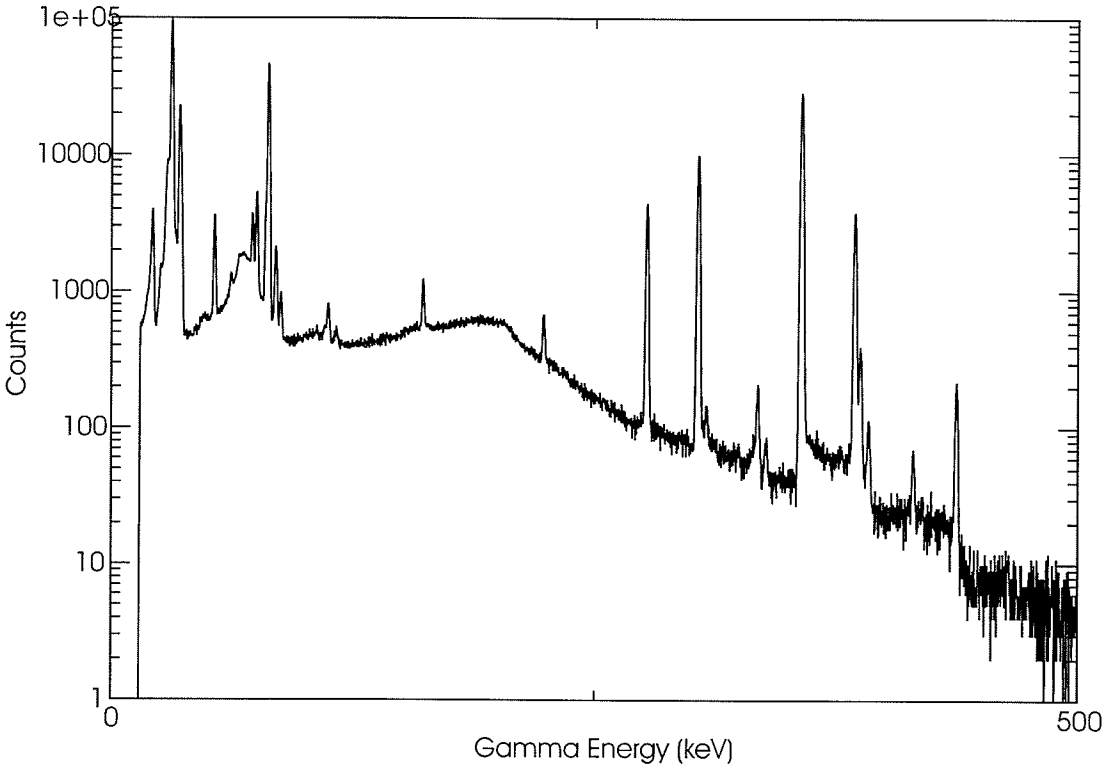

Figure 3.24: Gamma spectrum from the calibration source ^{133}Ba.

calculated peak count based on the known activity of the source and the known branchings.

The resulting summing corrections for the two ^{133}Ba calibration peaks were $C_7 = 1.0135 \pm 0.0015$ and $C_8 = 1.0091 \pm 0.0014$. In other words, the summing is a 1% effect. This level of effect is smaller than the effect due to the uncertainty in the calibration source activity, which is a 5% effect.

Next, the summing-corrected peak efficiencies for the ^{133}Ba calibration source were used to interpolate to the peak efficiency of the 320keV ^{51}Cr. The resulting ^{51}Cr peak efficiency is 0.0076 ± 0.0004.

Using this efficiency, the activity of each ^{51}Cr target was then calculated, and the number of neutrons produced in the $^{51}\mathrm{V}(p,n)^{51}\mathrm{Cr}$ reaction was calculated using equation 3.17. The number of neutrons detected was corrected for background using the background neutron rate measured in a separate run. The background rate was

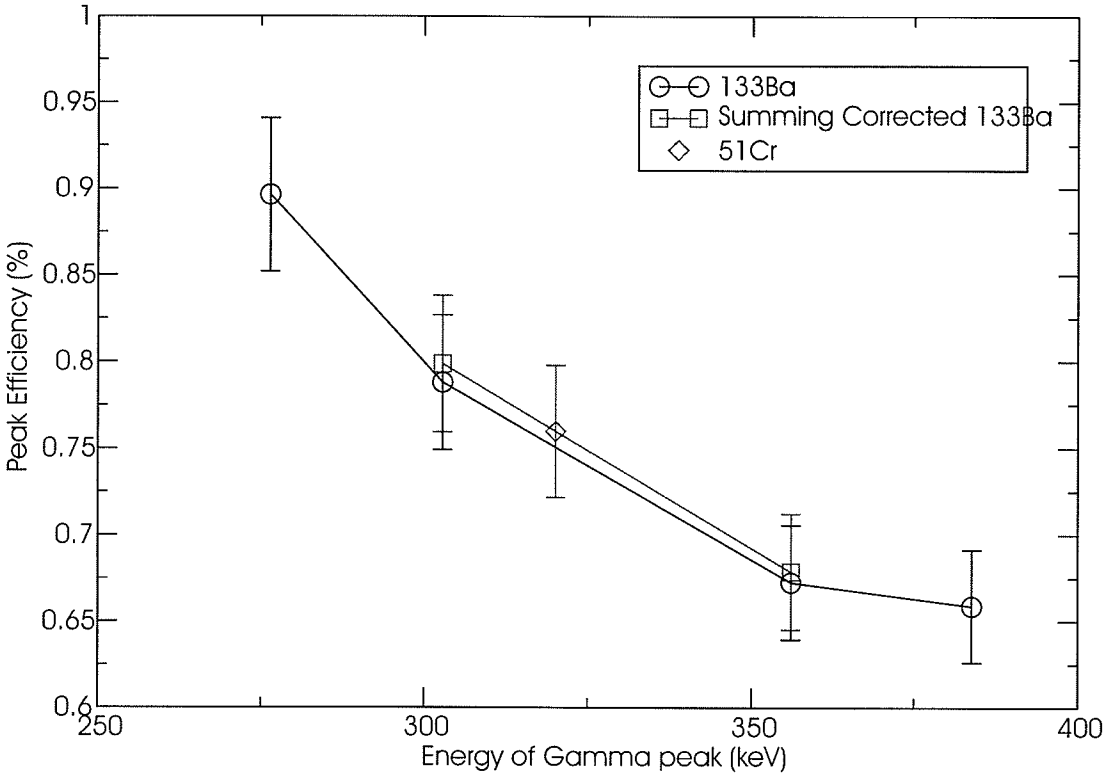

Figure 3.25: Interpolating the 320 keV peak efficiency of ^{51}Cr

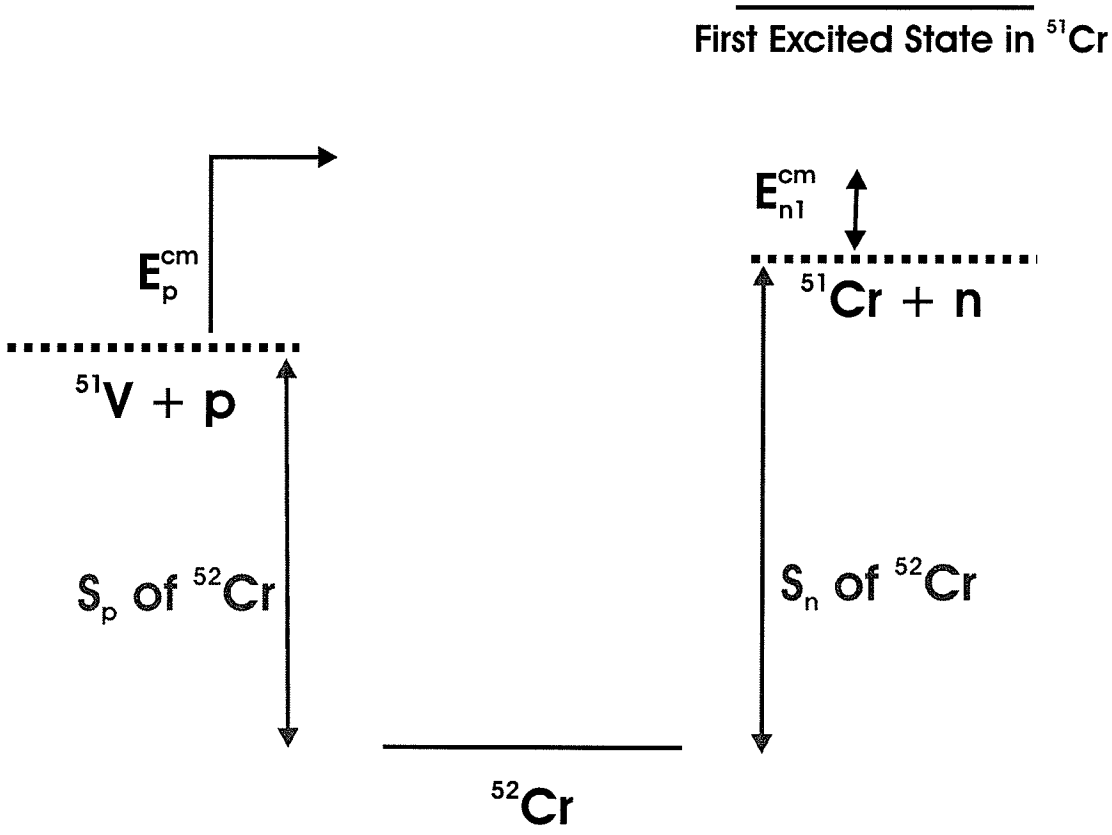

Figure 3.26: Diagram of the reaction ^{51}V(p,n)^{51}Cr.

determined to be 16.5±0.3 neutrons per second. The efficiency for neutron energies at corresponding proton beam energies of 1.8, 2.14 and 2.27 MeV were then calculated using equation 3.1. The resulting calculated efficiencies can be found in Table 3.10.

The energy of the neutrons produced was calculated as:

$$E_n^{CM} = S_p + E_p^{CM} - S_n \tag{3.29}$$

Table 3.10: NERO efficiencies for ^{51}V runs.

Proton Energy (keV)	Neutron Energy (MeV)	Efficiency (%)
1.8	230 ± 25	36.1 ± 2.3
2.14	564 ± 43	32.2 ± 1.8
2.27	692 ± 49	33.7 ± 1.8

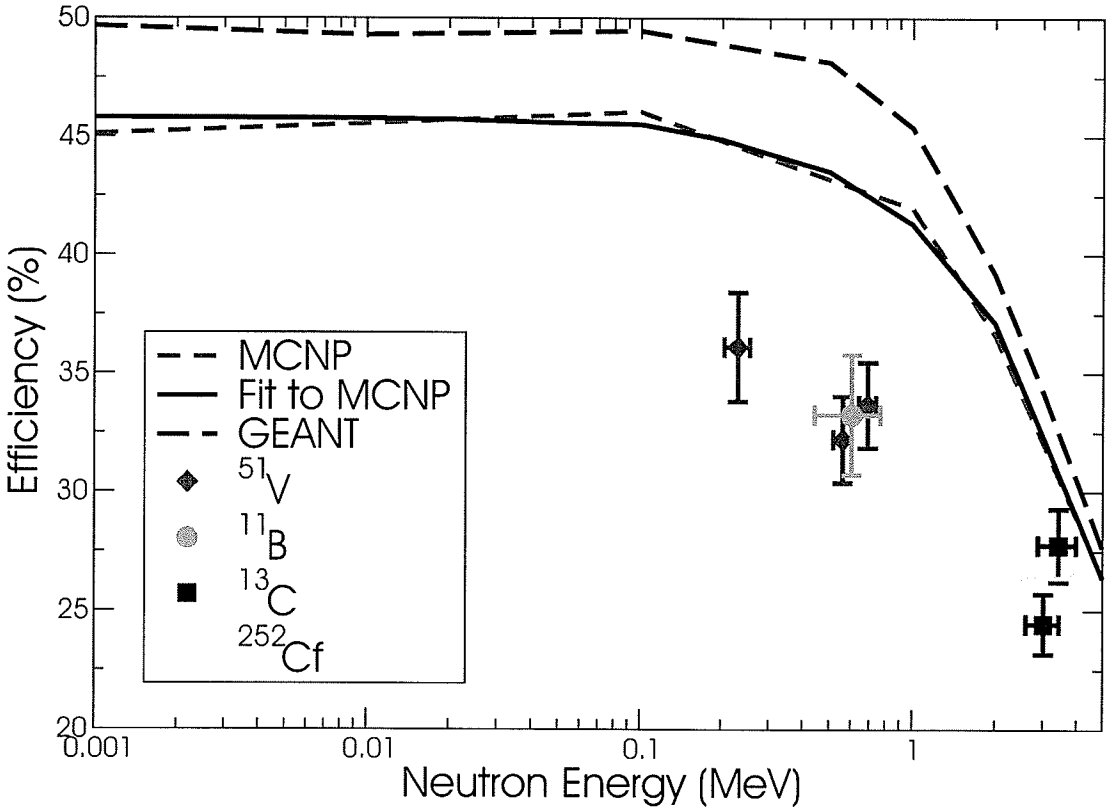

Figure 3.27: Experimental data from NERO efficiency calibration plotted with simulations from MCNP and GEANT.

3.5 Summary of NERO Efficiency Calibration

A summary of the NERO efficiency calibration is shown in Figure 3.27. Figure 3.28 gives the MCNP and calibration results ring by ring. The MCNP calculation is systematically higher than the experimental values. A GEANT4 simulation of NERO was carried out independently [49], and this simulation also resulted in a systematically higher efficiency curve. The cause of this difference is not clear. The fact that the shift applies to all rings argues against a general deterioration of counter gas since all

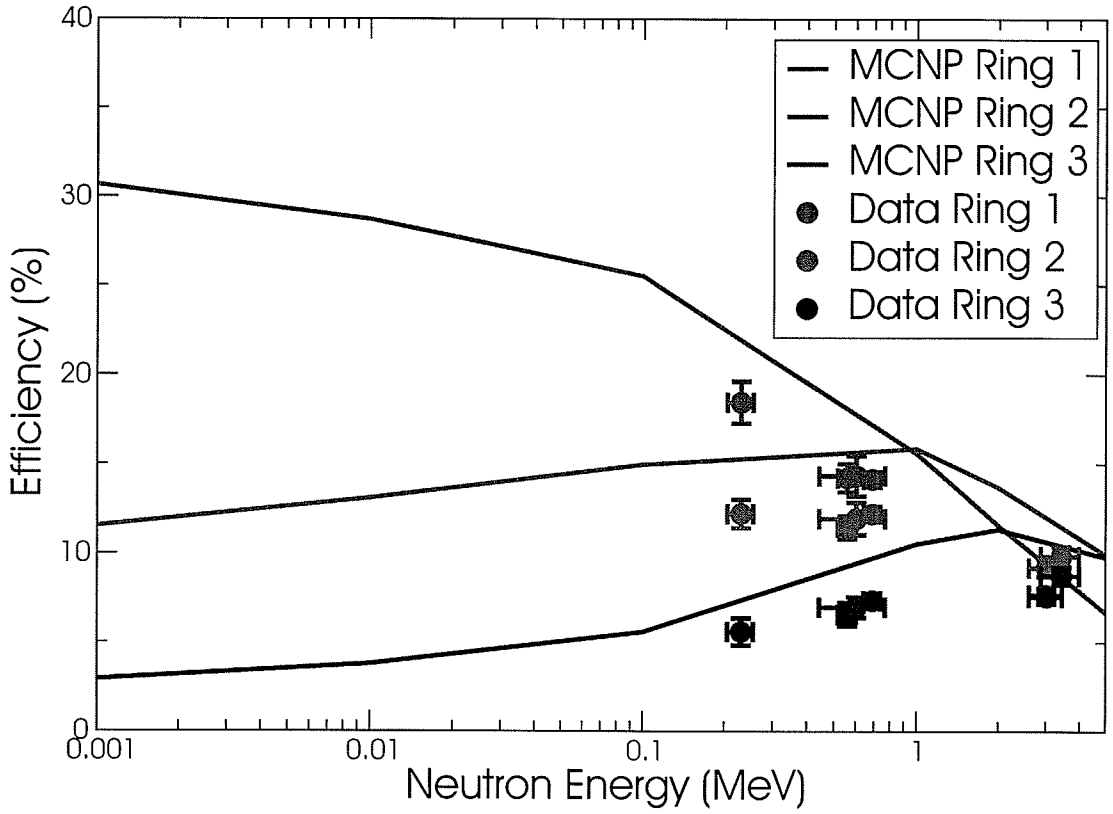

Figure 3.28: Experimental data from NERO efficiency calibration and MCNP calculations plotted by ring.

types of counters, which are of different types and come from various sources, would have to be deteriorated in a similar way. The density of polyethylene used in the codes is another possible source for the discrepency. However, the density of polyethylene used in NERO was well-specified and this value was used in the simulation.

In order to provide a fit to the data, the calculated MCNP efficiency curve was first fit with a second order polynomial. The resulting fit equation is:

$$Efficiency = 0.1519(Energy)^2 - 4.651(Energy) + 45.82 \tag{3.30}$$

where the efficiency is in % and neutron energy is in MeV. The curve was then fit to the data by χ^2 minimization allowing only the offset to vary. Using this method, a shift of -8.85895 was determined, resulting in a final fit curve of:

$$Efficiency = 0.1519(Energy)^2 - 4.651(Energy) + 36.96 \tag{3.31}$$

Figure 3.29 shows the calibration again with the shifted calculations curve.

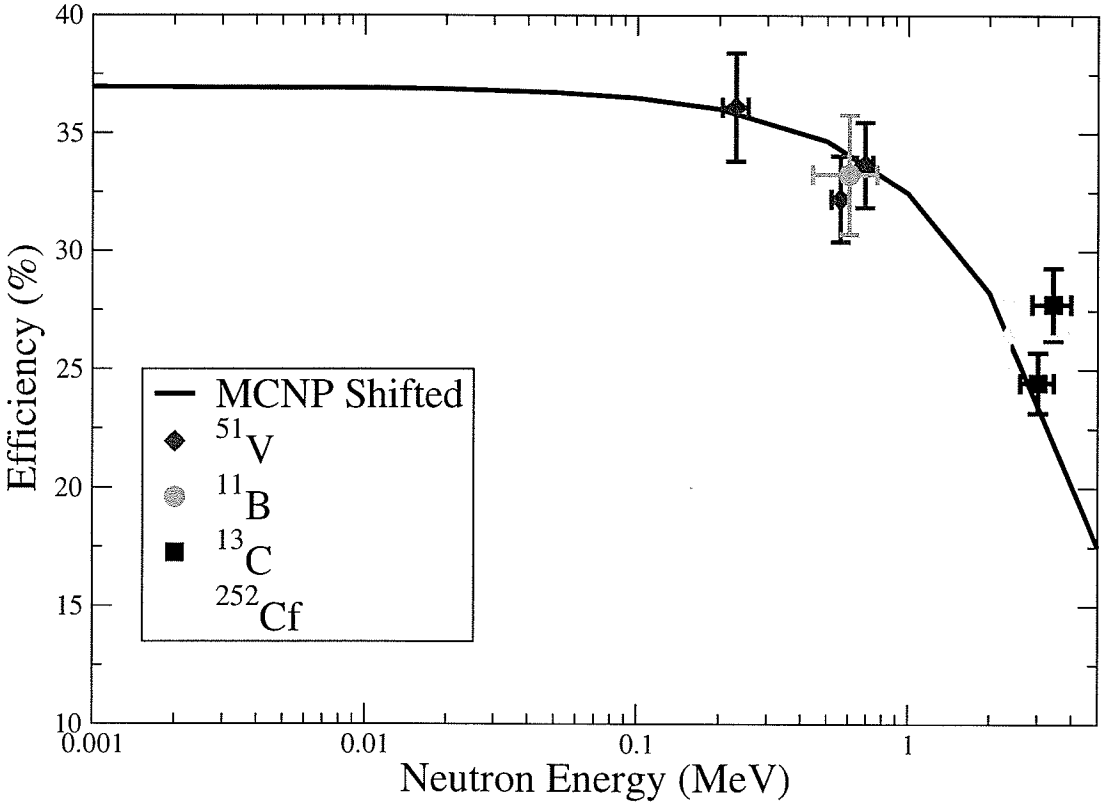

Figure 3.29: Experimental data from NERO efficiency calibration plotted with shifted MCNP calculated curve.

Chapter 4

Experiment

4.1 Introduction

The experiment to measure the half-lives and neutron emission probabilities of neutron-rich isotopes around ^{78}Ni was run at the Coupled Cyclotron Facility (CCF) of the National Superconducting Cyclotron Laboratory (NSCL) at Michigan State University, as NSCL experiment number 02028.

4.2 Experimental Setup

4.2.1 Fragment Production

The neutron rich isotopes were produced in the following manner. ^{86}Kr was accelerated in the K500 Cyclotron at the Coupled Cyclotron Facility (CCF) at the National Superconduction Cyclotron Laboratory (NSCL). After the K500, the ^{86}Kr beam passed through a thin stripper foil, and then was injected into the larger K1200 Cyclotron and accelerated to approximately 140 MeV/u. After extraction from the K1200 Cyclotron, the beam struck a thin Be production target of thickness 376 mg/cm^2, producing a secondary beam composed of a mix of neutron-rich isotopes via fast fragmentation. The average primary beam intensity was 15 pnA.

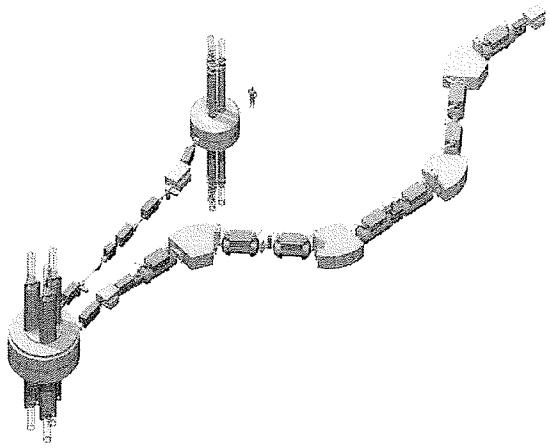

Figure 4.1: The coupled cyclotrons and the A1900 fragment separator.

4.2.2 Fragment Separation and Identification

The secondary beam of mixed fragments was then directed through the A1900 fragment separator. The A1900 fragment seperator is a series of 4 dipole magnets whose magnetic rigidity is set to allow to pass only the fragments of interest [50]. During the ^{78}Ni production runs, the A1900 was operating with full momentum acceptance. A position sensitve plastic scintillator at the dispersive intermediate focus was used to determine the momentum of each beam particle at typical rates of 10^5/s. A 100.9 mg/cm^2 achromatic Al equivalent degrader was placed at the intermediate image to clean the beam and increase transmission. The A1900 was first set to the ^{72}Ni secondary beam setting (Bρ_{12}=4.0611, Bρ_{34}=3.9509). Each nucleus in the secondary beam was individually identified in flight at the A1900 focal plane by energy-loss and time-of-flight measurements, in conjunction with the momentum measurement in the scintillator at the A1900 intermediate focus. The time of flight was measured using two plastic scintillators as start and stop. One of these scintillators was the scintillator at the intermediate image of the A1900 which was also used for momentum measuremnts, and the second scintillator was located at the focal plane of the A1900. In addition, isomers of ^{70}Ni were identified by a Ge detector at the focal plane, confirming the particle identification there.

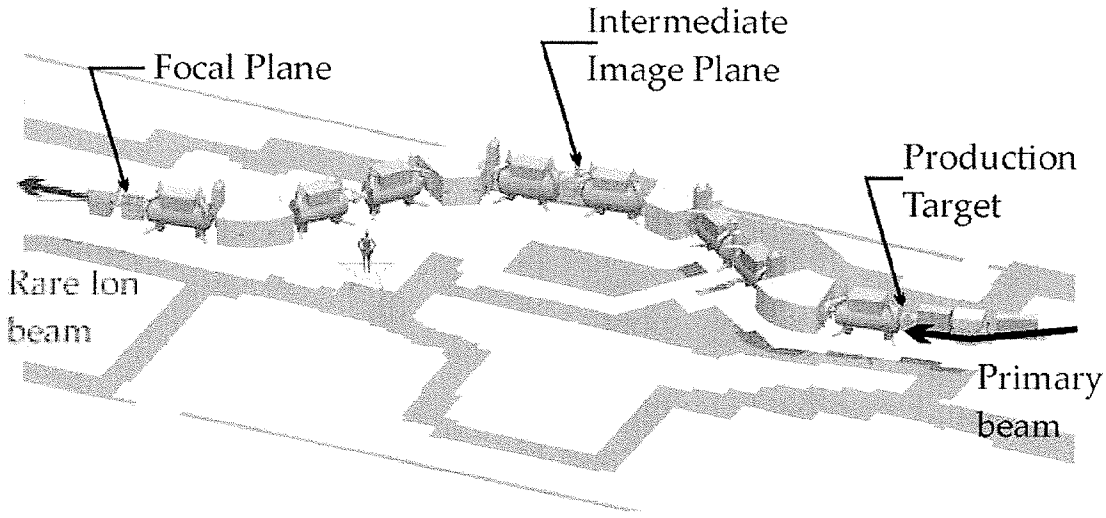

Figure 4.2: The A1900 fragment separator.

Next the particle identification had to be passed on to the detectors in the experimental vault. Degraded primary beam was sent first to the A1900 focal plane. Then the detectors at the focal plane of the A1900 were removed from the beamline and the degraded primary beam was sent to the experimental vault where the first energy-loss detector in the experimental vault (referred to as Pin1) was roughly calibrated to the A1900 energy loss detector. This, in conjunction with a time of flight measurement using the scintillator in the A1900 intermediate focus and a scintillator in the experimental vault, a separation of about 40 m, brings the particle identification to the vault.

4.2.3 Isomer Identification with SeGA

In order to further verify the particle identification in the experimental vault, the Segmented Germanium Array (SeGA) at the NSCL [51], an array of 32-fold segmented Ge detectors, was used to identify γ-peaks from known isomers of the implanted nuclei. This confirmation exploits the fact that several isotopes in this region are known to have microsecond isomers. Because of the relatively long lifetimes of these states, the

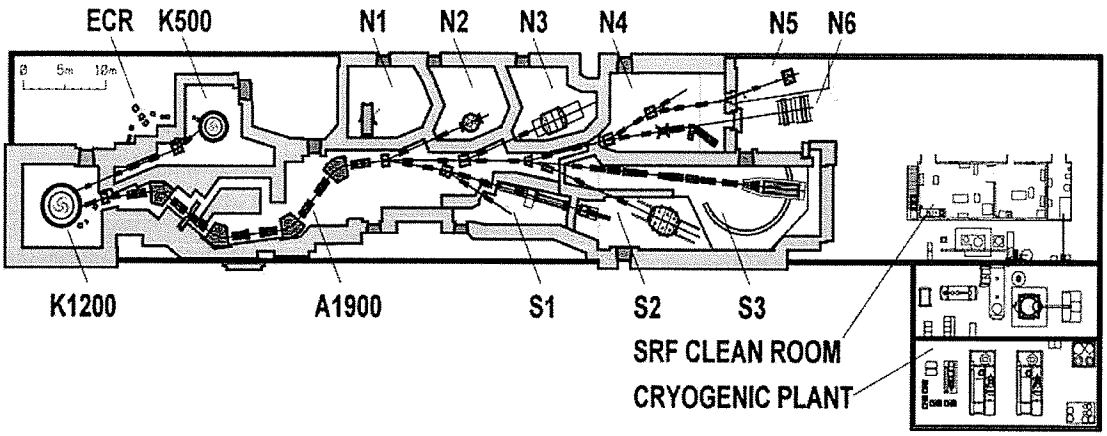

Figure 4.3: Floorplan of the NSCL.

isotopes can reach the experimental vault before they have decayed out of these states. The gammas from these decays can therefore be used in the experimental vault to identify some isotopes independent of energy-loss/time-of-flight. These isotopes can be used to confirm the energy-loss/time-of-flight identification.

For the isomer identification, a variable degrader in the vault upstream from the final β counting/NERO station was used as a separate implantation target station. SeGA was arranged around the degrader station in the "betaSeGA" configuration: 12 detectors at a distance of 8.5 cm from the target (see Figure 4.4.) When being used for this purpose, the variable thickness degrader was adjusted so that the isotopes to be identified would be fully stopped within the degrader. The electronics allowed for triggering on SeGA for purposes of calibration. The resolution of SeGA was checked prior to the isomer identification by placing a calibration "SRM" mixed gamma source near the detectors and running with the SeGA trigger. SeGA was then calibrated with a ^{56}Co source as well as with the SRM source placed in the beamline on the degrader mount.

The microsecond isomer verification was done at the ^{72}Ni setting of the A1900. Isomers of ^{70}Ni, and ^{72}Cu were used [52] (See Table 4.1). In this energy range, the betaSeGA configuration has an efficiency of 14.4% (at 100 keV) to 5.3% (at 1 MeV) (see http://www.nscl.msu.edu/tech/devices/ gammarayspectrometer/sld.pdf). The

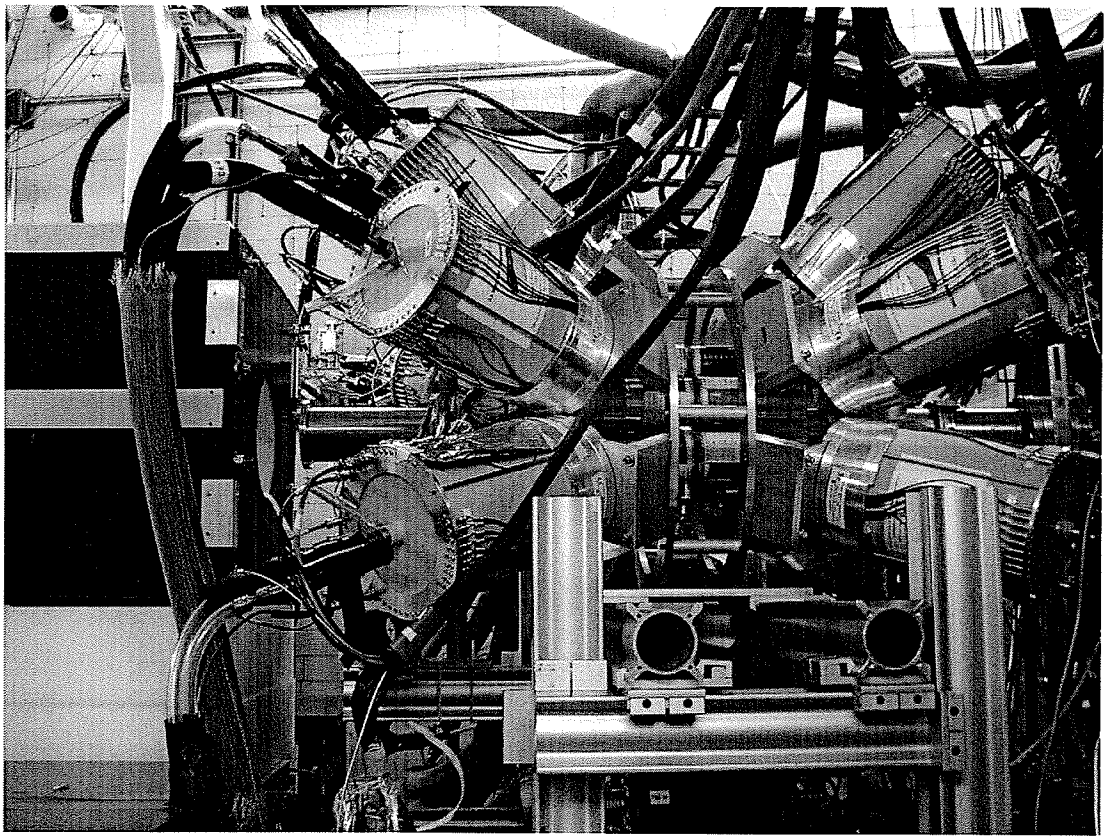

Figure 4.4: SeGA arranged in the "betaSeGA" configuration around the variable degrader, upstream from the BCS-NERO station.

Table 4.1: γ lines used to verify the particle ID.

Isotope with μsecond isomer	γ energy (keV)
^{70}Ni	183, 448, 970, 1259
^{72}Cu	138

Table 4.2: $B\rho$ setting used.

Centered Fragment	$B\rho_{12}$	$B\rho_{34}$
^{72}Ni	4.06110	3.95090
^{73}Ni	4.11870	4.00860
^{74}Ni	4.17550	4.06540
^{75}Ni	4.23150	4.12140
^{76}Ni	4.28850	4.17850
^{77}Ni	4.34300	4.23290
^{78}Ni	4.40140	4.29140

online particle identification by energy loss and time of flight in the experimental vault is shown in Figure 4.5. The isotopes ^{70}Ni and ^{72}Cu were identified by calibration with the A1900 energy-loss detector. Figures 4.6 and 4.7 show the gamma spectra gated on the isotopes ^{70}Ni and ^{72}Cu respectively as identified in the particle identificaton by calibration with the A1900. The gamma rays associated with the respective isomeric states are clearly visible, thus confirming the particle identification.

4.2.4 Scaling $B\rho$ to the ^{78}Ni setting.

Following the isomer verification of the particle identification at the ^{72}Ni setting, the fragment separator setting was stepped out to the ^{78}Ni setting using the $B\rho$ scaling technique. The settings were confirmed through the ^{75}Ni setting by scanning $B\rho$ for production rate. Table 4.2 shows the $B\rho$ values for each isotope setting.

4.2.5 Implantation

Once at the appropriate fragment setting, the variable degrader in the experimental vault was adjusted to allow the particles to pass through to the BCS-NERO station. The degrader then served to modify the secondary beam energy to achieve implan-

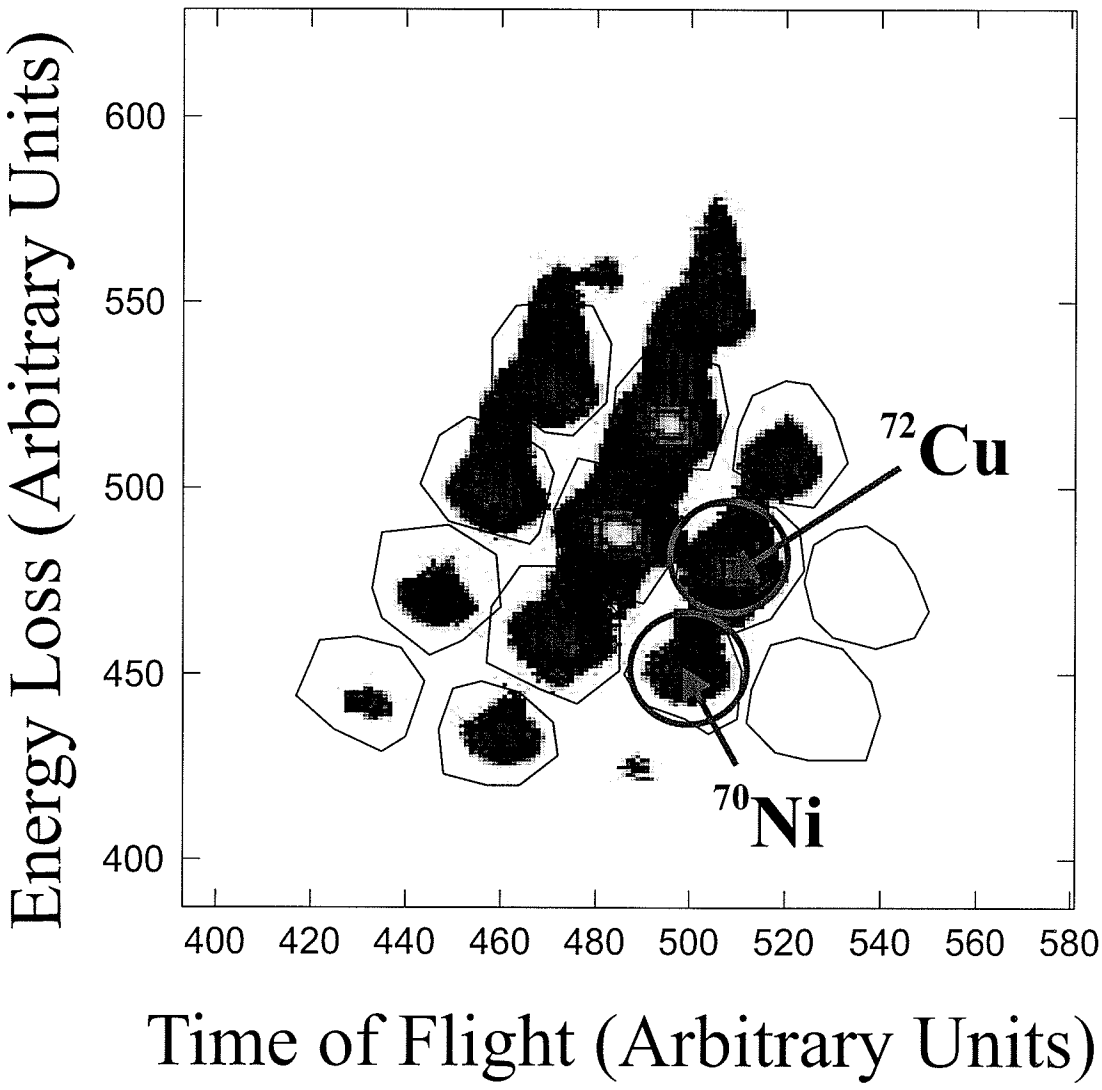

Figure 4.5: Online particle identification by ΔE-TOF using the experimental vault energy-loss detector.

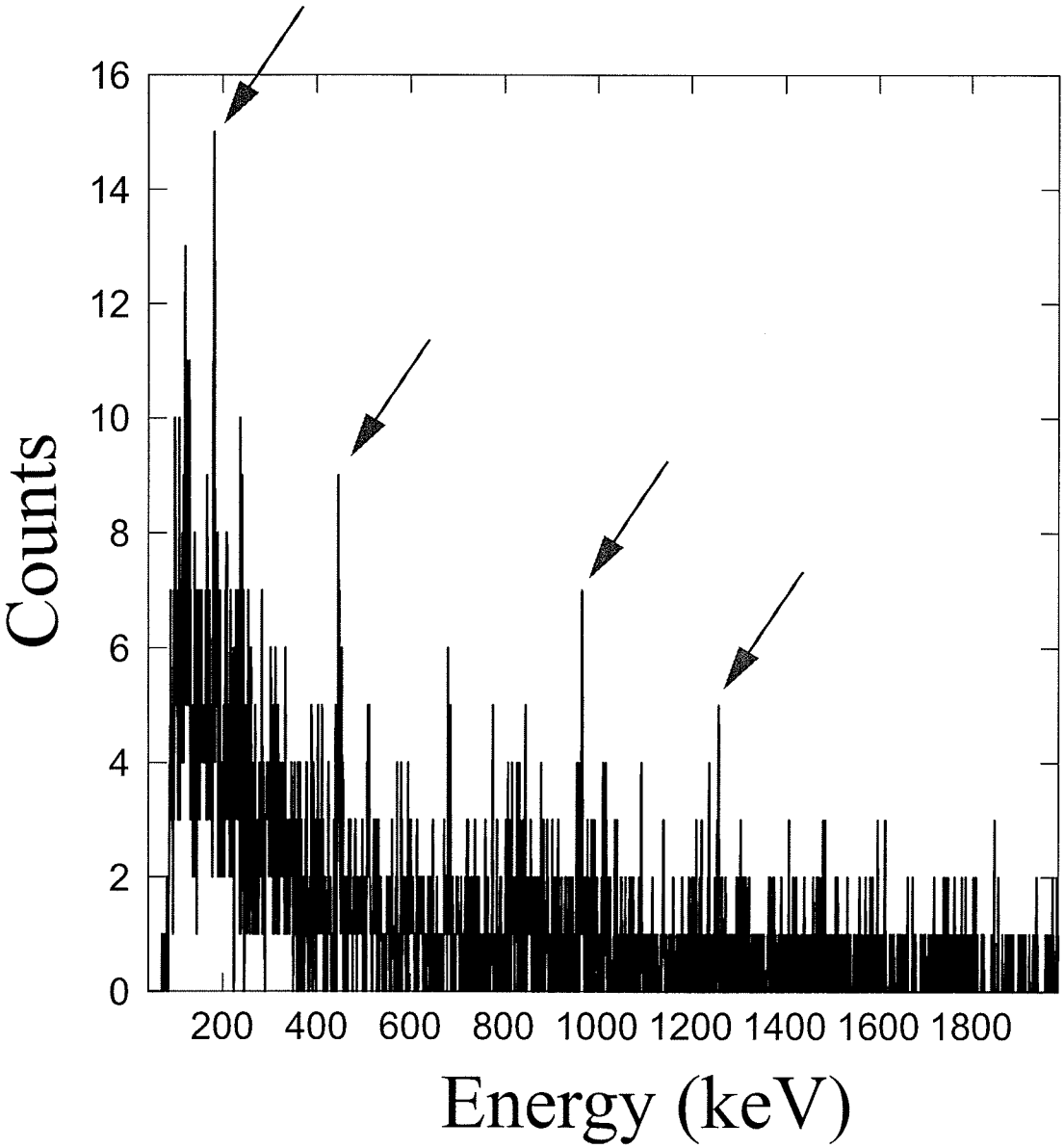

Figure 4.6: Gamma spectrum from ^{70}Ni PID gate showing the 183, 448, 970, and 1259 keV gammas associated with ^{70m}Ni.

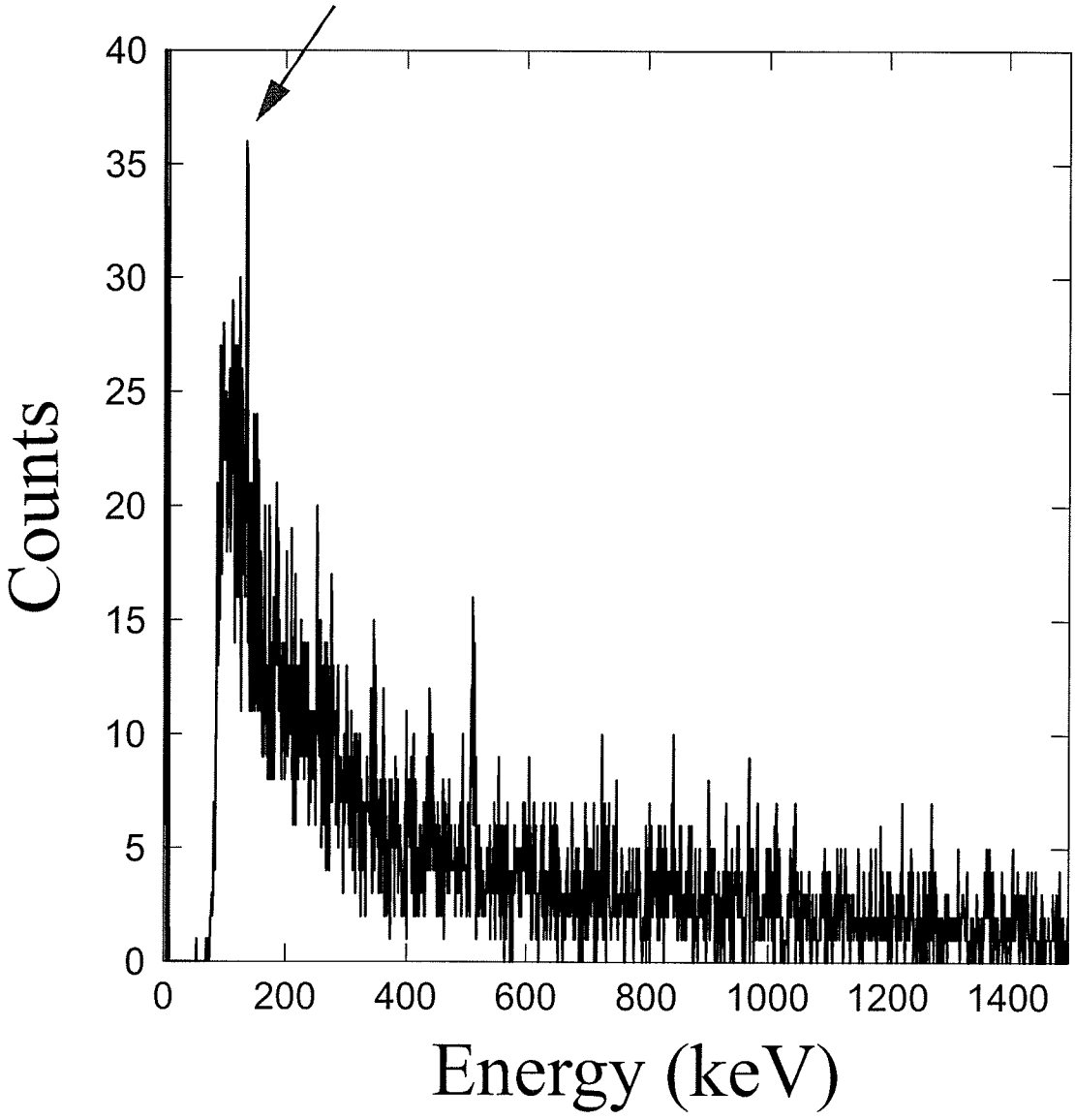

Figure 4.7: Gamma spectrum from ^{72}Cu PID gate showing the 138 keV gamma associated with ^{72m}Cu.

tation in the implantation detectors. Coarse thickness adjustments were made by adding thin pieces of Al in a stack. The degrader was mounted on a rod that could be rotated manually from a handle external to the beamline, so that fine adjustments to the thickness could be made without requiring to break the vacuum of the line. After the degrader, the beam encountered another Si detector, refered to as Pin2, for a second energy-loss measurement, and finally passed through a third Si detector, refered to as Pin2a, which was part of the Beta Counting System described in the next section, before finally implanting in the Double-Sided Silicon-strip Detector (DSSD) of the Beta Counting System. (See Figure 4.9).

4.2.6 Beta Counting System

The Beta Counting System (BCS) [53] consists of a 985 μm double-sided segmented Si detector in which the beam was implanted. On one side the forty 1mm wide segments run horizontally, and on the other side forty vertically, resulting in a pixelation of 1600 pixels in a 4 cm x 4 cm area, giving the location of implantation. The beam was continuously implanted into the DSSD, which registered the time and position of each ion. The typical total implantation rate for the entire detector was under 0.1 per second.

Using the dual-gain capabilities of the BCS electronics, the DSSD also registered the time and position of any β-decays following the implantation of a nucleus. This allowed the correlation of a decay event with a previously identified implanted nucleus. Additional Si detectors in front and behind the DSSD were used to veto events from light particles in the secondary beam that can be similar to β-decay events. With this setup, along with appropriate veto gates, the total β-type event background rate associated with an implanted ion was typically less than 3×10^{-2}/s. From the time differences between implants and a correlated decays, a decay curve could be built and half-lives could be deduced. The Si detectors of the BCS were calibrated before and after the experiment with a ^{90}Sr β-source and a ^{228}Th α-source.

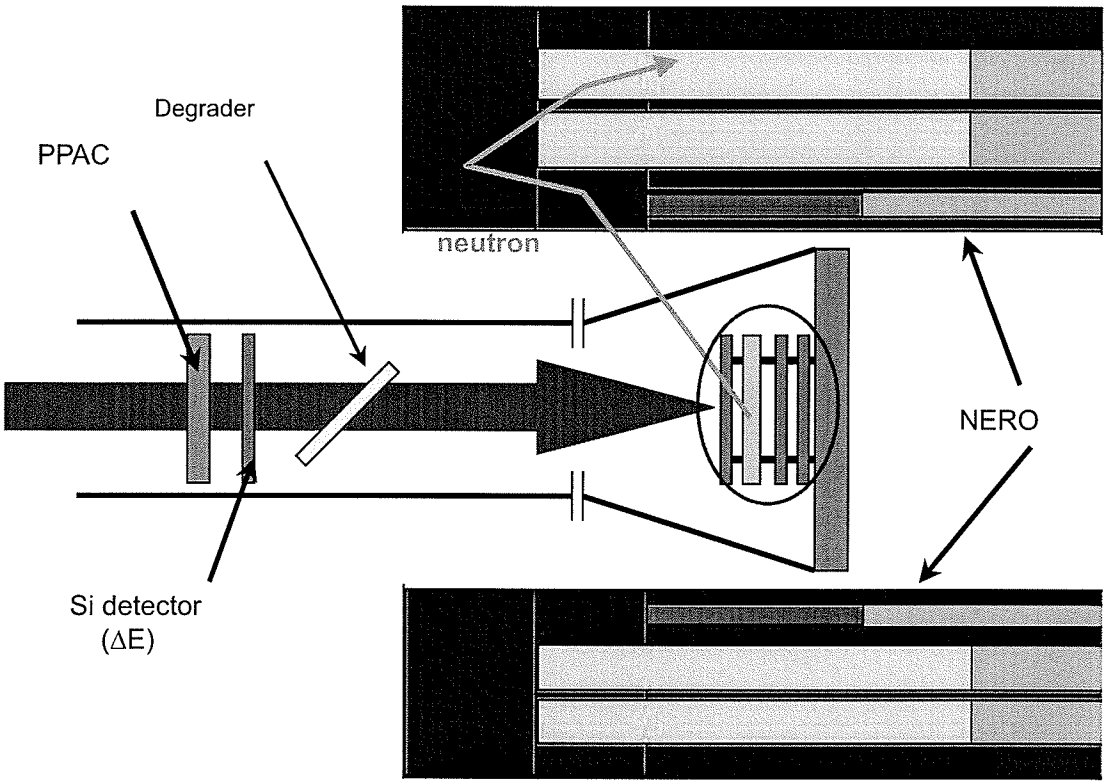

Figure 4.8: Schematic of beta endstation inside NERO.

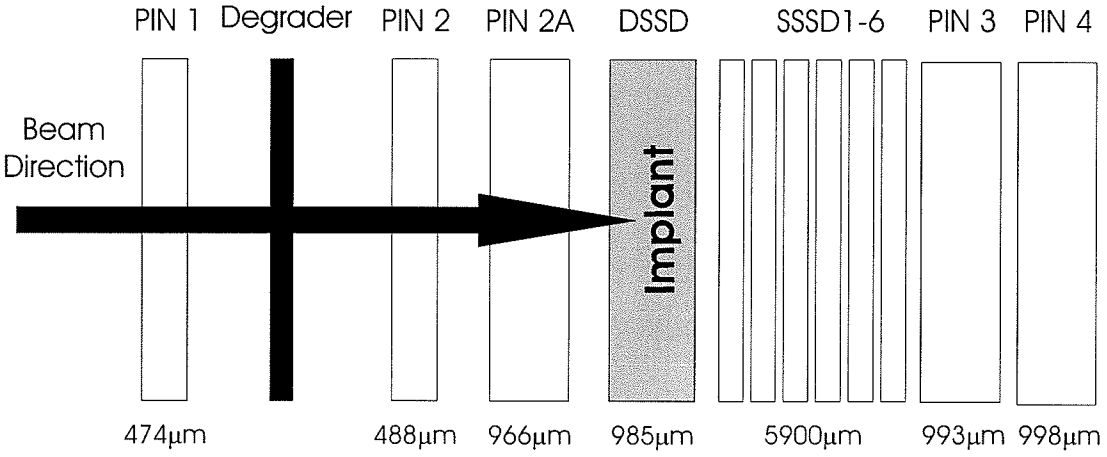

Figure 4.9: Beamline detector setup in the experimental vault.

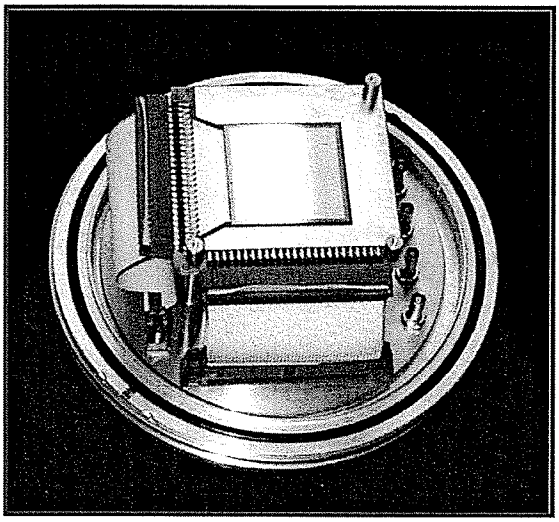

Figure 4.10: The DSSD.

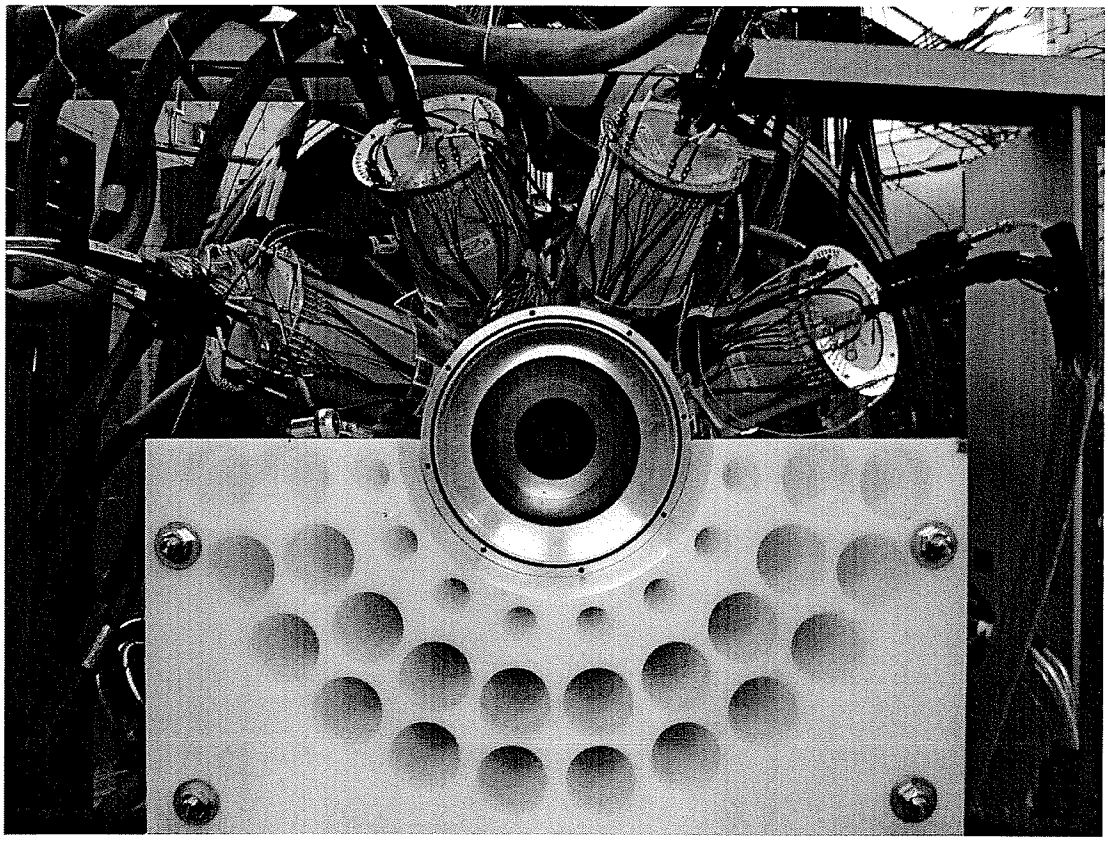

Figure 4.11: The DSSD case inside the bottom half of NERO. SEGA detectors in the background. View is looking up the beam axis.

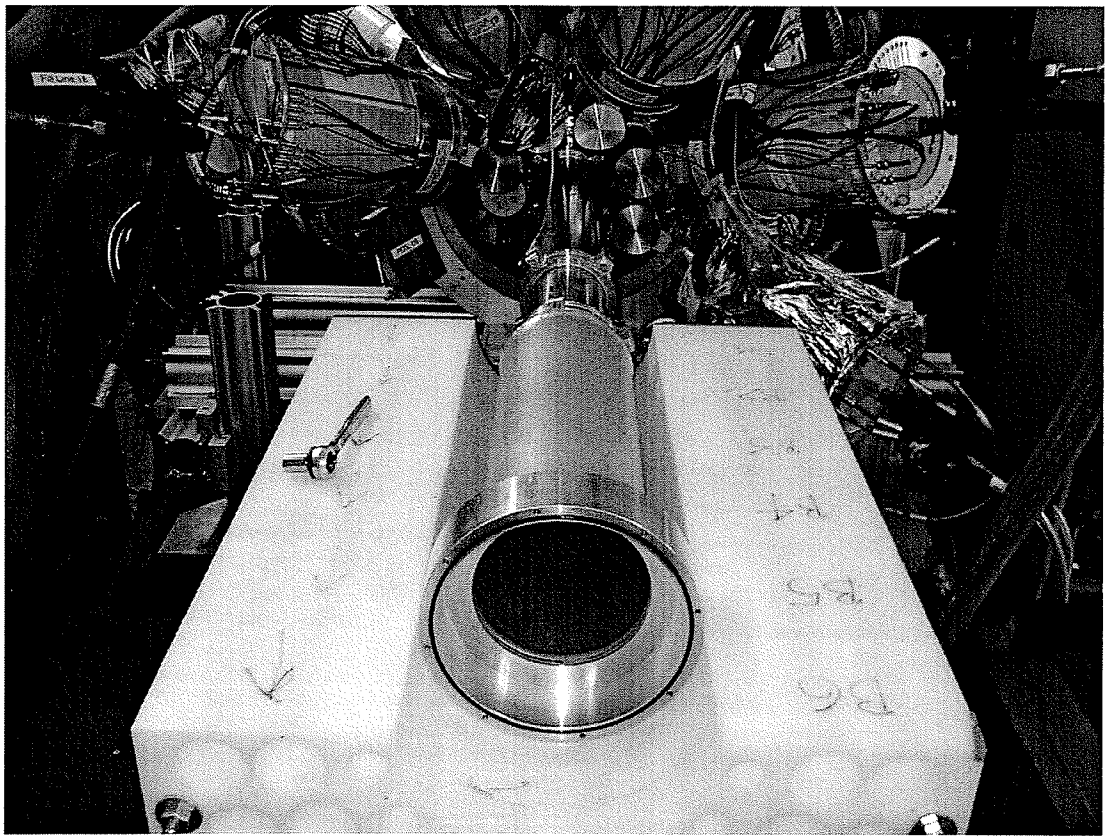

Figure 4.12: View of the experimental vault, looking up the beamline. SeGA is in the background. In the foreground is the BCS leading into the bottom half of NERO.

4.2.7 NERO

NERO was arranged around the BCS so that the DSSD of the BCS was at the target position of NERO. If the *beta*-decay resulted in the emission of a neutron, the neutron could pass into NERO, where it would be moderated and detected in the proportional tubes. The electronics of the BCS were fed out the down-beam end of the NERO beamline hole.

NERO was triggered on any event in the DSSD high-gain side. When a high-gain (decay) event occured, the NERO gate was openned for 200 μs. The energy from the proportional counters was recorded. In addition, the time of the neutron event was recorded by a V767 VME TDC which was added to the NERO electronics for this experiment. The TDC could record multiple neutron events occuring within the 200 μs neutron gate.

4.2.8 Electronics

Figure 4.13 shows a diagram of the electronics for the experiment. The DSSD provided the master trigger; however, alternate master triggers were available for other detectors, such as NERO and SEGA in case they were needed. The master trigger was any implant or decay event. The master live trigger was the AND of the master trigger and the computer NOT busy according to standard trigger configuration. The master trigger opened the neutron gate for the NERO electronics with a gate in latch mode for 200 μs.

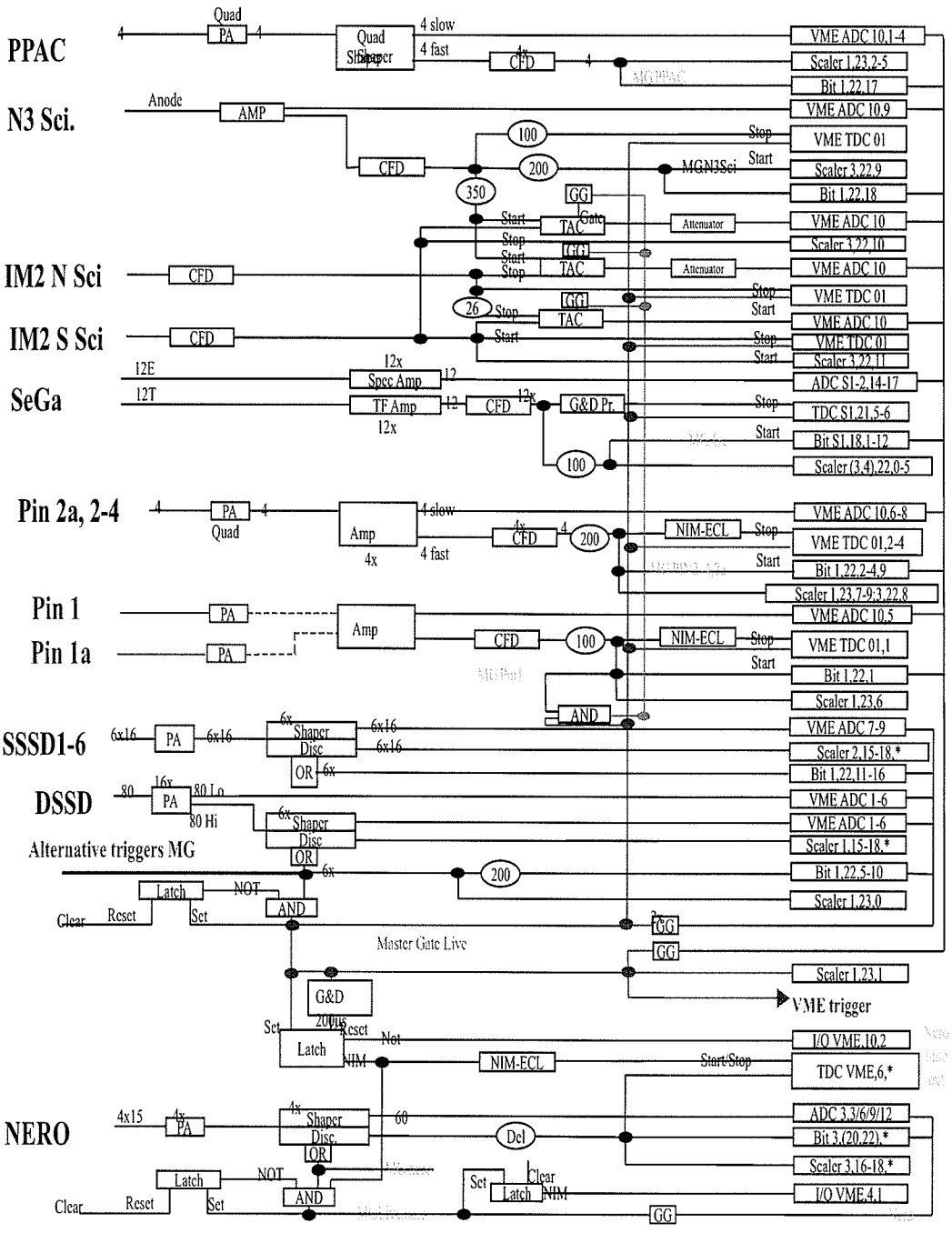

Figure 4.13: Electronics diagram for NSCL Experiment 02028.

Chapter 5

Analysis

5.1 Particle Identificaton

As stated in the Experimental Chapter, the isotopes were identified in-flight by energy-loss, time-of-flight and momentum measurements. The energy loss, when velocity corrected using the time-of-flight measurements, gives elemental seperation. For a given element, a time-of-flight measurement, when momentum corrected, gives isotopic seperation.

5.1.1 Energy Loss

The energy loss was measured in two Si detectors located in the experimental vault and seperated by a passive Al degrader. The energy loss of a projectile in a material is proportional to the square of the nuclear charge of the projectile and inversely propertional to the square of the velocity. The relationship is given by the Bethe formula [30]:

$$-\frac{dE}{dx} = \frac{4\pi e^4 Z^2}{m_o v^2 A} N_A \rho B(v) \tag{5.1}$$

which in terms of Z is:

$$Z = \sqrt{-\frac{dE}{dx}\frac{m_o v^2 A}{4\pi e^4 N_A \rho B(v)}} \tag{5.2}$$

where

$$B = z[ln\frac{2m_o v^2}{I} - ln(1 - \frac{v^2}{c^2}) - \frac{v^2}{c^2}] \tag{5.3}$$

v and Z are the velocity and atomic number of the projectile, ρ, A and z are the mass density, atomic weight, and atomic number of the absorber, in this case Si. m_o and e are electron mass and charge. N_A is Avagadro's number. I is the average excitation and ionization of the absorber. For a given velocity then, the energy loss uniquely defines the atomic number, or element, of a particle.

Time-of-flight Correction to Energy Loss

The projectiles in the experiment arrive at the energy loss detectors with a velocity distribution. To distinguish them, it is necessary to remove the velocity dependence. One can remove this dependence by measuring the time of flight of each particle. The velocity is given simply by:

$$v = \frac{D}{t} \tag{5.4}$$

Since the distance D, a particle's path length through the beamline, is essentially the same for all particles, a measure of the time of flight is a measure of the velocity, and the energy loss can be corrected using time of flight. The energy loss vs time of flight with the energy loss uncorrected is shown in Figure 5.1. The same plot with energy loss corrected is shown in Figure 5.2. The values used for this correction can be found in Table 5.1.

In this experiment, two energy-loss detectors were used. The full Bethe energy-loss correction was performed only on the first energy-loss detector, and confirms the elemental identification. However, for the analysis, a simple linear correction as a function of time-of-flight was performed for both energy-loss detectors and used for the remainder of the analysis. The general equation used was:

$$dE_{CORRECTED} = dE_{RAW} - [(M \times TOF) + B] + Y \tag{5.5}$$

Table 5.1: Values Used in Bethe Energy Loss Correction

$4\ \pi\ e^4\ N_A\ /\ m_o$	0.30707 MeV cm^2 / mole
m_o	0.511003 MeV/c^2
c	2.9979×10^8 m/s
A	28.086 g/mole
Z	14
ρ	2.3212 g/cm^3
I	0.000173 MeV
L	37.3 m
dx	0.0474 cm

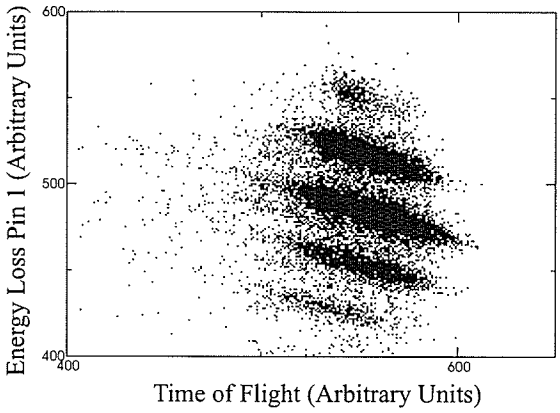

Figure 5.1: Uncorrected energy loss vs. time of flight.

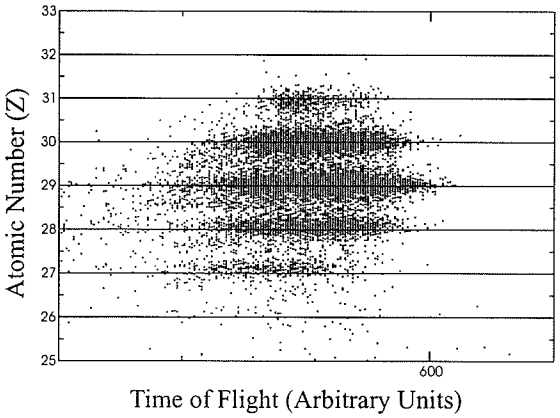

Figure 5.2: Bethe corrected energy loss vs. time of flight.

Table 5.2: Correction Factors for Linear Energy-loss Correction

	Pin1	Pin2
M	-0.3682	-1.4125
B	686.93	1575.2
Y	480	480

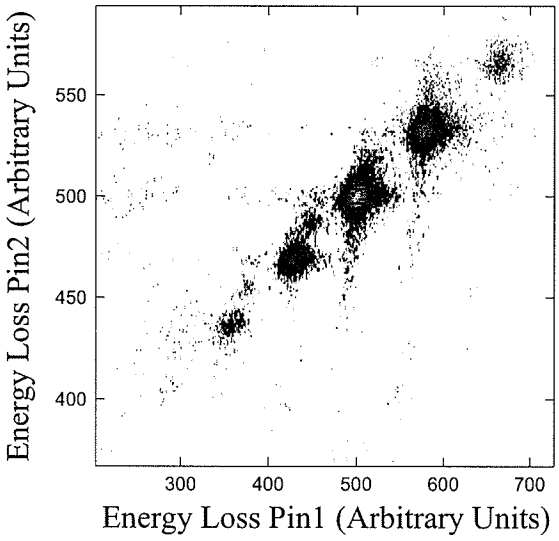

Figure 5.3: Element identification using energy loss in Pin1 vs. Pin2.

where M is the slope, B is the intercept, and Y is another arbitrary offset used for convenience. The values used for the correction as shown in Figure 5.3 can be found in Table 5.2.

5.1.2 Time of Flight

In order to separate individual isotopes from the element distributions, one requires essentially a measurement of the mass of the particle. A time-of-flight measurement affords such a mass measurement because the time of flight of the projectile is proportional to the mass of the projectile. In the non-relativistic limit,

$$t = \frac{D}{v} = \frac{D}{\frac{p}{m}} = \frac{mD}{p} \tag{5.6}$$

In the experiment, the momentum p is not directly measured but the magnet settings and slits of the fragment separator define a $B\rho = \frac{p}{q}$, so that

$$t = \frac{mD}{B\rho q} \tag{5.7}$$

For a time of flight gated on an element using the two energy losses as described in Section5.1.1 (thereby specifying a q), the time of flight uniquely defines a mass.

5.1.3 Momentum Correction to Time of Flight

However, the particles actually have a distribution in $B\rho$ due to the 5% momentum acceptance of the A1900. Therefore, to distinguish masses, it is still necessary to corrrect for the $B\rho$ distribution. This correction to the time of flight was assumed to be linear. That this assumption is valid is demonstrated by the following.

The measured position in the intermediate image is proportional to $B\rho = \frac{p}{q}$, or for a given particle with charge q, proportional to the momentum p (the following assumes non-relativistic limit):

$$x \propto \Delta p \tag{5.8}$$

$$x = G\Delta p \tag{5.9}$$

$$x = G(p_o - p) \tag{5.10}$$

$$x = Gp_o - Gmv \tag{5.11}$$

so that

$$v = \frac{Gp_o - x}{mG} \tag{5.12}$$

since

$$v = \frac{D}{t} \tag{5.13}$$

$$t = \frac{mGD}{Gp_o - x} = mGD[\frac{1}{Gp_o - x}] = mGD[1 - \frac{x}{Gp_o} + ...] \tag{5.14}$$

so

$$t = mGD - \frac{D}{v_o}x + ... = Mx + B + ... \tag{5.15}$$

taking the first two terms demonstates the linear correction to the time of flight to first order.

Therefore, in a plot of momentum-corrected time of flight vs. intermediate image position, the isotopes of a given element appear as seperated horizontal lines.

In summary, the elements were selected by a gate in the time-of-flight corrected two-dimensional energy-loss plot. These element gates were then applied to a position-corrected time-of-flight vs. momentum plot, where the isotopes were then identified. In addition, reasonable cuts to exclude events at large A1900 intermediate image (IM2) positions were made. A particle identification plot is shown in Figure 5.5 to give an idea of the relative statistics. However, this plot was not directly used for isotope identification, as described above. Based on the identification, a total of 11 ^{78}Ni were identified.

5.1.4 Possible Contaminants

As can be seen in the Pin1 Energy Loss vs. Pin2 Energy Loss (Figure 5.6), there are some particles in the identification which do not lie within an elemental distribution. These particles were gated on and analysed in the same manner as the identified particles. Their half-lives were determined and compared to the identified elements, and the results are most consistant with with the hypothesis that these are not charge states, but particles which encountered an additional energy loss consistant with a piece of material of thickness $525 \pm 25\mu$m Al equivalent in the beamline. In order to achieve the corresponding lengthening flight time that would be consistant with their measured time of flight, this material would have to be located somewhere after the focal plane of the A1900 but before the experimental vault. A study of the beamline does not indicate that there should have been any known material in this section

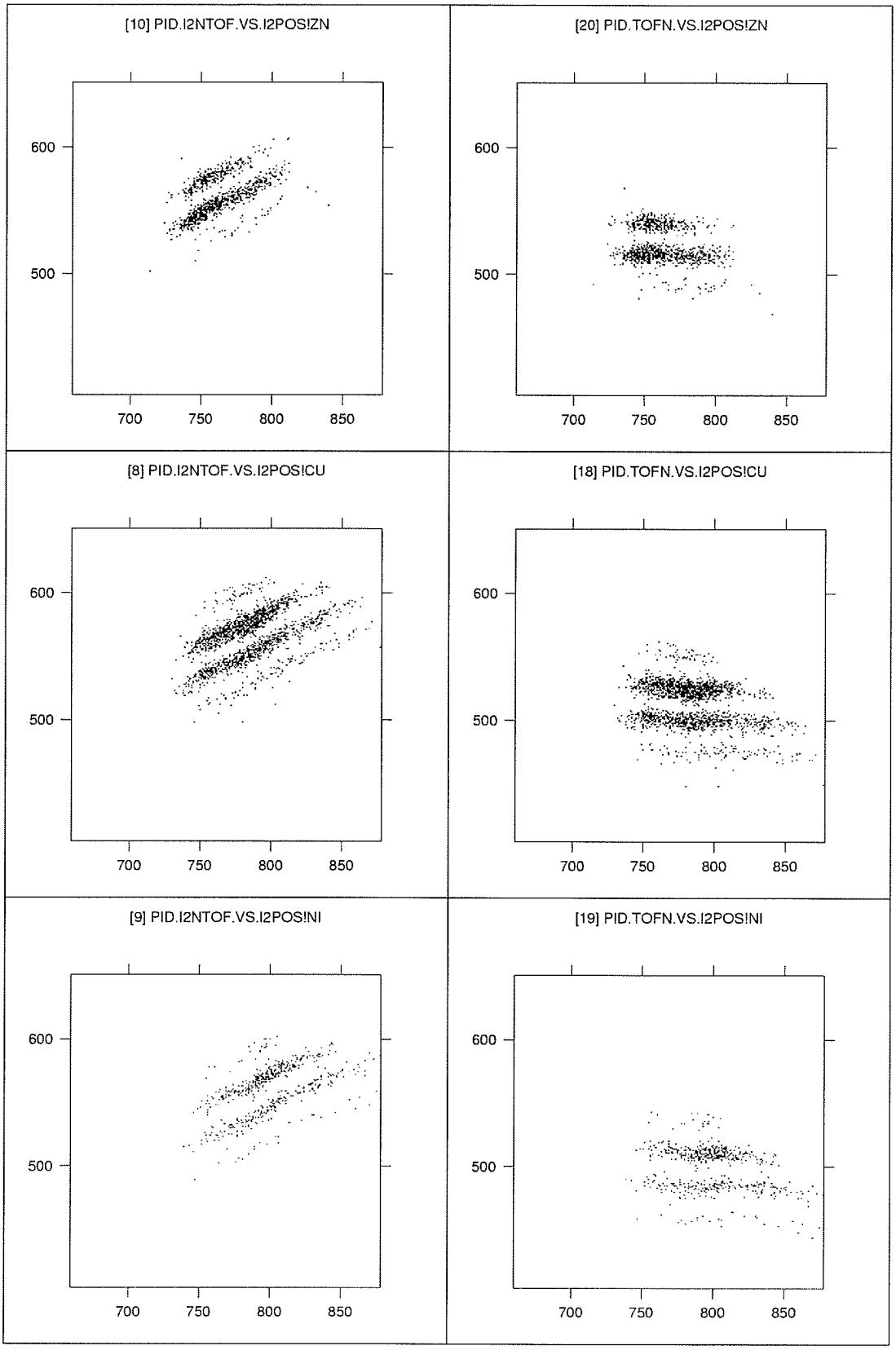

Figure 5.4: Time of flight vs. intermediate image position for Zn, Cu, and Ni isotopes. The first column is uncorrected. The second column is momentum corrected.

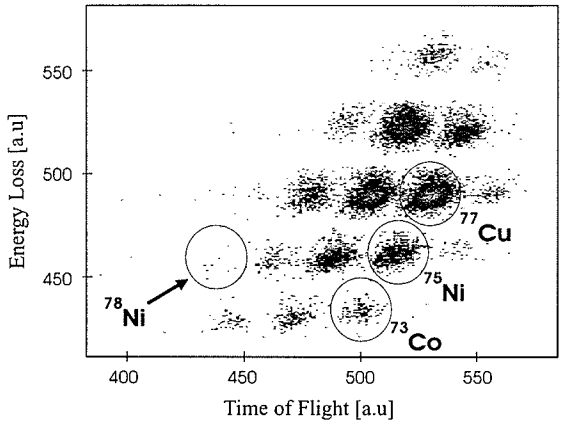

Figure 5.5: Energy loss vs. Time of flight for a portion of the data.

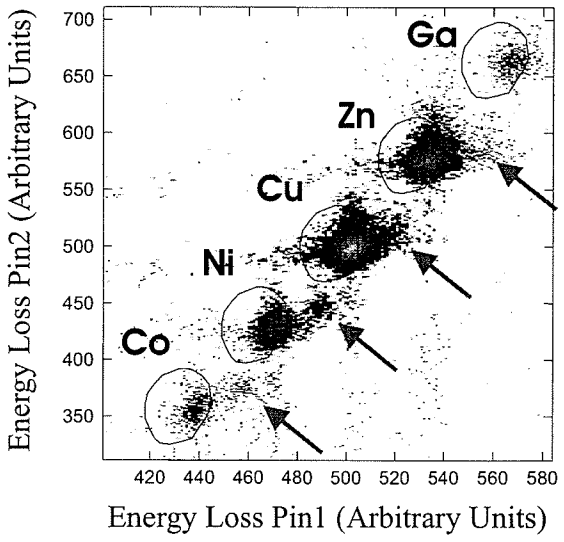

Figure 5.6: Energy Loss in Pin1 vs Pin2 showing the conservative element gates. The arrows indicate the unidentified particle distributions

of the beamline during the experiment. In addition, these particles do not exibit any abnormal position distribution or angle distribution, as one would expect for particles that might encounter different thicknesses of material along the beamline. Therefore the origin of these particles is still unclear. The element gates were therefore drawn conservatively in such a way as to avoid possible contamination from these particles (see Figures 5.6 and 5.7).

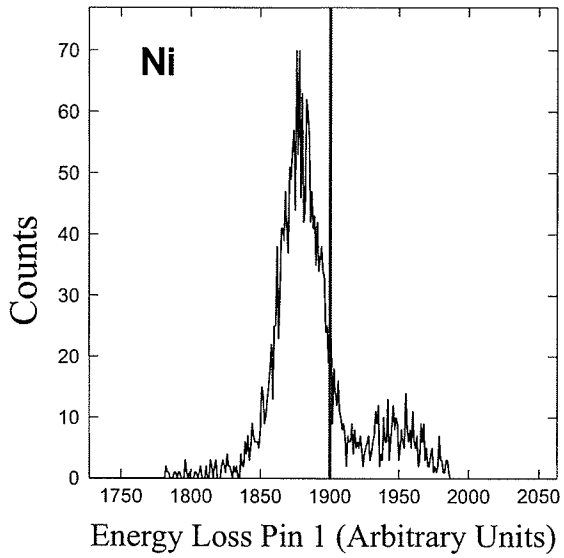

Figure 5.7: Energy Loss in Pin1 showing the Ni distribution on the left and the unidentified particle distribution on the right. The line indicates the position of the Ni element gate.

5.2 Production Cross-section

With a particle identification, one can calculate a production cross-section. The production cross-section of ^{78}Ni is of particular interest. It has been calculated and tested at several laboratories and serves as a marker for the capabilities of next generation accelerators.

The production cross section was calculated based on the equation:

$$\sigma = \frac{R_b}{I_a N} \tag{5.16}$$

where N is the number of target nuclei shown to the beam per unit area, I_a is the incident beam rate, and R_b is the rate of outgoing particles. The rate of outgoing particles of ^{78}Ni was 11 over a beam time of about 104 hours. Our target was 376 mg/cm^2 Be. Using the atomic mass of Be, and Avagodro,s number, we convert this to target nuclei per unit area. BaF_2 detectors were placed at the production target

to measure the incident beam rate, I_a. However, the voltage was set so that the rate resulted in overflow in the detectors, so that the BaF_2 detectors were not helpful. Fortunately, the beam current was also measured with a Faraday cup before and/or after most runs. The current during a run was taken to be the average of the current before and after the run. For runs for which no current measurement was taken, the current was taken to be the average of the run before and after. The uncertainty in the Faraday cup measurement is known to be on the order of a few enA.

The final factor in the cross section is the transmission of the beam from the production location before the A1900 to the detection location in the experimental vault. The transmission was studied using the code MOCADI [54] as well as through several measurements.

The transmission through the A1900 depends on the angular and momentum acceptance. The angular acceptance was calculated to be 80-90 % so a value of 85 $\pm$ 5 % was adopted. The reduction in efficiency due to limited momentum acceptance depends on the momentum distribution of the beam, and the results of calculations based on some of these distributions range from 90 to 100 %. A value of 95 $\pm$ 5 % was adopted.

The transmission to the N3 vault was measured for several isotopes on different $B\rho$ settings. For ^{72}Ni, the FP-N3 transission was measured with the aid of BaF_2 detectors to be 84 $\pm$ 12 %. It must be assumed that the transmission of ^{78}Ni on the ^{78}Ni setting does not deviate within 12 % of the ^{72}Ni setting.

Combining these contributions based on both measurement and simulation, the adopted value for transmission was 65 $\pm$ 13 %.

The resulting cross section for the production of ^{78}Ni was 0.02(1) pb, much smaller than the value calculated by EPAX [55] of about 4 pb. The largest uncertainty comes from the statistical uncertainty due to the extremely low ^{78}Ni count. The uncertainty in the transmission is the next largest contribution to the total error budget.

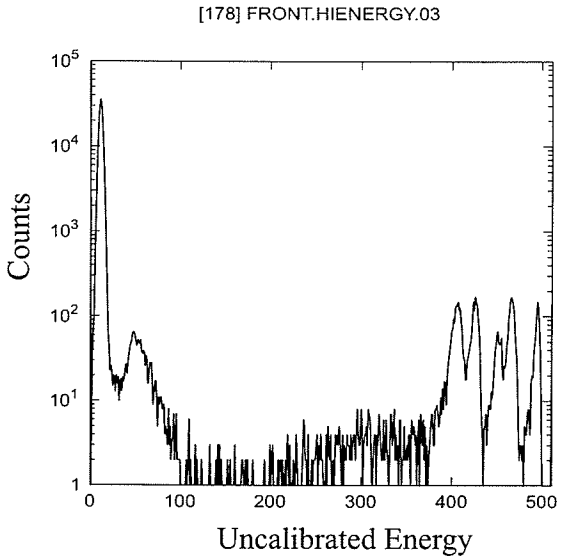

Figure 5.8: ^{228}Th calibration source spectrum in a typical DSSD high-gain channel.

5.3 Gain-matching

The high gain of the DSSD strips were gain-matched before and after the experiment using the alpha source ^{228}Th, which displays several peaks of known energy. The source was placed in front of the DSSD. See Figure 5.8. The low gains were not gain-matched. The SSSDs were gain-matched in the same way as the high-gain DSSD.

5.4 Thresholds

The high-gain thresholds for the DSSD were set using the β emitter ^{90}Sr. A typical threshold setting is shown in Figure 5.9

Upper level thresholds were not used. The SSSD thresholds were set as with the high-gain DSSD.

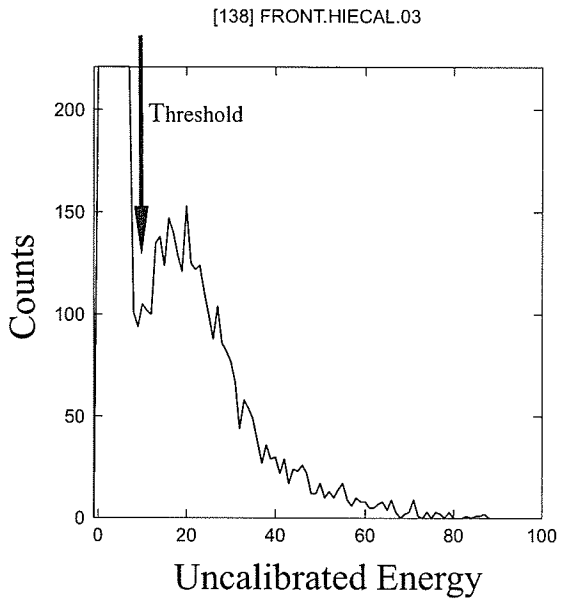

Figure 5.9: ^{90}Sr calibration source spectrum for setting threshold in a typical DSSD high-gain channel.

5.5 Absolute Calibration of DSSD

An absolute calibration of the high-gain DSSD energy was done. Though it was not necessary for the analysis of the present experiment, it is useful for the purpose of comparing the threshold settings to other experiments which make use of the DSSD. The calibration was based on the energy of the peaks in the ^{228}Th α spectrum. The settings can be found in Figures 5.10 and 5.11.

5.6 Correlations

An implant event in the DSSD was essentially defined as a low-gain (high-energy) signal. The actual implant criteria are in Table 5.3. The position of the implant was taken to be the pixel in which the maximum energy was deposited. A decay event was essentially defined as a high-gain event which did not also trigger the other Si detectors in a specific way so as to be vetoed as a punch-through or other type of event.

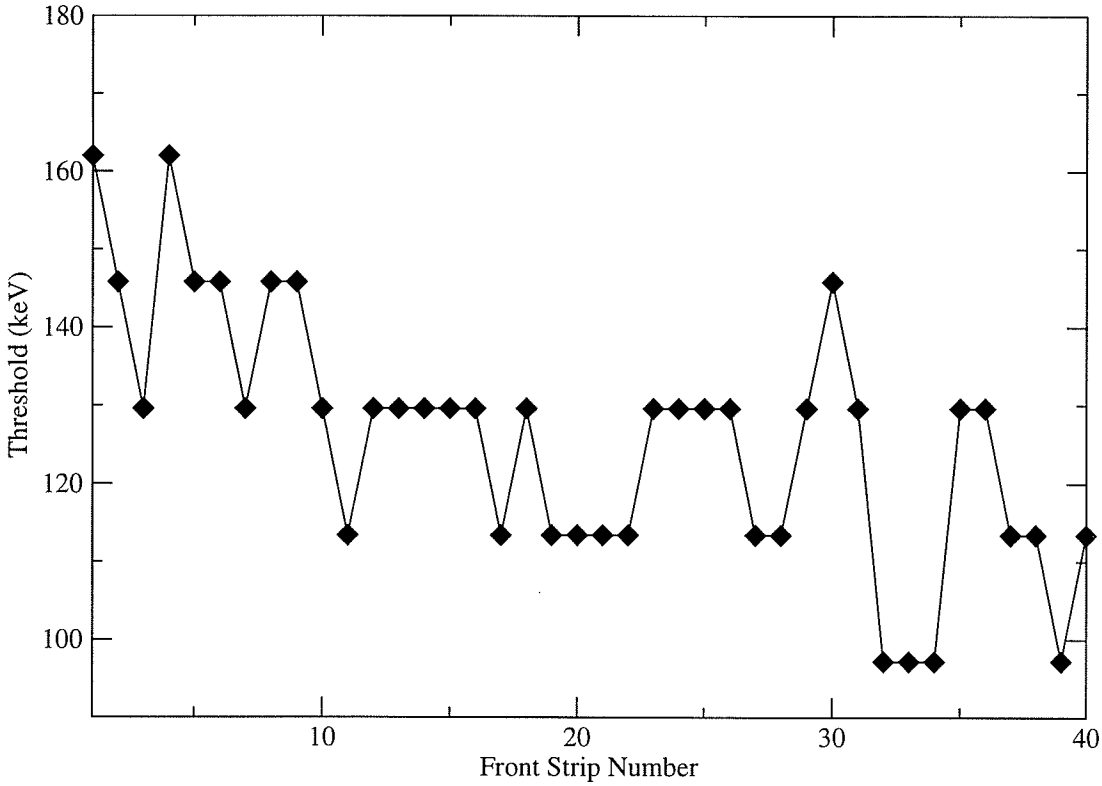

Figure 5.10: Threshold settings for DSSD front high-gain strips.

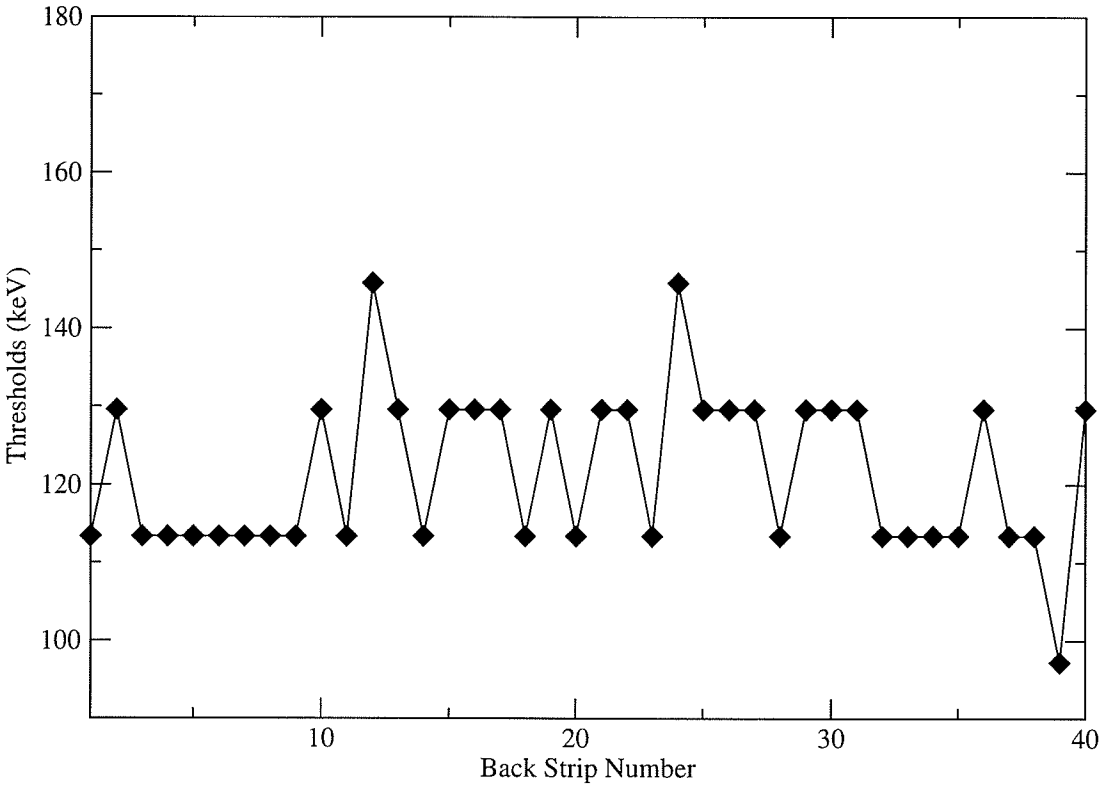

Figure 5.11: Threshold settings for DSSD back high-gain strips.

Table 5.3: Implant Criteria

Required logical AND of the following
Hit Pin1
Hit DSSD Front
Hit DSSD Back
NOT Hit SSSD1

Table 5.4: Decay Criteria

Required logical AND of the following
NOT Hit Pin1
NOT Hit Pin2
DSSD Front High Gain Signal
DSSD Back High Gain Signal
NOT a Punch Through
Hit SSSD1 OR SSSD2 OR Pin3 OR Pin4

If a decay event fired more than one strip, the position of a decay was taken to be the strip with maximum energy deposited. A decay was correlated to an implant if the position of the decay was at the pixel of an implant or within one pixel away. If the decay event fired more than one strip, the maximum strip was required to be within one pixel away. The decay also had to come within a specified correlation time window, which is chosen based on the expected lifetime of the isotopes being studied. Up to three decays could be correlated to a given implant.

For each decay correlated to an implant, the time difference between implant and decay was found by simply comparing the times of the two events. This produces a list of decay times associated with a previously identified isotope, each implant having a decay chain of up to three decays associated with it. Of the 11 ^{78}Ni events identified, 8 had at least one decay associated with it. Table 5.5 shows the 8 decay chains associated with^{78}Ni.

Table 5.5: Decay Chains for ^{78}Ni

Chain	Decay Time 1 (s)	Decay Time 2 (s)	Decay Time 3 (s)
1	0.328	3.322	0
2	0.749	0	0
3	0.120	1.740	2.280
4	0.884	1.555	0
5	0.031	0	0
6	0.391	0	0
7	0.049	0	0
8	0.804	0	0

5.7 Curve Fitting

For the isotopes with high statistics, it was possible to bin the decay times to form a decay curve. This is a common analysis of decay data in the case of high statistics. For this method to be valid, the minimum number of counts in a bin must be around 5 (see Ref. [56], p266). This was done for the isotopes of highest statistics. The decay times were binned and fit to a curve which included terms for parent, daughter, granddaughter, and background contributions. The equations used are known as the Bateman equations (Ref. [42]):

$$A_n = N_o \sum_{i=1}^{n} c_i e^{-\lambda_i t} \tag{5.17}$$

where A_n is the activity of the nth member of the decay chain, N_o is the initial number of parent nuclei, λ_i is the decay constant of the ith member of the decay chain, and the coefficients are:

$$c_m = \frac{\prod_{i=1}^{n} \lambda_i}{\prod_{i=1}^{n}{}' (\lambda_i - \lambda_m)} \tag{5.18}$$

where $\prod'$ indicates for all $i \neq m$. In this case, three generations (parent, daughter, granddaughter) were assumed.

The free parameters were the scaling factor and the parent decay constant. Re-

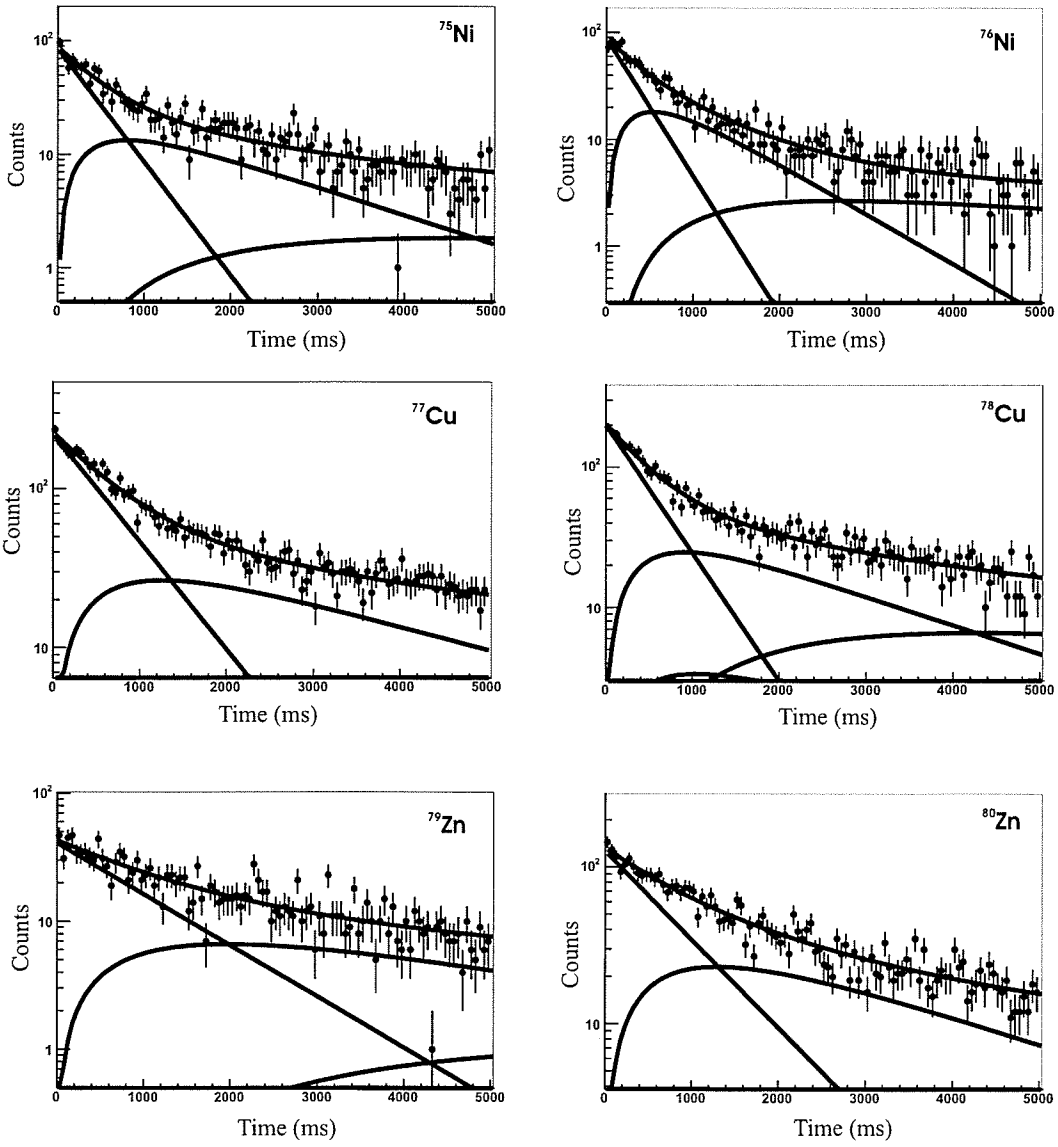

Figure 5.12: Decay-curve fits for the high-statistics cases of $^{75\text{-}76}$Ni, $^{77\text{-}78}$Cu and $^{78\text{-}79}$Zn. The linear background is not shown.

quired known inputs were daughter and granddaughter half-lives. The background was assumed to be constant as a function of time and was allowed to vary as a parameter in the fitting

5.7.1 β-detection Efficiency from Curve Fits

Using the curve fits, the DSSD efficiency for detection of decays was determined in the following way. The number of implants is known simply from counting implant events in the DSSD. The fit for that isotope is then used to identify the number of parent decays detected. The efficiency is the number of parent decays detected divided by the number of parent implants observed:

$$\epsilon_\beta = 100 \times \frac{N_D^{parent}}{N_I} \tag{5.19}$$

where N_I is the number of implants and N_D^{parent} is the number of parent decays, calculated from the fit parameters $(A_o)_{fit}$ and λ_{fit}, the fitted decay constant of the parent:

$$N_D^{parent} = \frac{(A_o)_{fit}}{\lambda_{fit}} \tag{5.20}$$

The efficiencies derived in this way are shown in Figure 5.13. For ^{75}Ni, ^{76}Ni,^{77}Cu and ^{78}Cu the statistics were sufficient to determine the β-detection efficiency by comparing fitted decay curves with the total number of implanted species of that isotope. The resulting efficiencies agree very well and range from 40% to 43% with no systematic trends in the deviation. (see Table 5.6).

5.8 A Method of Maxiumum Likelihood

In the case of low statistics, it is not possible to bin the data and then analyze a decay curve by the method of curve fitting. However a method does exist that is correct even in the case of low statistics. This method has been used previously to extract

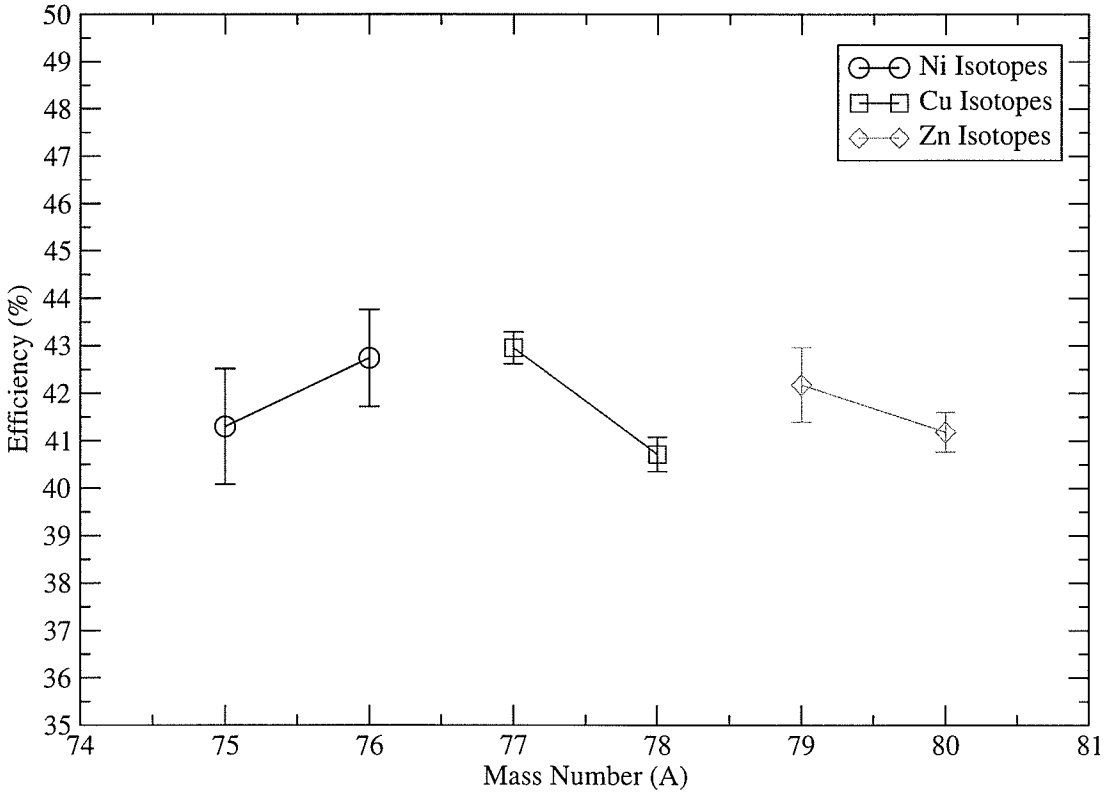

Figure 5.13: Beta detection efficiency based on fitting of decay curves for isotopes with more than 500 implants.

Table 5.6: β-detection Efficiencies for High-Statistics Cases

Isotope	Efficiency (%)
^{75}Ni	41.3 ± 1.2
^{76}Ni	42.7 ± 1
^{77}Cu	42.95 ± 0.34
^{78}Cu	40.71 ± 0.36
^{79}Cu	41.2 ± 1.1
^{79}Zn	42.2 ± 0.8
^{80}Zn	41.2 ± 0.4

beta-decay half-lives, even with as low as 6 or 7 events [57–59].

The method, which will be refered to as Maximum Likelihood Method (MLH), is the basis of most common fitting analysis etc, even the curve fitting described above. However, the analysis used here might be described as more of a direct MLH method, in that it avoids the necessity of binning the data and thereby losing time information as well as sequential decay-chain information. This direct method will be referred to in the following simply as the MLH method, although it should be remembered that the idea of maximum likelihood is common in error analysis and fitting.

5.8.1 Probability Density Functions

The method finds the decay constant that maximizes a likelihood function, which is the product of probability densities for three decay generations as well as background events, to produce the measured time sequence of decay-type events following the implantation of a beam particle. The calculation requires knowledge of the β-detection efficiency, background rate, daughter and granddaughter half-lives, including those reached by β-delayed neutron emission, and branchings for β-delayed neutron emission (P_n) for all relevant nuclei in the decay chain.

The probability functions from which the likelihood function is constructed represent the probabilities for a given number of decay events to occur and be observed at specific times t. (The following description is based on Ref [60]).

The probability density function for one decay governed by a decay constant λ_1

to occur at the exact time t is:

$$f_1(\lambda_1, t) = \lambda_1 e^{-\lambda_1 t} \tag{5.21}$$

The probability for a decay to occur *within* a time t is:

$$F_1 = \int_0^t f_1(\lambda_1, t')dt' = 1 - e^{-\lambda_1 t} \tag{5.22}$$

The probability density function for a daughter with decay constant λ_2, which was populated by a mother with decay constant λ_1, to decay at exactly time t is:

$$f_2(\lambda_1, \lambda_2, t) = \frac{\lambda_1 \lambda_2}{\lambda_2 - \lambda_1}(e^{-\lambda_1 t} - e^{-\lambda_2 t}) \tag{5.23}$$

The probability for a decay *within* a time t of a daughter with decay constant λ_2 populated by a mother with decay constant λ_1 is:

$$F_2(\lambda_1, \lambda_2, t) = 1 - \frac{\lambda_1 \lambda_2}{\lambda_2 - \lambda_1}(\frac{1}{\lambda_1}e^{-\lambda_1 t} - \frac{1}{\lambda_2}e^{-\lambda_2 t}) \tag{5.24}$$

The probability function for the granddauther decay with decay constant λ_3 is:

$$f_3(\lambda_1, \lambda_2, \lambda_3, t) = \frac{\lambda_1 \lambda_2 \lambda_3}{(\lambda_2 - \lambda_1)(\lambda_3 - \lambda_1)(\lambda_3 - \lambda_2)}[(\lambda_3 - \lambda_2)e^{-\lambda_1 t} - (\lambda_3 - \lambda_1)e^{-\lambda_2 t} + (\lambda_2 - \lambda_1)e^{-\lambda_3 t}] \tag{5.25}$$

The probability for the granddaughter decay to occur *within* a time t is:

$$F_3(\lambda_1, \lambda_2, \lambda_3, t) = 1 - \frac{\lambda_1 \lambda_2 \lambda_3}{(\lambda_2 - \lambda_1)(\lambda_3 - \lambda_1)(\lambda_3 - \lambda_2)}[\frac{(\lambda_3 - \lambda_2)}{\lambda_1}e^{-\lambda_1 t} - \frac{(\lambda_3 - \lambda_1)}{\lambda_2}e^{-\lambda_2 t} + \frac{(\lambda_2 - \lambda_1)}{\lambda_3}e^{-\lambda_3 t}] \tag{5.26}$$

Using Poisson statistics, the probability for *observing* exactly r background events within a time window t_c, given an average background rate of b is

$$B_r = \frac{(bt_c)^r e^{-bt_c}}{r!} \tag{5.27}$$

5.8.2 Probability Function for Observation of No Decays

To this point we have talked only about the probability for real decay events to *occur*. For the MLH analysis, we need expressions concerning the probability for decay events to be *detected*. As an example, here is how the probability for no events to be detected is built up. Take D_i to be the probability that an ith generation decay occurs, O_i the probability that it is observed, and ϵ_i the detection efficiency for the ith generation decay. In addition, $\bar{x} = 1 - x$ for all variables.

$$P_0 = (\bar{D}_1 + D_1\bar{O}_1\bar{D}_2 + D_1\bar{O}_1D_2\bar{O}_2\bar{D}_3 + D_1\bar{O}_1D_2\bar{O}_2D_3\bar{O}_3) \times B_0 \tag{5.28}$$

where B_0 is the probability for exacty 0 background decays observed within the observation window according to Equation 5.27. The four terms in Equation 5.28 correspond to the four possible ways of observing no decays, assuming three decay generations are possible: 1) the parent does not decay, 2) the parent decays but is not observed and the daughter does not decay, 3) the parent decays but is not observed, the daughter decays but is not observed, and the granddaughter does not decay, and 4) the parent, daughter, and granddaughter all decay, but none are observed. After some arithmetic, this situation is expressible using the above probability functions and the detection efficiencies as:

$$P_0(\lambda_1, \lambda_2, \lambda_3, t) = [1 - F_1(\lambda_1, t)\epsilon_1 - F_2(\lambda_1, \lambda_2, t)\bar{\epsilon}_1\epsilon_2 - F_3(\lambda_1, \lambda_2, \lambda_3, t)\bar{\epsilon}_1\bar{\epsilon}_2\epsilon_3] \times B_0 \tag{5.29}$$

Obtaining Background Rates from No-Decay Probability Function

If the decay efficiencies and decay constants are known, one can use the expression for P_0 to calculate the average background rate from the number of events where no decays were observed, relative to the number of events where at least one decay event was observed. If N_0 is the number of events were no decays were observed, and N_{123} is the number of events with 1, 2 or 3 correlated decays, then based on the definition

of P_0:

$$\frac{N_0}{N_{123}} = \frac{P_0}{1 - P_0} \tag{5.30}$$

In the experiment, both N_0 and N_{123} were measured. N_0 is simply the number of implant events to which no decay events are correlated, and N_{123} is the number of implant events to which at least one decay event is correlated. From Eqn. 5.27 with r=0, the average background rate b is:

$$b = \frac{-\ln B_0}{t_c} \tag{5.31}$$

where B_0 is calculated from Eqns. 5.29 and 5.30:

$$B_0 = \frac{N_0}{N_0 + N_{123}} \times (1 - F_1\epsilon_1 - F_2\bar{\epsilon}_1\epsilon_2 - F_3\bar{\epsilon}_1\bar{\epsilon}_2\epsilon_3)^{-1} \tag{5.32}$$

The average background rate was calculated for the high-statistics cases in Ni, Cu, and Zn, assuming the literature values of the decay constant. The results are shown in Figure 5.15. The results are consistant with the background rates derived by other methods such as from the curve fits. For the case of ^{75}Ni, the background rate derived by this method is larger than that derived by the "blocking window" method as described later, but is consistant with the background derived from curve-fitting.

5.8.3 Probability Functions for the Observation of at Least One Decay

The probabilities for detecting one, two, and three decays can be constructed in a similar way to P_0. These terms are quite long and will not be given here. Using arguments similar to those used for finding P_0, one finds the probability density functions p_i for i decays being observed.

5.8.4 The Likelihood Function

The likelihood function is the product of the probability density function for every event with one (n_i=1), two (n_i=2), or three (n_i=3) decays:

$$\mathcal{L}_{123}(\lambda_1) = \prod_{i=1}^{N_{123}} (\delta(n_i - 1)p_1 + \delta(n_i - 2)p_2 + \delta(n_i - 3)p_3) \tag{5.33}$$

where the product is over all events with one, two, or three decays, and δ(x)=1 for x=0, and δ(x)=0 for x $\neq$ 0. One then finds the most probable value of λ_1, which is the value of λ_1 that maximizes $\mathcal{L}_{123}$.

5.8.5 Probability Functions Including Possible P_n

For this analysis, the probability for neutron emission could be large enough that this decay mode cannot be ignored in the likelihood function. Probability functions were therefore constructed to account for the possibility of neutron emission in the first two decay generations. As an example, the probability function P_0 from Equation 5.29 was modified to:

$$\begin{aligned}
P_0(\lambda_1, \lambda_2, \lambda_3, \lambda_{2n}, \lambda_{3n}, \lambda_{3nn}, t) \quad &= [1 - F_1(\lambda_1)\epsilon_1 && (5.34)\\
&-((1 - P_n)F_2(\lambda_1, \lambda_2) && (5.35)\\
&+P_n F_2(\lambda_1, \lambda_{2n}))\bar{\epsilon}_1\epsilon_2 && (5.36)\\
&-((1 - P_n)(1 - P_{nn})F_3(\lambda_1, \lambda_2, \lambda_3) && (5.37)\\
&+(1 - P_n)P_{nn}F_3(\lambda_1, \lambda_2, \lambda_{3n}) && (5.38)\\
&+P_n(1 - P_{n2n})F_3(\lambda_1, \lambda_{2n}, \lambda_{3n}) && (5.39)\\
&+P_n P_{n2n}F_3(\lambda_1, \lambda_{2n}, \lambda_{3nn}))\bar{\epsilon}_1\bar{\epsilon}_2\epsilon_3] \times B_0 && (5.40)
\end{aligned}$$

where P_n, P_{nn} and P_{n2n} are the neutron emission probabilities of the parent, daughter, and the daughter assuming neutron emission of the parent (N-1 daughter), and λ_{2n},

λ_{3n} and λ_{3nn} are the decay constants for N-1 daughter, the granddaughter assuming the N-1 daughter does not emit a neutron (N-1 granddaughter), and the granddaughter assuming the daughter does emit a neutron (N-2 granddaughter).

5.8.6 Inputs into the MLH Calculation

Half-lives and P_ns in the Decay Chain

Experimental values for the daughter and granddaughter decay properties were used whenever available. The experimentally unknown P_n values for the Ni isotopes were taken from detailed spherical quasi-particle random-phase (QRPA) calculations for pure Gamow-Teller (GT) and GT with first-forbidden decay [61] and a number of different choices of single-particle potentials and mass model predictions. From a comparison of the different theoretical P_n values, we derive an average uncertainty for the calculated P_n values of about a factor of two. Table 5.7 gives the decay properties that were used as inputs in the analysis.

Background

The β background was determined in three ways: 1) from fitting decay curves as discussed in a previous section, 2) from the expression for P_0 as discussed above, and 3) from directly counting uncorrelated β-type events. For method 3), the background was determined for each run (typical duration of 1h) and in each detector pixel by counting all decay events that occur outside of a 100 s time window following an implantation. A background rate for each isotope was then found by averaging the background rate over the run-averaged background rate for all pixels in which the isotope was implanted. Because of the low implantation rate the background is constant over the 5 s time window used to correlate decays to an implantation. This last method of determining background rates gives by far the smallest uncertainty of all the methods since it utilizes much higher statistics than either the fitting method or the P_0 method,

and also does not depend on input parameters such as decay constants and efficiencies as do the other methods.

Efficiencies

The efficiencies for the three decay generations were taken from the curve fits as discussed in Section 5.7.1 for the high statistics cases (see Table 5.6). For the other isotopes, an average value of $42 \pm 1\%$ was used. In the MLH analysis, the efficiency of the parent was used for each of the subsequent decay generations.

5.8.7 Examples of Likelihood Functions

Figure 5.16 shows the log of the likelihood function for the sum of all the 8 ^{78}Ni decay chains individually as an example. Figure 5.17 shows the log of the likelihood function for each of the 8 ^{78}Ni decay chains.

The results of the MLH calculations can be found in Table 5.8.

5.8.8 Error Contributions in the MLH

Statistical Error Contributions

The statistical error of the derived decay half-lives is obtained directly from the maximum likelihood analysis (see Ref [60],Schneider96) and is valid even in the case of very low statistics. The validity of the statistical error bars were tested with input data resulting from Monte-Carlo simulation. Decay chains similar to the actual data were simulated and run through the analysis. A sample of the results for ^{78}Ni-type simulations are shown in Figure 5.18. Each set analysed consists of only 8 Monte Carlo simulated decay chains to simulate the real 8 ^{78}Ni decay-chain analysis. The Monte Carlo input data had a half-life of 0.130 seconds. The number of sets for which this input half-life falls within the error bars of the output half-life is 63%, slightly smaller than the usual 68% confidence level, but the result confirms the error bars

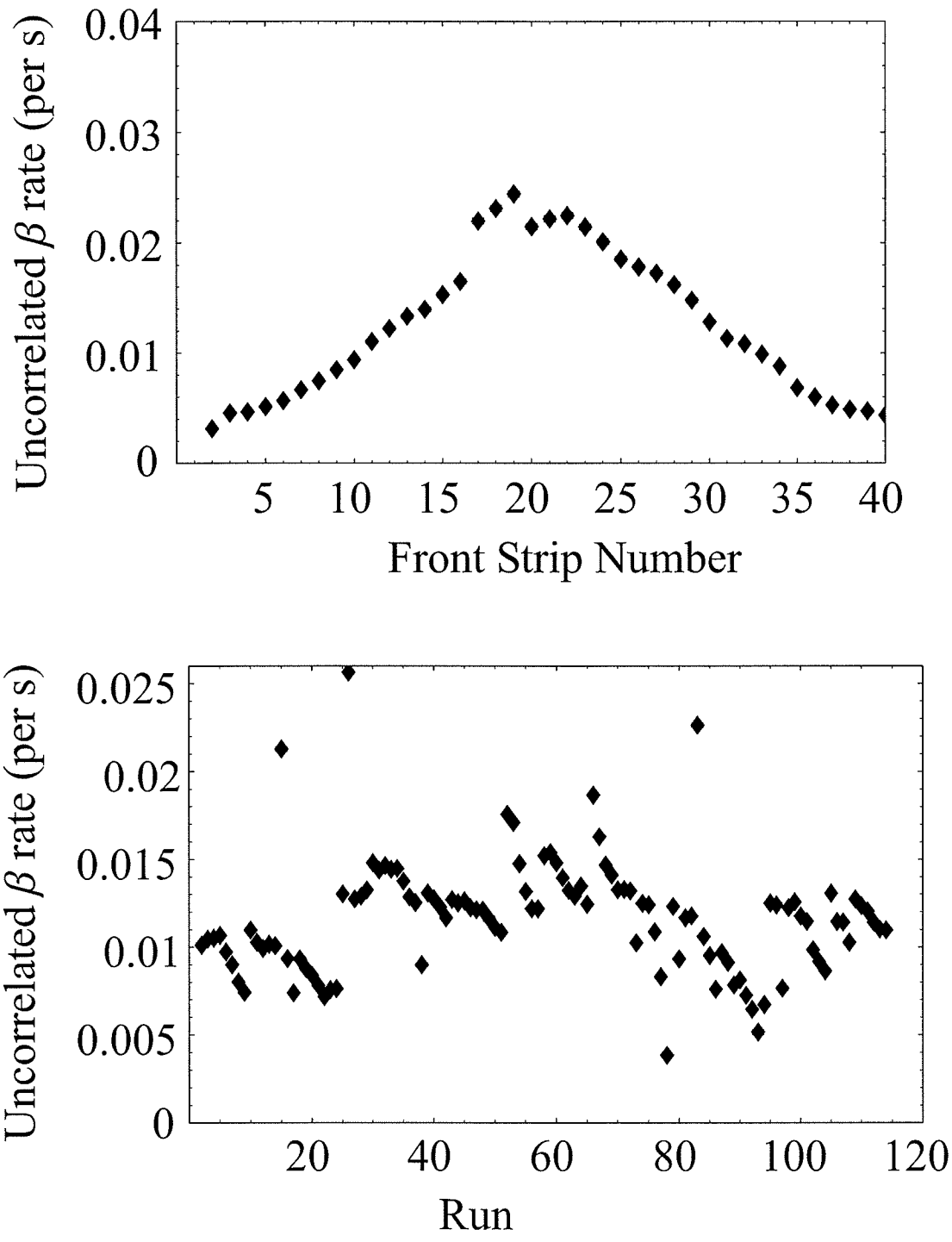

Figure 5.14: β-background as a function of front strip number for a representative back strip, and β-background averaged over the DSSD as a function of run.

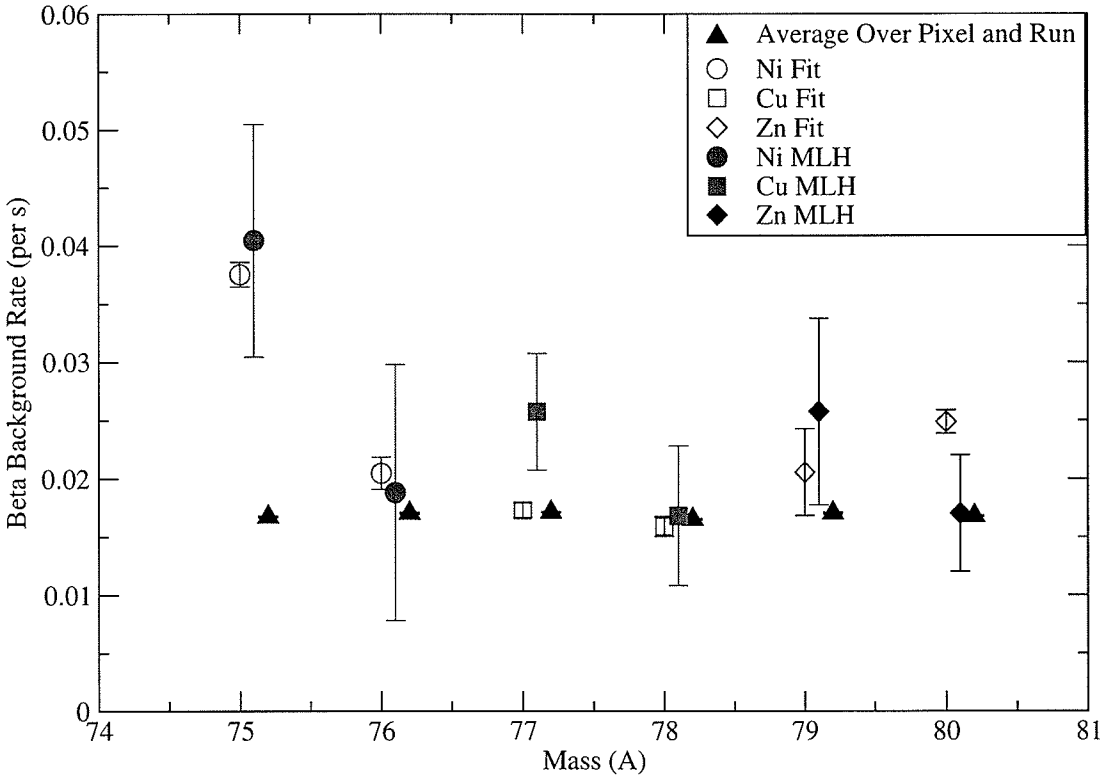

Figure 5.15: β background by three different methods, shown for cases with high statistics.

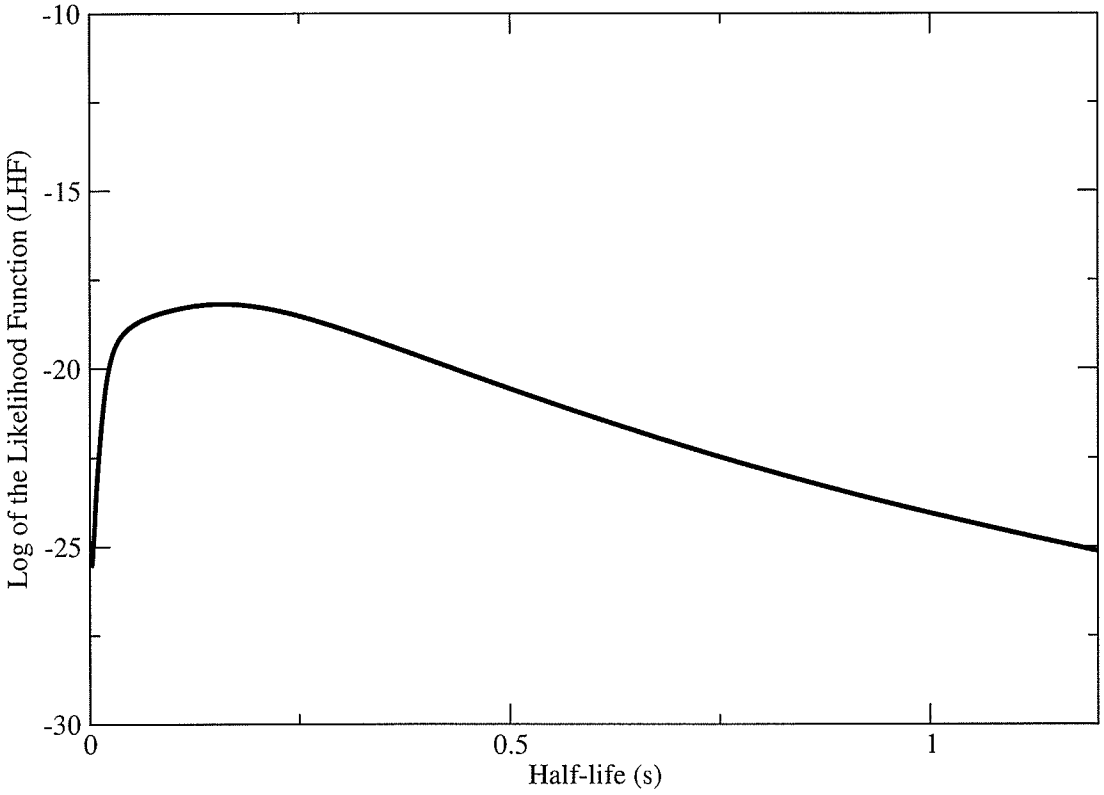

Figure 5.16: Likelihood functions for the sum of the 8 ^{78}Ni decay chains.

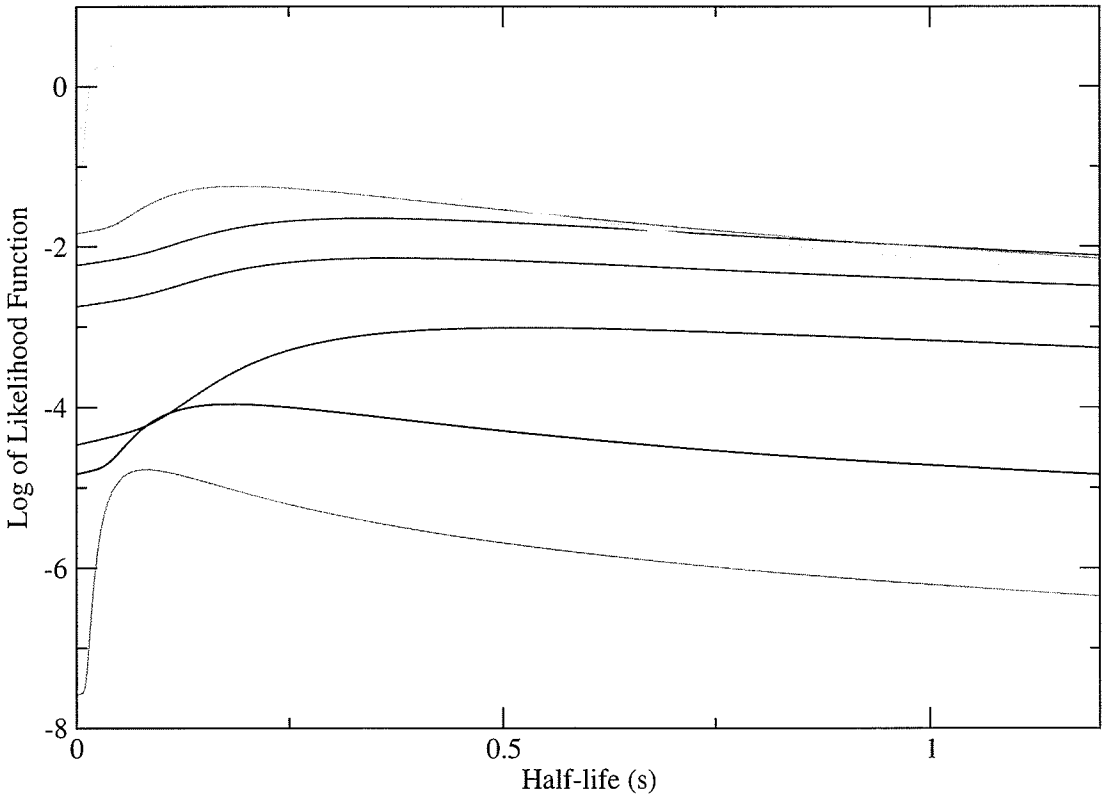

Figure 5.17: Likelihood functions for each of the 8 ^{78}Ni decay chains.

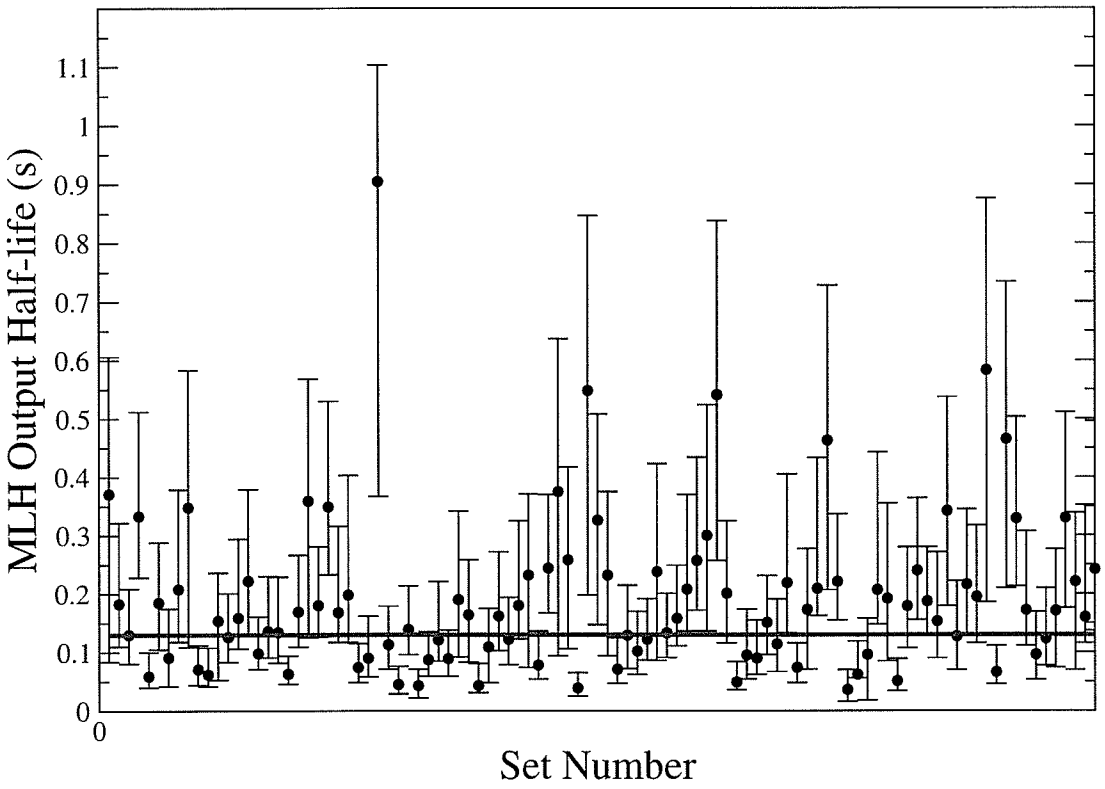

Figure 5.18: MLH analysis output of 100 8-decay-chain sets of Monte Carlo simulated data with input half-life of 0.130 s.

are reasonable, even in the case of very low statistics.

Systematic Error Contributions

The uncertainties in the input half-lives of the daughter, N-1 daughter, granddaughter, N-1 granddaughter, and N-2 granddaughter all result in systematic errors in the MLH output, as well as the P_n values for the same nuclei, the background, and the *beta*-detection efficiency.

These uncertainties were taken into account in the following way. Each of the above values was varied within it's respective uncertainties, and all possible permutations of all of these variations of all inputs were calculated. The nominal value was taken to be the value calculated assuming the nominal value of all the inputs. Systematic and statistical errors are correlated since the shape of the likelihood function

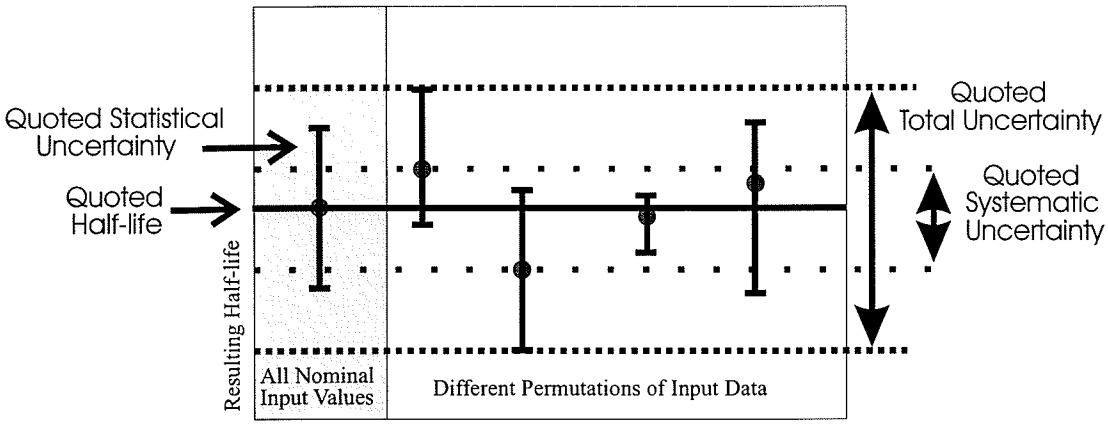

Figure 5.19: A sketch demonstrating how the quoted uncertainties were obtained. The points and error bars are rough sketches, not actual data.

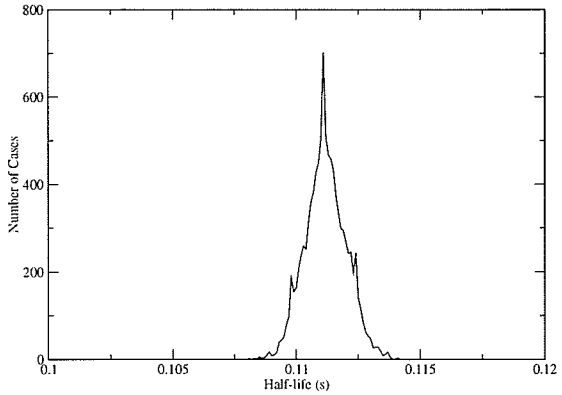

Figure 5.20: Monte Carlo distribution of ^{78}Ni half-lives for background varying within the background uncertainty range.

depends on the analysis parameters. We therefore reran the analysis for all combinations of systematic variations and employed the lower and upper one-sigma limits of the resulting statistical errors as the total error budget. As a result of this method, the quoted statistical error and the systematic error do not necessarily add up to the total error (see Figure 5.19). The main contribution to the systematic errors are uncertainties in the detector efficiency, and uncertainties in the parent P_n values.

In the case of ^{78}Ni, due to the low statistics we also took into account the possibility that one of the events is misidentified. Given the very low number of events beyond ^{78}Ni in the particle identification, this is a very conservative assumption. Each of

the eight decay chains were successively removed and the half-life was redetermined for the remaining seven decay chains. The resulting range in half-lives leads to an additional systematic error for ^{78}Ni of $^{+10}_{-0}$ms.

5.9 Isomerism in the decay chain

In principle the analysis depends somewhat on the unknown feeding and decay branchings of the known isomeric states in several nuclei. The isotopes involved in the analysis which have known isomeric states are ^{76}Cu, ^{73}Zn,^{77}Zn, ^{79}Ge, ^{81}Ge and ^{82}As (Nudat). ^{76}Cu has two isomeric states, one with a half-life of 0.641 s and the other with a 1.27 s half-life. Both of these states are supposed to decay 100% by β-. The relative feeding to these states is not known. Most of the delayed neutrons probably come from the 0.641 s state. ^{73}Zn has three isomeric states, with half-lives of 23.5 s, 5.8 s, and 13.0 ms respectively. The first and third decay 100% by negative β-decay. The second is not known. ^{77}Zn has two isomeric states with half-lives of 2.08 s and 1.05 s. The first decays 100% by β-decay. The second decays more than 50% by internal transitions, and less than 50% by β-decay, with the β-decay branch probably an order of magnitude smaller. ^{79}Ge has two isomeric states with half-lives of 18.98 s and 39.0 s. The first decays 100% by β- decay. The second is 96% by β and 4% by IT. ^{81}Ge has two isomeric states, both are given as 7.6 s half-life. The first decays 100% by β- decay. The second may have a small branch to IT. ^{82}As has two isomeric states with half-lives of 19.1 s and 13.6 s. Both decay 100% by β- decay.

As an example of how these isomers can affect the half-life results, consider the following cases. Assuming decay from the isomeric state with a half-life of 1.27 s for ^{76}Cu would increase the ^{76}Ni half-life by no more than 12 ms and the ^{77}Ni half-life by no more than 5 ms. Assuming population of the 1.05 s isomer for ^{77}Zn could change the half-life of ^{77}Ni by -8 ms to +13 ms, and the half-life of ^{78}Ni by -10 ms to +15 ms depending on the probability for that state to β-decay.

The uncertainties resulting from the existance of isomers in the chain are based on extreme assumptions with no obvious central value. We therefore do not include them in our systematic error bars.

5.10 Half-life Results

The final half-life results are shown in Figure ?? and compared to previous measurements.

5.11 Neutron Analysis

5.11.1 Neutron Spectra

During the experiment, when any DSSD event on the high-gain side occured, a 200μs gate was openned on NERO to allow the observation of neutrons. NERO data was collected by ADCs which recorded an energy spectrum, and a TDC which recorded the time from the triggering decay event to any neutron event. When the energy spectrum is gated to cut out the low energy noise signals, the number of counts in the energy and time spectra agreed to less than 2%. The TDC registers only events above threshold, but registers all events within the measuring window, while the ADC registers counts independent of threshold, but only the first event within the measuring window. The agreement between these two methods of counting implies that the software cuts applied to the energy spectra (see Table 5.10) agree with the set thresholds (see Table 5.9), and also that multiple hits in the counters are rare. Figures 5.22, 5.23, 5.24, and 5.25 show the ADC energy spectra for this experiment. The noise that is visible in counters D7 and D11 was gated out in the analysis. Figure 5.26 shows the neutron time spectra for each of the three NERO rings.

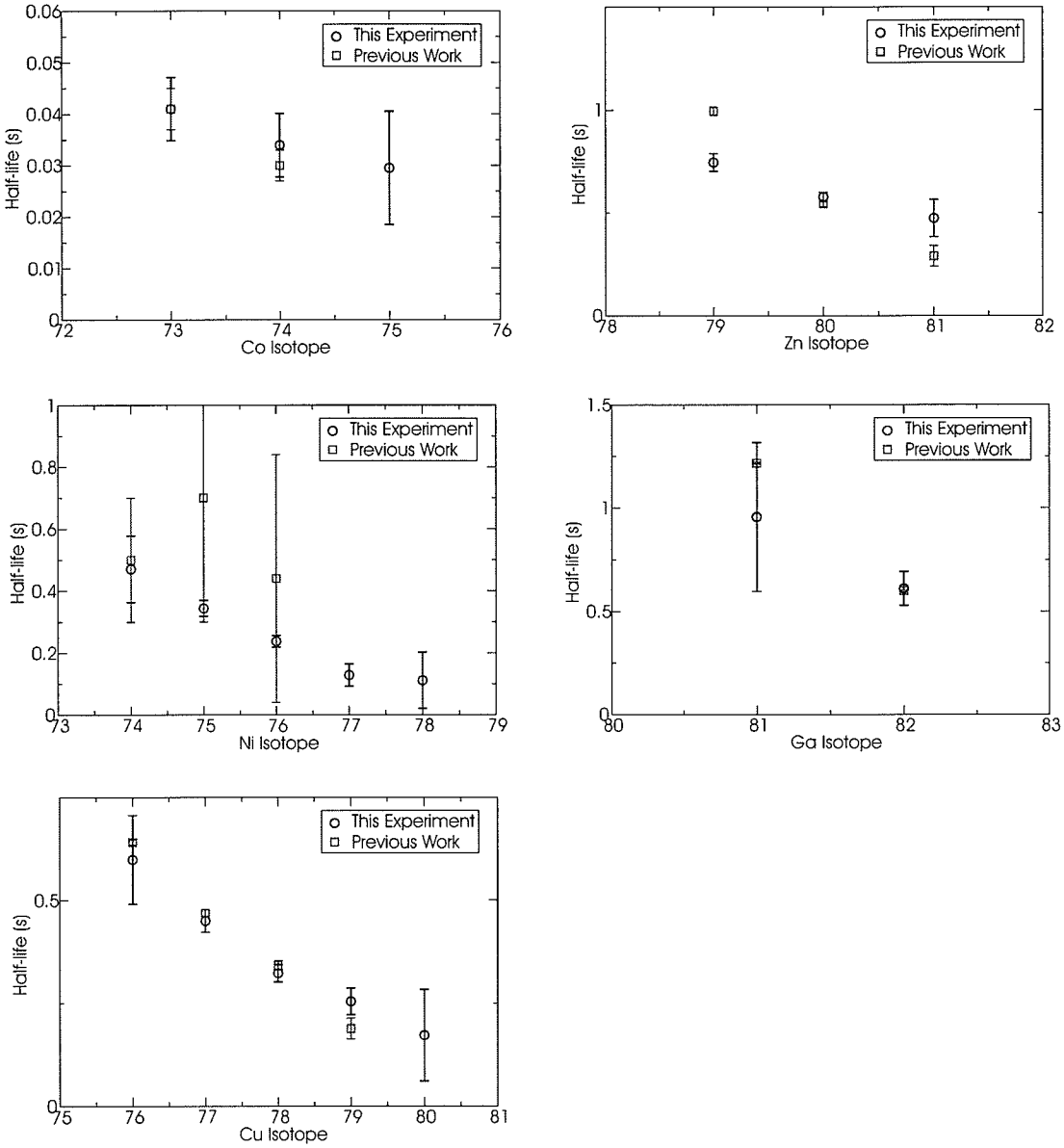

Figure 5.21: half-lives from this experiment and previous work.

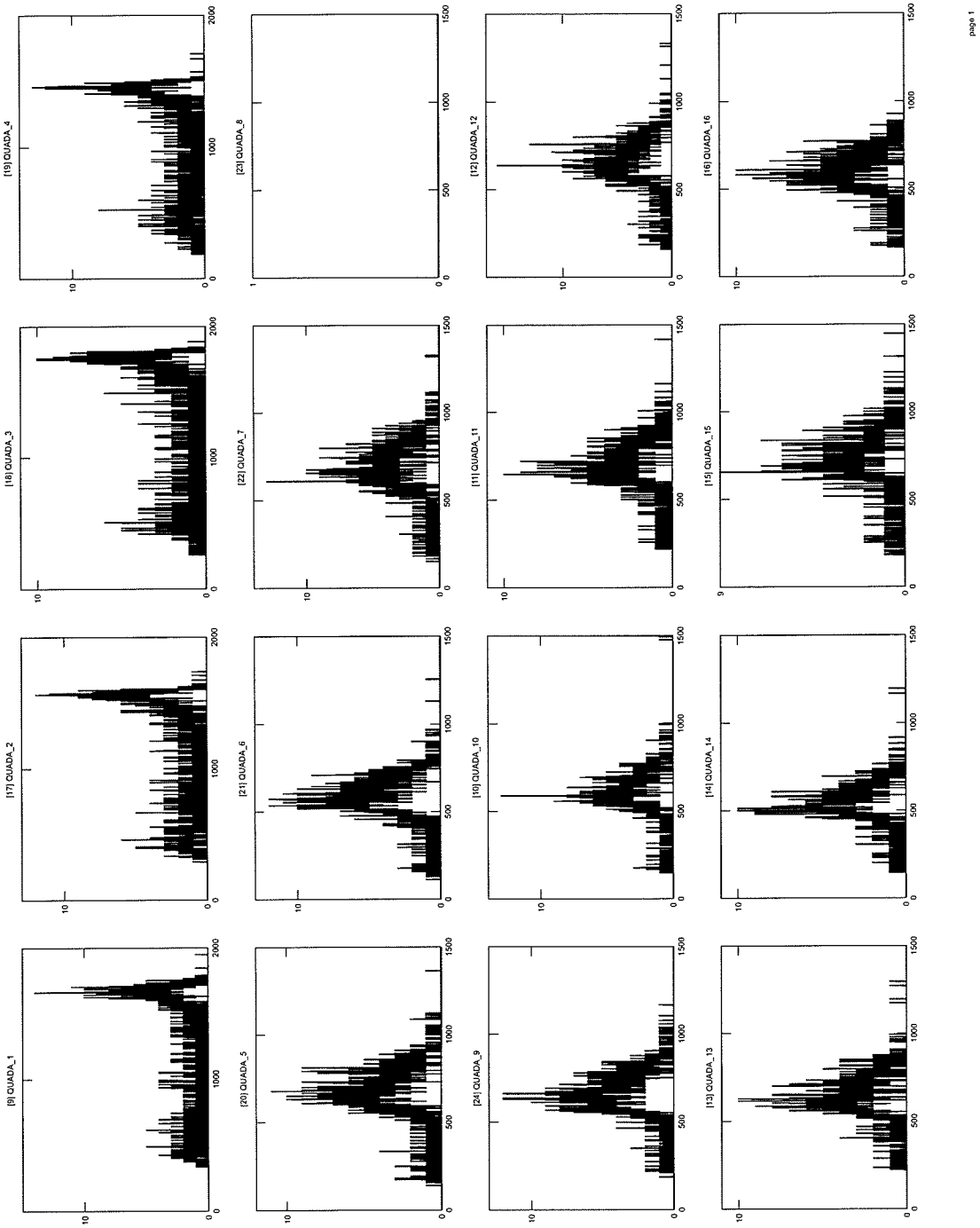

Figure 5.22: Neutron energy spectra from NERO quandrant A.

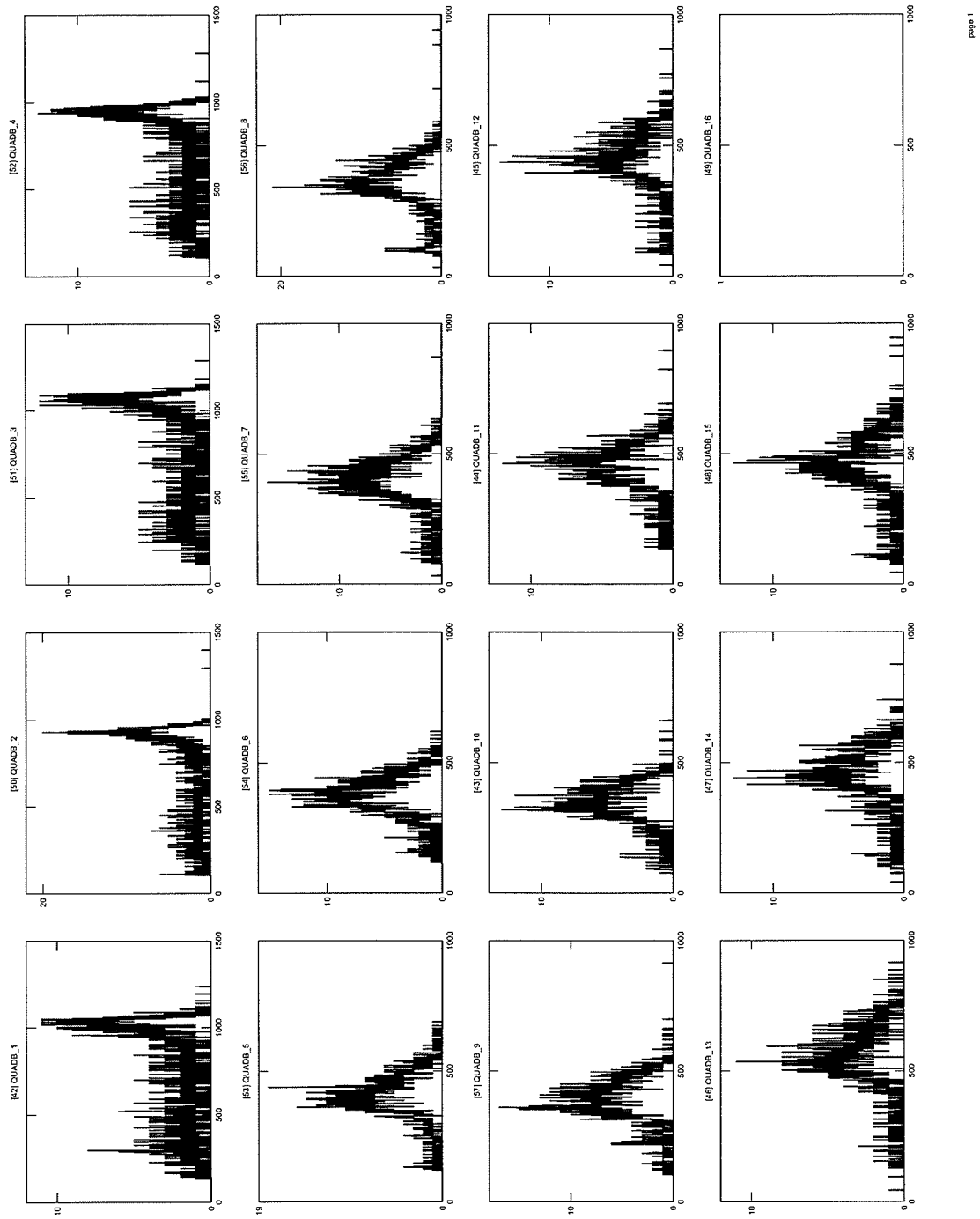

Figure 5.23: Neutron energy spectra from NERO quandrant B.

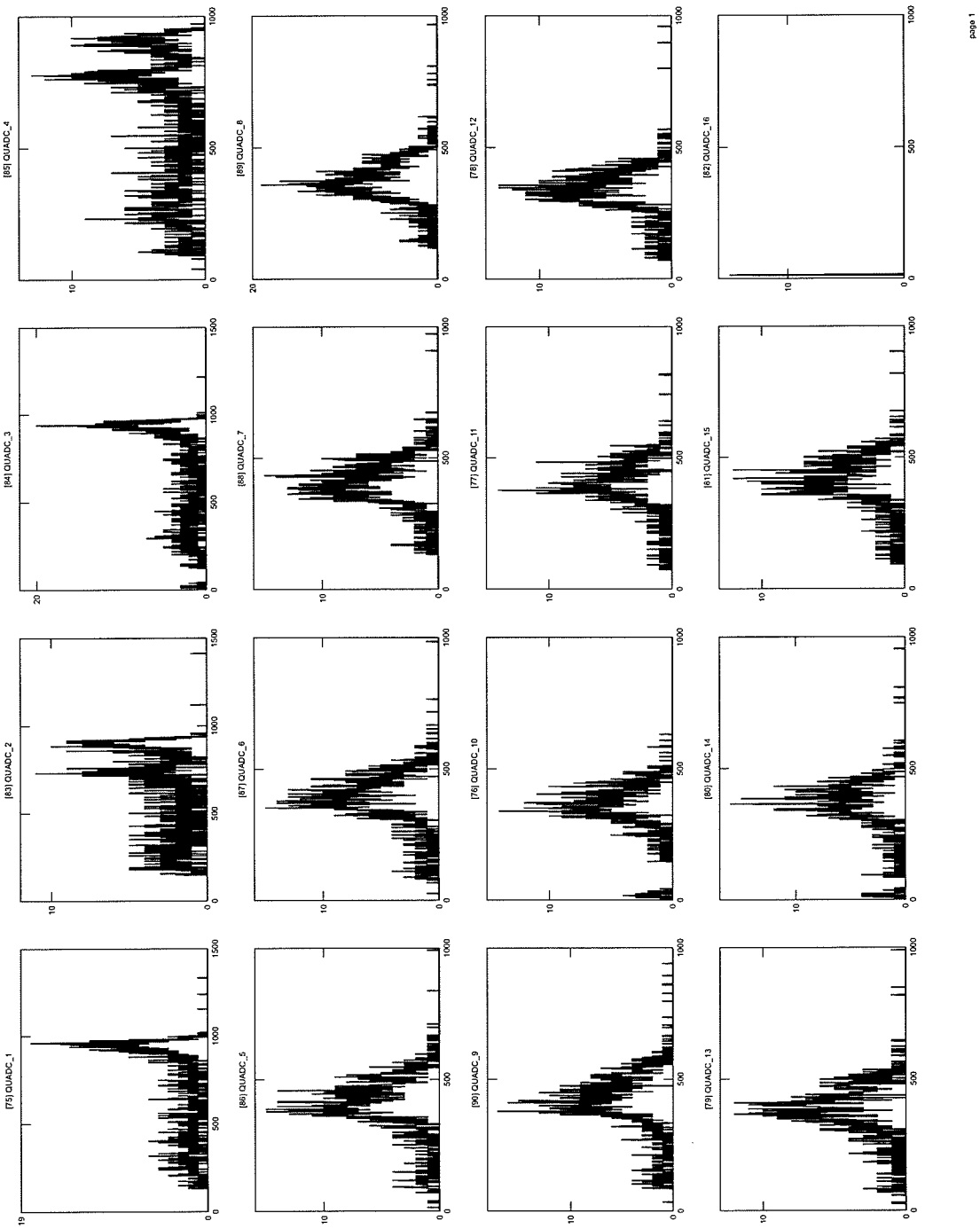

Figure 5.24: Neutron energy spectra from NERO quandrant C.

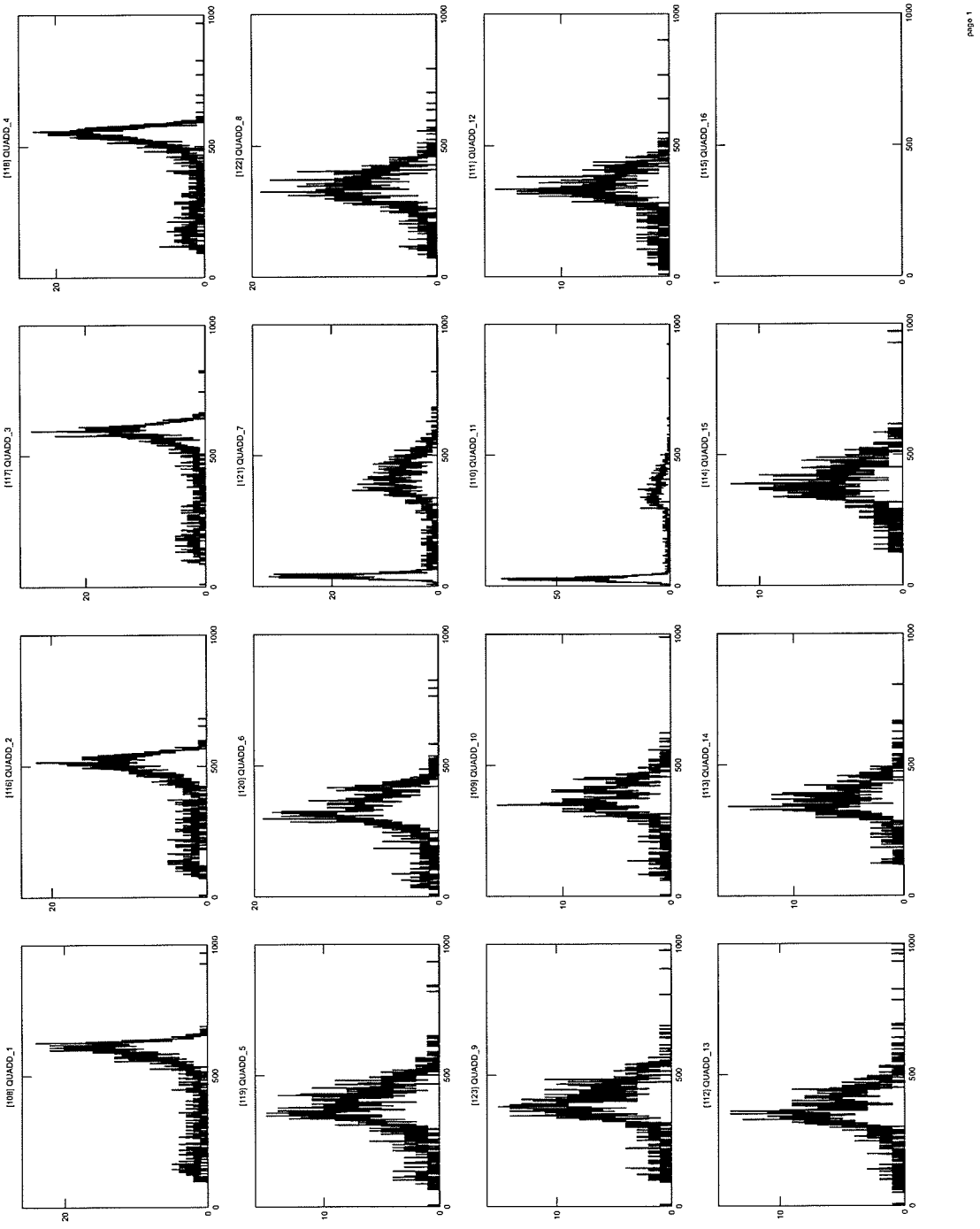

Figure 5.25: Neutron energy spectra from NERO quandrant D.

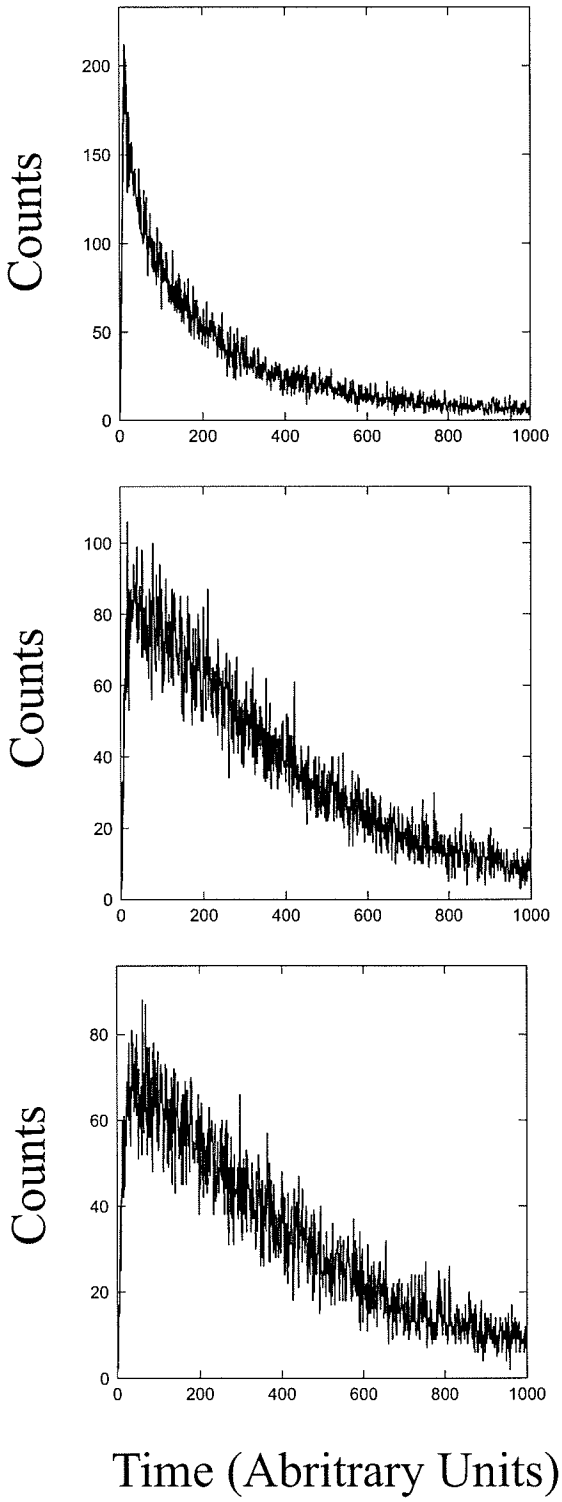

Figure 5.26: Neutron time spectra from the three NERO rings. The graphs show the full 200 μs neutron window.

5.11.2 Calculating P_n values

For a given isotope, the P_n value in % is calculated using the equation:

$$P_n = 100 \times \frac{N_{\beta-n}}{N_{\beta parent}} \tag{5.41}$$

$N_{\beta parent}$ is the number of parent calculated from:

$$N_{\beta parent} = N_{imp}(1 - e^{-\lambda t_{corr}}) \tag{5.42}$$

where N_{imp} and λ are the number of implants and decay constant of the given isotope. The λ used were those derived from the MLH analysis. $N_{\beta parent}$ is the actual number of parent β-decays within the correlation time t_{corr} after every implant of a given isotope. The number $N_{\beta-n}$ is the number of β-n coincidences detected within t_{corr} corrected for background and detection efficiencies:

$$N_{\beta-n} = \frac{N_{\beta-ndetected} - N_{\beta-nbackgrounddetected}}{\epsilon_{\beta-n}} \tag{5.43}$$

$N_{\beta-ndetected}$ is the raw number of β-n coincidences detected within the correlation time following each implant. $N_{\beta-nbackgrounddetected}$ is detected number of random β-n coincidences within the correlation time following each implant (see Section 5.11.2). $\epsilon_{n-\beta}$ is the product of the neutron detection efficiency and the β detection efficiency:

$$\epsilon_{n-\beta} = \epsilon_{nero}\epsilon_{\beta} \tag{5.44}$$

were ϵ_{nero} is the neutron-energy-dependent NERO detector efficiency (see Section 5.11.2 and ϵ_{β} is the β-detection efficiency from Section 5.7.1.

Neutron Energies and Detection Efficiency

The neutron energies were taken from shell-model calculations carried out at the NSCL by A. Lisetskiy [63, 64] which will be described in more detail in the next chapter. For the Ni and Cu isotopes for which calculations were available, the neutron energy branchings were folded with the NERO efficiency curve to produce a weighted efficiency. The weighted neutron energies and efficiencies can be found in Table 5.11. The energy dependence of the fitted NERO efficiency curve in this energy range is fairly flat, ranging just 4% from 36.5% to 32.5% within the energy range of 0.1 MeV to 1 MeV. The uncertainty in the efficiency therefore has only a small dependence on the uncertainty in the energy within this range. For example, if the neutron energy of 0.75 MeV is only known with an uncertainty as large as $\pm 30\%$, then the resulting absolute uncertainty in the efficiency due only to the energy dependence of the fitted curve is less than $\pm 1\%$. The largest uncertainty in the calculated efficiency is then the systematic uncertainty in the fitted curve. This uncertainty is taken to be $\pm 2\%$.

For the isotopes for which the neutron energy calculations were not available, their average neutron energies were conservatively assumed to be within the range 0.1 to 1 MeV. The central efficiency value of this energy range is 34.5%. This possible energy range results in a systematic uncertainty of $\pm 2\%$. When added to the additional systematic uncertainty in the fit curve, the resulting uncertainty in efficiency for these isotopes is $\pm 4\%$.

Neutron Background

From Section 5.11.2, the detected number of β-n events was corrected by the detected number of β-n background events. The number of β-n background events for a given isotope was determined based on the equation:

$$N_{\beta-nbackgrounddetected} = (Rate_{\beta-ndetected}) \times t_{corr} \times N_{imp} \tag{5.45}$$

The rate $Rate_{\beta-ndetected}$ was determined on a pixel by pixel basis by averaging the random β-n coincidence rate for a given pixel over all runs to increase the counting statistics. For a given isotope, the background rate was then assigned based on the run-averaged rate only in pixels in which that isotope was implanted. Figure 5.27 shows the random β-n coincidence rate for the entire detector as a function of run. Figure 5.27 also shows the random β-n coincidence rate averaged over all runs as a function of DSSD front strip number for a representative back strip number. It can be seen that the random β-n coincidence rate varies as a function of both strip number and run. However, since the β rate varies in a similar way as a function of both strip and run the result is that the number of random β-n coincidences per β event is fairly constant except in several contiguous runs which display systematically lower neutron counts. (see Figure 5.27). For this analysis, the background was averaged over run.

5.12 P_n Value Results

The resulting P_n values and are given in Table 5.12 and plotted in Figure 5.28 along with values from previous works.

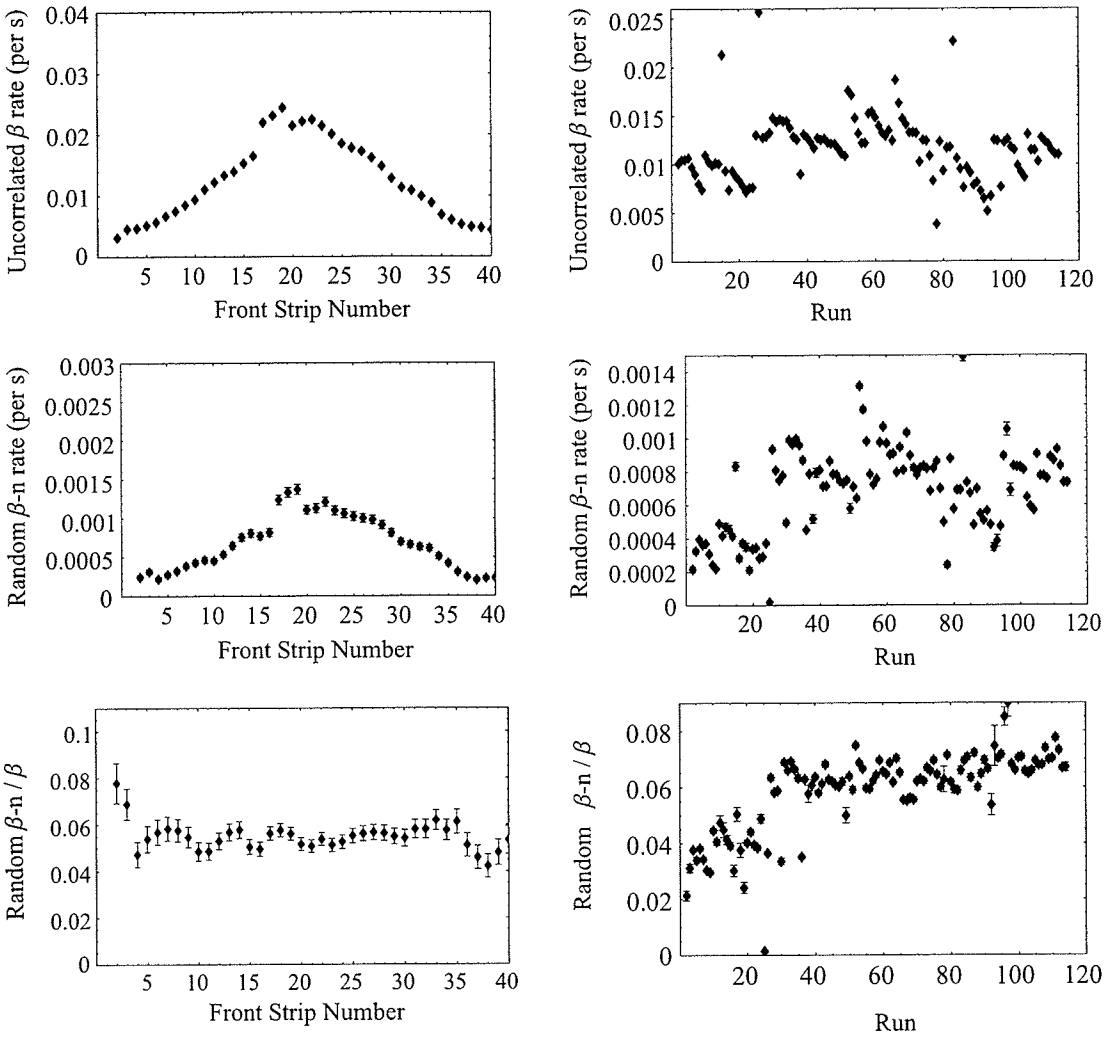

Figure 5.27: β-background rate, random β-n coincidence rate, and number of random β-n coincidences per β event as a function of DSSD front strip number for a representative back strip (strip 20) and for the entire DSSD as a function of run.

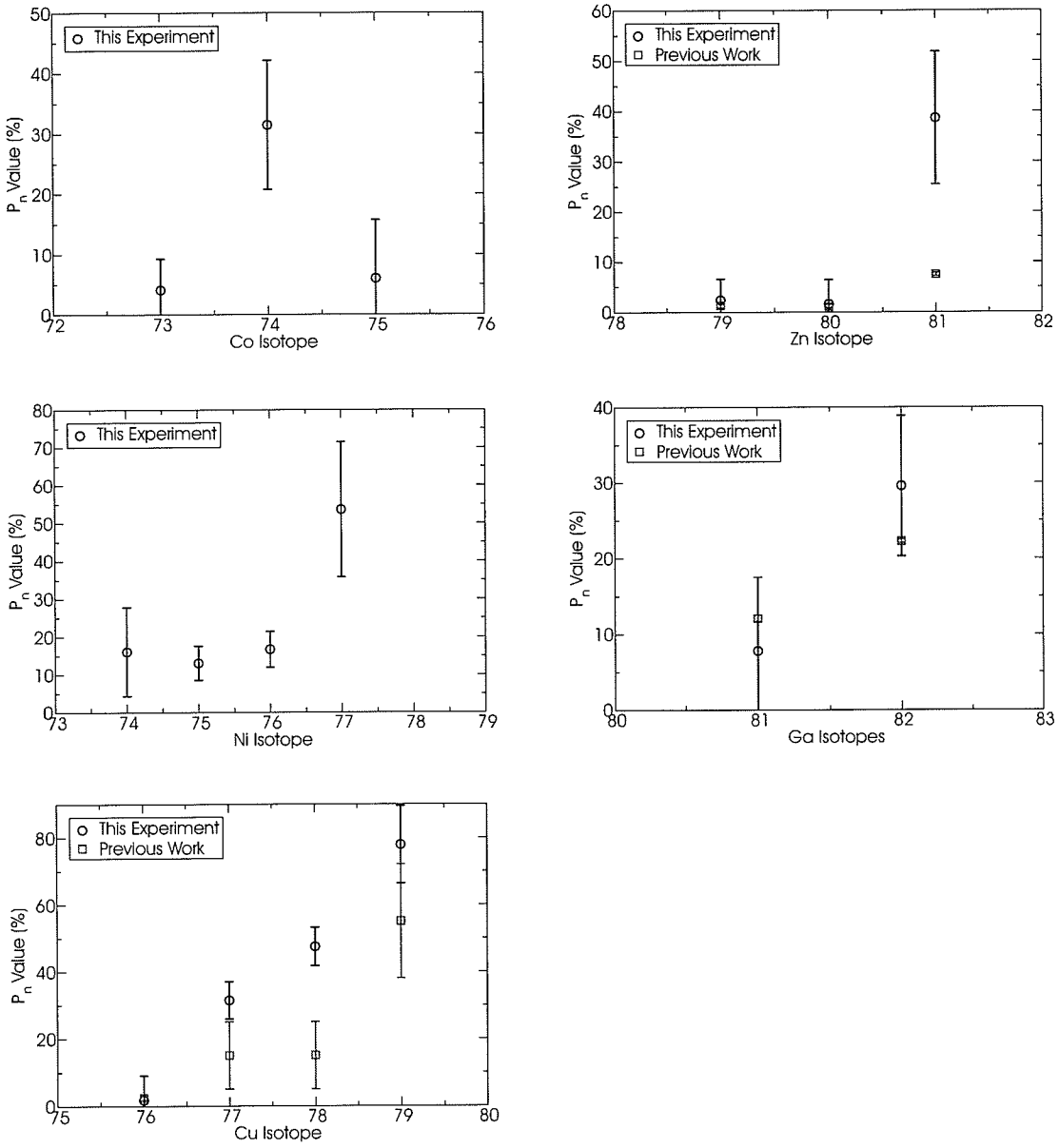

Figure 5.28: P_n values from this experiment and previous work.

Table 5.7: Inputs for MLH Half-life Calculation

Isotope	$t_{1/2}$ (s)	P_n (Fraction)	Reference
^{72}Ni	1.57 ± 0.05	0	[62]
^{73}Ni	0.84 ± 0.03	0.0026	[62]
^{74}Ni	0.5 ± 0.2	0.02853	[62]
^{75}Ni	0.7 ± 0.4	0.09127	[62]
^{71}Cu	19.5 ± 1.6	0	NuDat
^{72}Cu	6.6 ± 0.1	0	NuDat
^{73}Cu	3.9 ± 0.3	0.00029 ± 0.00006	[62]
^{74}Cu	1.594 ± 0.01	0.00075 ± 0.00016	[62]
^{75}Cu	1.224 ± 0.003	0.026 ± 0.005	[62]
^{76}Cu	0.641 ± 0.006	0.024 ± 0.005	[62]
^{77}Cu	0.469 ± 0.008	$0.15^{0.1}_{0.05}$	[62]
^{78}Cu	0.342 ± 0.011	$0.15^{0.1}_{0.05}$	[62]
^{72}Zn	167400 ± 360	0	NuDat
^{73}Zn	23.5 ± 1	0	NuDat
^{74}Zn	95.6 ± 1.2	0	NuDat
^{75}Zn	10 ± 0.2	0	NuDat
^{76}Zn	5.7 ± 0.3	0	NuDat
^{77}Zn	2.08 ± 0.05	0	[62]
^{78}Zn	1.47 ± 0.15	0	[62]
^{79}Zn	0.995 ± 0.019	0.013 ± 0.004	[62]
^{80}Zn	0.545 ± 0.016	0.01 ± 0.005	[62]
^{74}Ga	487.2 ± 7.2	0	NuDat
^{75}Ga	126 ± 2	0	NuDat
^{76}Ga	32.6 ± 0.6	0	NuDat
^{77}Ga	13.2 ± 0.2	0	NuDat
^{78}Ga	5.09 ± 0.05	0	NuDat
^{79}Ga	2.847 ± 0.003	0.0008 ± 0.00014	[62]
^{80}Ga	1.697 ± 0.011	0.0085 ± 0.0006	[62]
^{81}Ga	1.217 ± 0.005	0.121 ± 0.004	[62]
^{77}Ge	40680 ± 36	0	NuDat
^{78}Ge	5280 ± 60	0	NuDat
^{79}Ge	18.98 ± 0.03	0	NuDat
^{80}Ge	29.5 ± 0.4	0	NuDat
^{81}Ge	7.6 ± 0.6	0	NuDat
^{79}As	540.6 ± 9	0	NuDat
^{80}As	15.2 ± 0.2	0	NuDat
^{81}As	33.3 ± 0.8	0	NuDat
^{82}As	19.1 ± 0.5	0	NuDat

Table 5.8: $T_{1/2}$ Results from MLH Analysis

Isotope	$T_{1/2}$ (s)	Stat (+)	Stat (-)	Sys (+)	Sys (-)	Total (+)	Total (-)
^{73}Co	0.040988	0.005404	0.004803	0.001001	0.000913	0.006164	0.005613
^{74}Co	0.033977	0.004181	0.003539	0.001791	0.005313	0.006189	0.008676
^{75}Co	0.0295	0.007778	0.006914	0.003153	0.004509	0.011152	0.010401
^{74}Ni	0.470765	0.102405	0.084284	0.007557	0.00682	0.110431	0.0908
^{75}Ni	0.344347	0.018916	0.017935	0.00729	0.005465	0.026203	0.02313
^{76}Ni	0.237776	0.013584	0.013158	0.005255	0.004087	0.019128	0.01703
^{77}Ni	0.128394	0.024826	0.025495	0.010799	0.006732	0.036416	0.032161
^{78}Ni	0.111189	0.077691	0.061169	0.023201	0.009315	0.101954	0.063305
^{76}Cu	0.599152	0.095446	0.079477	0.011951	0.01351	0.109094	0.091845
^{77}Cu	0.449737	0.012847	0.012444	0.014158	0.008581	0.026894	0.020793
^{78}Cu	0.322705	0.011345	0.01103	0.009914	0.008047	0.021232	0.018813
^{79}Cu	0.254057	0.021771	0.019848	0.010697	0.009044	0.032778	0.028609
^{80}Cu	0.171988	0.105057	0.048707	0.003871	0.004055	0.111167	0.052218
^{79}Zn	0.746214	0.037711	0.036436	0.004891	0.004829	0.043256	0.041029
^{80}Zn	0.577882	0.019046	0.018811	0.002492	0.002514	0.021611	0.020785
^{81}Zn	0.474277	0.080764	0.072562	0.01035	0.011421	0.092535	0.08292
^{81}Ga	0.9568	0.330593	0.251892	0.030856	0.034619	0.366263	0.285397
^{82}Ga	0.609823	0.071687	0.062034	0.010426	0.010826	0.083221	0.072349

Table 5.9: NERO dedicated Pico Systems CFD Thresholds for this Experiment (On 255 Scale). The corresponding gain settings were 255 for all counters.

Counter	Thresh.	Counter	Thresh.	Counter	Thresh.	Counter	Thresh.
A1	55	B1	35	C1	30	D1	25
A2	65	B2	25	C2	40	D2	25
A3	40	B3	30	C3	30	D3	25
A4	40	B4	30	C4	255	D4	30
A5	25	B5	30	C5	20	D5	25
A6	25	B6	35	C6	20	D6	23
A7	25	B7	25	C7	35	D7	20
A8	30	B8	25	C8	33	D8	30
A9	30	B9	25	C9	18	D9	30
A10	25	B10	18	C10	40	D10	25
A11	35	B11	35	C11	20	D11	25
A12	25	B12	25	C12	20	D12	20
A13	35	B13	25	C13	15	D13	25
A14	25	B14	20	C14	25	D14	40
A15	30	B15	20	C15	25	D15	35

Table 5.10: NERO Energy Software Cuts on 12-bit (4096) scale

Counter	Cut	Counter	Cut	Counter	Cut	Counter	Cut
A1	200	B1	117	C1	99	D1	80
A2	186	B2	100	C2	103	D2	67
A3	179	B3	111	C3	93	D3	76
A4	152	B4	106	C4	76	D4	76
A5	124	B5	110	C5	72	D5	69
A6	108	B6	100	C6	66	D6	67
A7	123	B7	97	C7	97	D7	81
A8	150	B8	123	C8	88	D8	59
A9	126	B9	96	C9	76	D9	71
A10	123	B10	115	C10	99	D10	56
A11	165	B11	122	C11	72	D11	84
A12	130	B12	151	C12	62	D12	66
A13	163	B13	110	C13	59	D13	67
A14	114	B14	162	C14	68	D14	79
A15	143	B15	170	C15	77	D15	87

Table 5.11: Neutron Energies and Corresponding NERO Efficiencies

Isotope	Neutron Energy (MeV)	NERO Efficiency (%)
^{74}Ni	0.877	33 ± 2
^{75}Ni	0.998	33 ± 2
^{76}Ni	1.06	35 ± 2
^{78}Cu	1.10	32 ± 2
^{79}Cu	1.20	32 ± 2
All Other Isotopes	From 0.1 to 1	34.5 ± 4

Table 5.12: P_n values

Isotope	Raw Neutron Count	P_n from this Work (%)	Previous Measurements (%)
^{73}Co	4	less than 9	
^{74}Co	16	31 ± 11	
^{75}Co	1	less than 16	
^{74}Ni	3	16 ± 12	
^{75}Ni	43	13 ± 5	
^{76}Ni	43	17 ± 5	
^{77}Ni	13	54 ± 18	
^{76}Cu	3	less than 9	2.4 ± 0.5 [17], [65], [62]
^{77}Cu	348	31 ± 6	15 ± 10 [65], [62]
^{78}Cu	310	47 ± 6	15 ± 10 [65], [62]
^{79}Cu	81	78 ± 12	55 ± 17 [23]
^{79}Zn	19	2 ± 5	1.3 ± 0.4 [23]
^{80}Zn	45	1 ± 6	1 ± 0.5 [23]
^{81}Zn	14	62 ± 22	7.5 ± 0.3 [23]
^{81}Ga	1	12 ± 18	12.1 ± 0.4 [66], [62]
^{82}Ga	21	32 ± 12	22.3 ± 0.22 [66], [62]

Chapter 6

Discussion

6.1 QRPA Calculations

Global calculations such as QRPA are employed often in r-process model calculatons because they offer nuclear physics inputs for the wide range of nuclei required for these studies. The experimental values are compared to QRPA calculations in this mass region [67, 68] (see Figures 6.1 and 6.2). These calculations assumed no deformation and used a Folded-Yukawa potential and Lipkin-Nogami pairing, and take into account only allowed Gamow-Teller (GT) transitions. The masses were taken from G. Audi *et al.* 03 [69]. These calculations differ from those found in Ref. [67] in the daughter deformations. In addition, they do not include a "smearing-out" of the levels above around 2 MeV, as does Ref. [67].

The QRPA calculation assuming only allowed GT transitions tends to over-predict the half-lives of the nuclei in this region, but reproduces well the experimentally derived P_n values. There are several possible explanations for the over-prediction of the half-lives. First, the calculation takes into account only allowed transitions. If these transitions feed high-lying states, the higher half-lives will still result (because due to the energy dependence, there will be less energy to drive the transition). However, if there exist first-forbidden branches to low-lying states, lower half-lives will result.

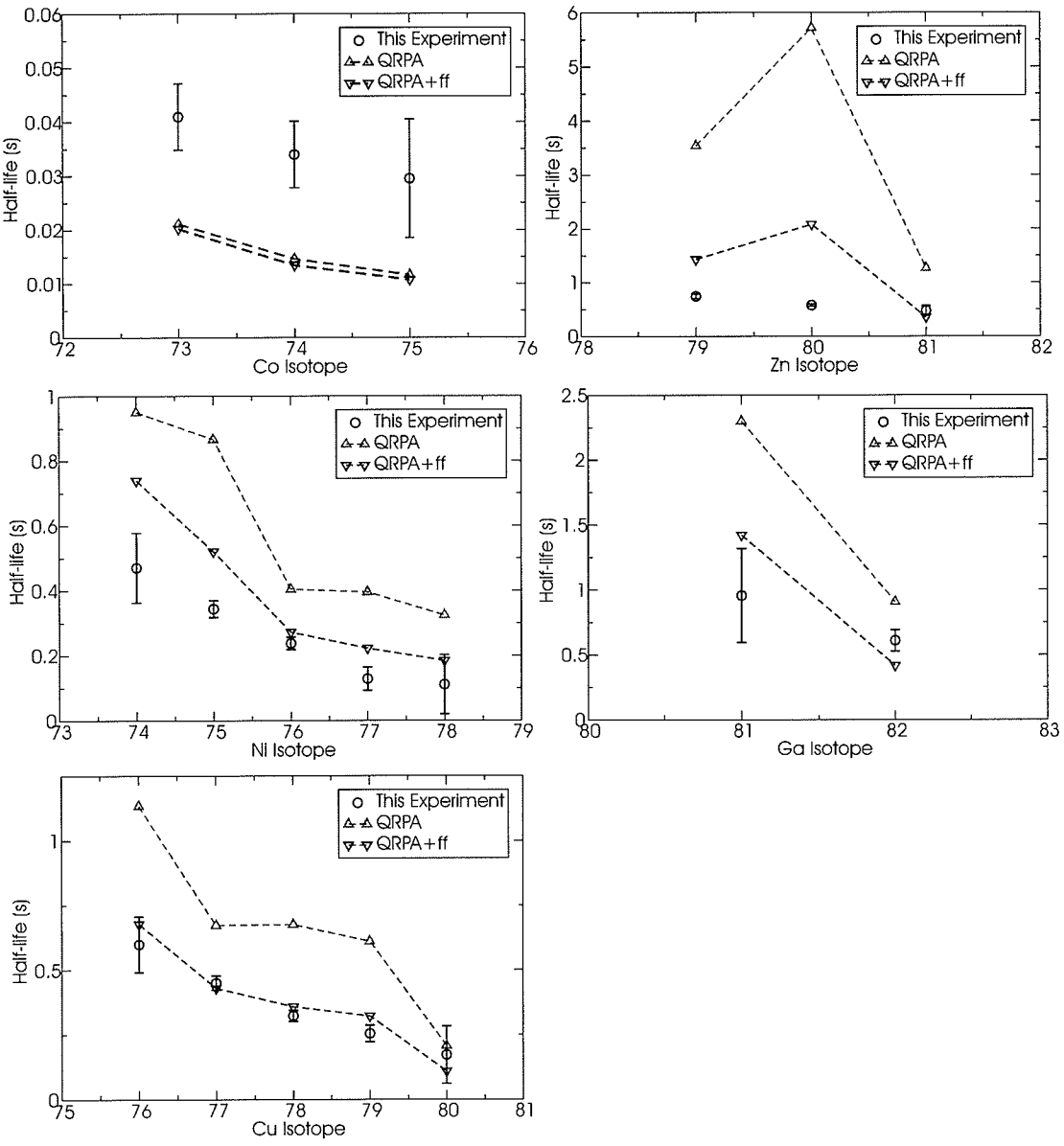

Figure 6.1: Comparison of half-lives from this experiment to QRPA calculations with allowed GT transitions and with allowed GT+ first-forbidden (ff) transitions.

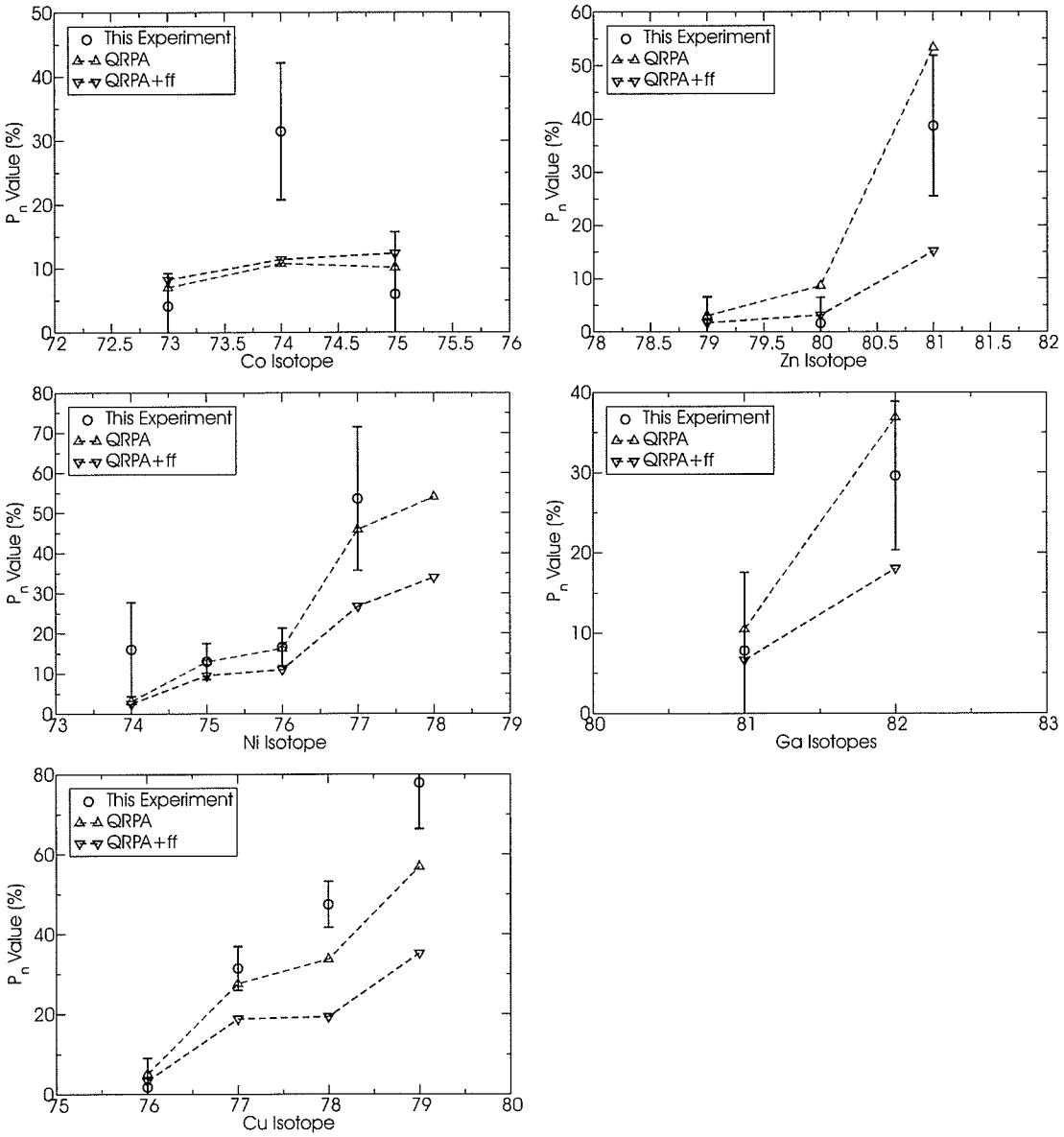

Figure 6.2: Comparison of P_n values from this experiment to QRPA calculations with allowed GT transitions and with allowed GT+ first-forbidden (ff) transitions.

Since the P_n values probe the transitions to higher-lying states, this is an indication that these calculations reproduce well the transitions to higher-lying states.

First-forbidden transitions were added heuristically to the QRPA calculations [67, 68]. As can be seen in the Figures, the resulting half-lives in general are shorter and are more in agreement with the experimental values. The P_n values also shift. When the first-forbidden transitions are added, the P_n values get smaller and consequently agree less with the experimental values, indicating too much strength is added below the neutron separation energy.

Another possible explanation for the longer half-lives in the calculation which only includes allowed transitions is that the predicted Q_β values may be too small. Due to the energy to the fifth power dependence of intensity ($I \propto (Q_\beta - E_x)^5$), the uncertanties in Q_β can be decisive. A smaller Q_β would result in a higher half-life, and a higher Q_β value would result in lower half-lives.

In conclusion there are several factors in the model calculation that affect the half-lives and P_n values. To answer which of these factors are mostly responsible for discrepencies between measurements and calculations may require detailed spectroscopy. However, here we showed that first-forbidden strength improves the half-life, but not the P_n values, thus suggesting that the lack of first-forbidden transitions does not seem to answer the problem of the discrepency between these calculations and the experimental half-lives. With just a measured half-life and without the measured P_n value, this result would be unnoticed. This example demonstrates that the combinded measurements of half-life and P_n values can be a powerful tool to study nuclear structure questions in exotic nuclei even with relatively low statistics.

6.2 The Case of ^{78}Ni

To examine these effects in more detail, consider the case of ^{78}Ni. Figure 6.3 shows the ^{78}Ni proton and neutron shell model configurations with the classic shell-model

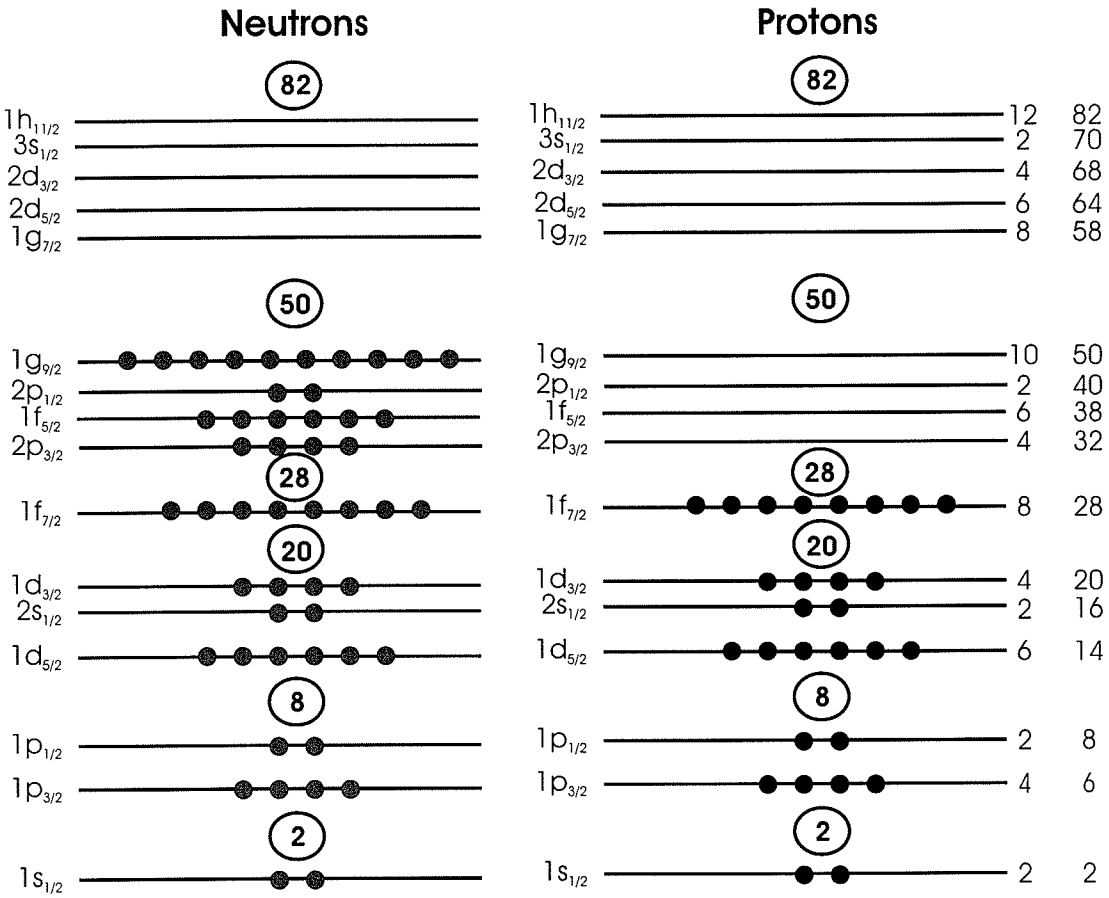

Figure 6.3: Proton and neutron configuration for ^{78}Ni according to the shell model.

gaps. Figure 6.4 shows the important transitions in the decay of ^{78}Ni to ^{78}Cu from the QRPA calculation. The $\nu p_{1/2}/\pi p_{3/2}$ transition dominates below the neutron separation energy. The $\nu g_{9/2}/\pi g_{9/2}$ transition is the main transition above the neutron separation energy. The grey region in the middle of the scheme represents the uncertainty in S_n. The $\nu f_{5/2}/\pi f_{7/2}$ transitions lie in this region. There are several considerations which effect the half-life. Assume the calculated half-life is too high. A general shifting of any of the levels upward will decrease the calculated half-life due to the energy dependence of the transition intensities. However, raising the $\nu p_{1/2}/\pi p_{3/2}$ or $\nu g_{9/2}/\pi g_{9/2}$ states, being the dominant states would have the greatest effect. One of the problems with comparing the half-lives is that raising one of the states could be compensated for by lowering the other state. Perhaps the $\nu p_{1/2}/\pi p_{3/2}$ is too high, but

the $\nu g_{9/2}/\pi g_{9/2}$ is too low, and the result is that this effect is cancelled out and the half-life is insensitive to the position of these levels.

The P_n value measurement, if it were available for ^{78}Ni, would offer additional insight. The P_n value is sensitive to the states above S_n. Here there is one dominant transition, the $\nu g_{9/2}/\pi g_{9/2}$, according to this calculation. In this case, without considering the possibility of an incorrect Q_β or S_n, a calculated P_n value that was high relative to measured value would most likely indicate that this level is too low. Another possibility is that one or more of the states in the vicinity of S_n slips below S_n. In this way, the P_n value can be sensitive to states within the vicinity of S_n. Finally , the P_n value is sensitive to the S_n. A too-high P_n value might indicate that S_n is too low and has slipped under the levels in the vicinity of S_n in the calculation, when it actually is above these levels.

This case along with the preceding discussion on first-forbidden transitions demonstrates how half-life and P_n value measurements, especially when both are available, can indeed offer some indications of the structure and first tests of theories. These tests can reveal discrepencies between theory and measurement and indicate where more detailed data such as mass measurements to determine Q_β and S_n values and/or spectroscopy to determine level structure will be needed.

6.3 Nuclear Shell Model

In order to better understand the nuclear structure in this mass region and to benchmark global models beyond the range of experimental data it is important to test the more sophisticated microscopic calculations, which have been performed for a limited set of singly- and doubly-magic heavy nuclei. The shell-model results of Reference [70] for ^{78}Ni are in good agreement with experimental data (see Fig. 6.5). Of course this does not necessarily mean that the shell-model description of this mass region is entirely correct. For example, as discussed in the previous section, deviations

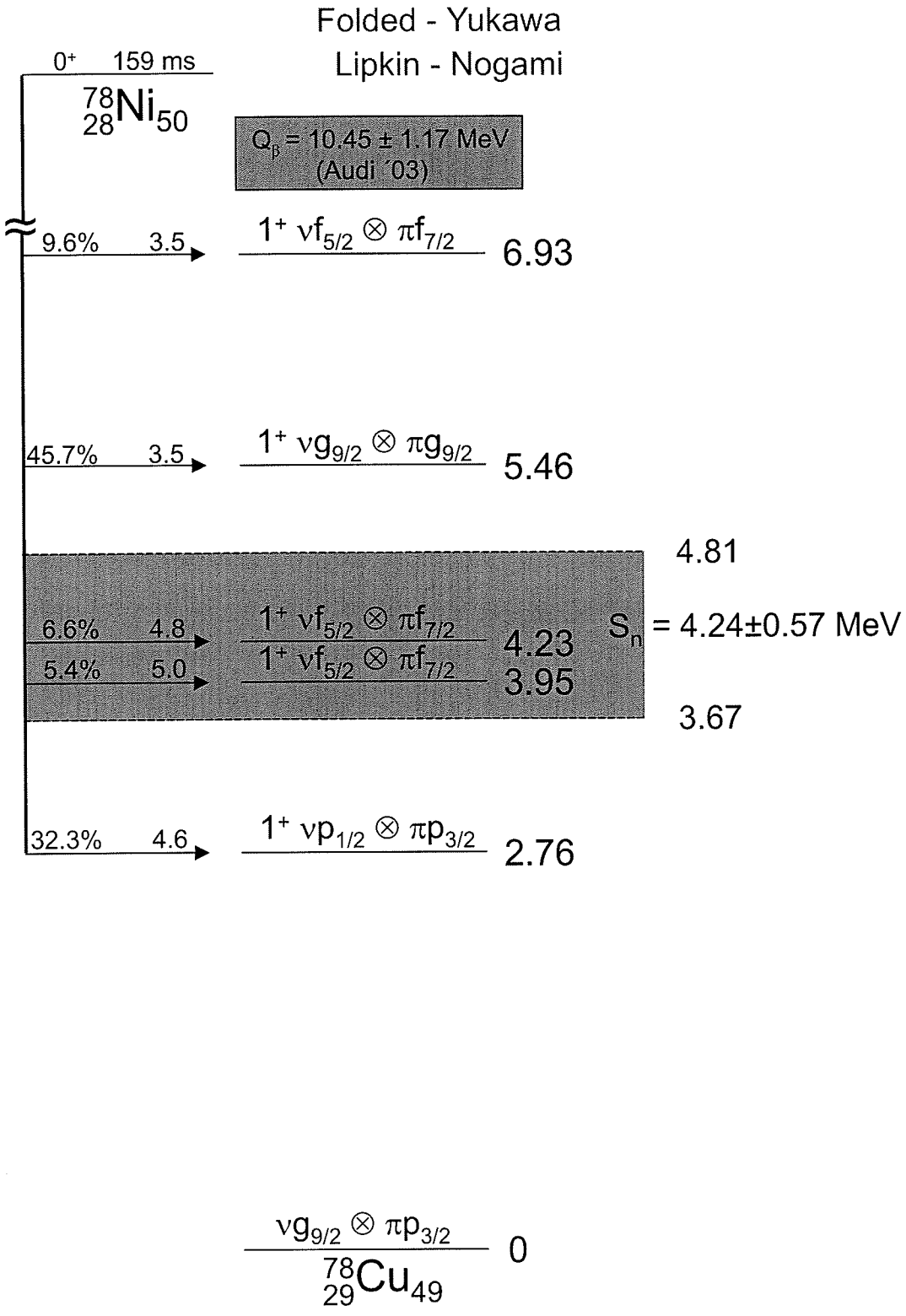

Figure 6.4: Important transitions in the decay of ^{78}Ni according to QRPA calculations.

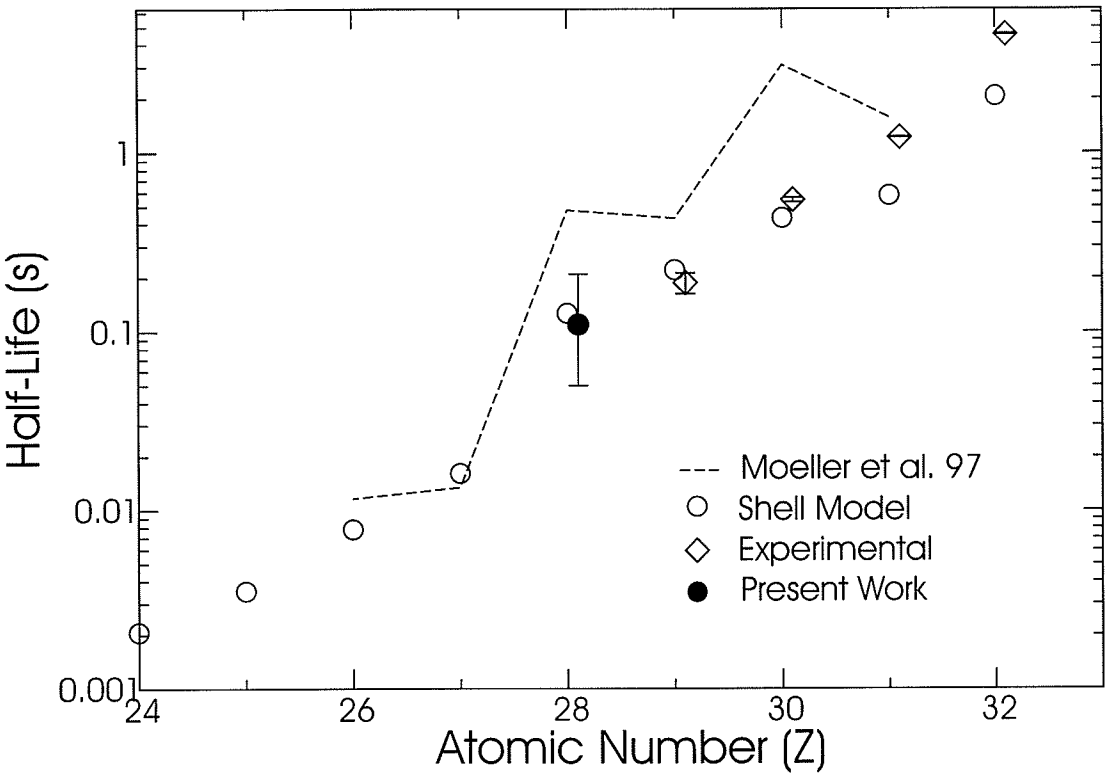

Figure 6.5: Experimental and theoretical halflives for N=50 isotones. Moeller *et al.* 97 [71], shell model of Ref [70], and previous work (NuDat).

in excitation energies, transition strengths, and decay Q-value can in principle compensate each other. The shell-model of Reference [70] did not include the proton or neutron $g_{9/2}$ orbitals, which for example carries a significant amount of strength for ^{78}Ni (see Fig. 6.4). Shell-model calculations which include these orbitals in the model space were carried out in this mass region at the NSCL by A. Lisetskiy [63, 64]. To model this mass range, one would like to assume an inert ^{40}Ca core and the full pf shell, including the intruder $g_{9/2}$ orbital. However, this makes the dimensions of the problem too large. Instead, one assumes an inert ^{56}Ni core and includes the smaller model space of the $p_{3/2}$, $f_{5/2}$, $p_{1/2}$, and $g_{9/2}$ orbitals.

To calculate β-decay properties such as $t_{1/2}$ and P_n values, one needs binding energies, spectra of the parent and daughter isotopes, and Gamow-Teller matrix elements. These were calculated using the code OXBASH. An effective interaction recently de-

rived from realistic G-matrix and adjusted to experimental data in this region was used [64]. Using the shell-model output, the half-lives and P_n values were calculated. The results are compared to the experimental results in Figure 6.6.

The good agreement with half-lives and P_n values indicates reasonable single-particle energies. However, very strong quenching is required to reproudce the half-lives. Usually for a full major oscillator shell, one requires a quenching of 0.7 to 0.8 for GT matrix elements. In this case, the $f_{7/2}$ orbital is missing, which is the spin-orbit partner of the $f_{5/2}$ orbital and is responsible for a large part of the sum rule for GT strengths. Furthermore, this configuration space includes the $g_{9/2}$ orbital but its partner $g_{7/2}$ is excluded from the space. This truncation of the configuration space results in a GT sum rule that is only 50% of the Ikeda sum rule. Consequently, it requires a considerably smaller quenching factor (0.35), which means more quenching, for GT strengths. This factor was chosen to reproduce the half-lives of $^{75\text{-}77}$Ni (Figure 6.6). It can be seen in that figure that this quenching factor works well also for the Cu isotopes, so it seems to be the proper quenching factor for this mass region and model space. The good agreement with P_n values is an indicator of correct distribution of higher-lying GT strengths in the daughter nuclei. It also supports the choice of single-particle energies.

With the interaction and quenching adjusted to fit the present results, these measurements provide an important basis for nuclear structure calculations in this region of the nuclear chart. The fact that both the P_n values and half-lives are well reproduced by the shell-model calculation which only includes GT transitions casts further doubt on the relevance of the first-forbidden transitions in these decays.

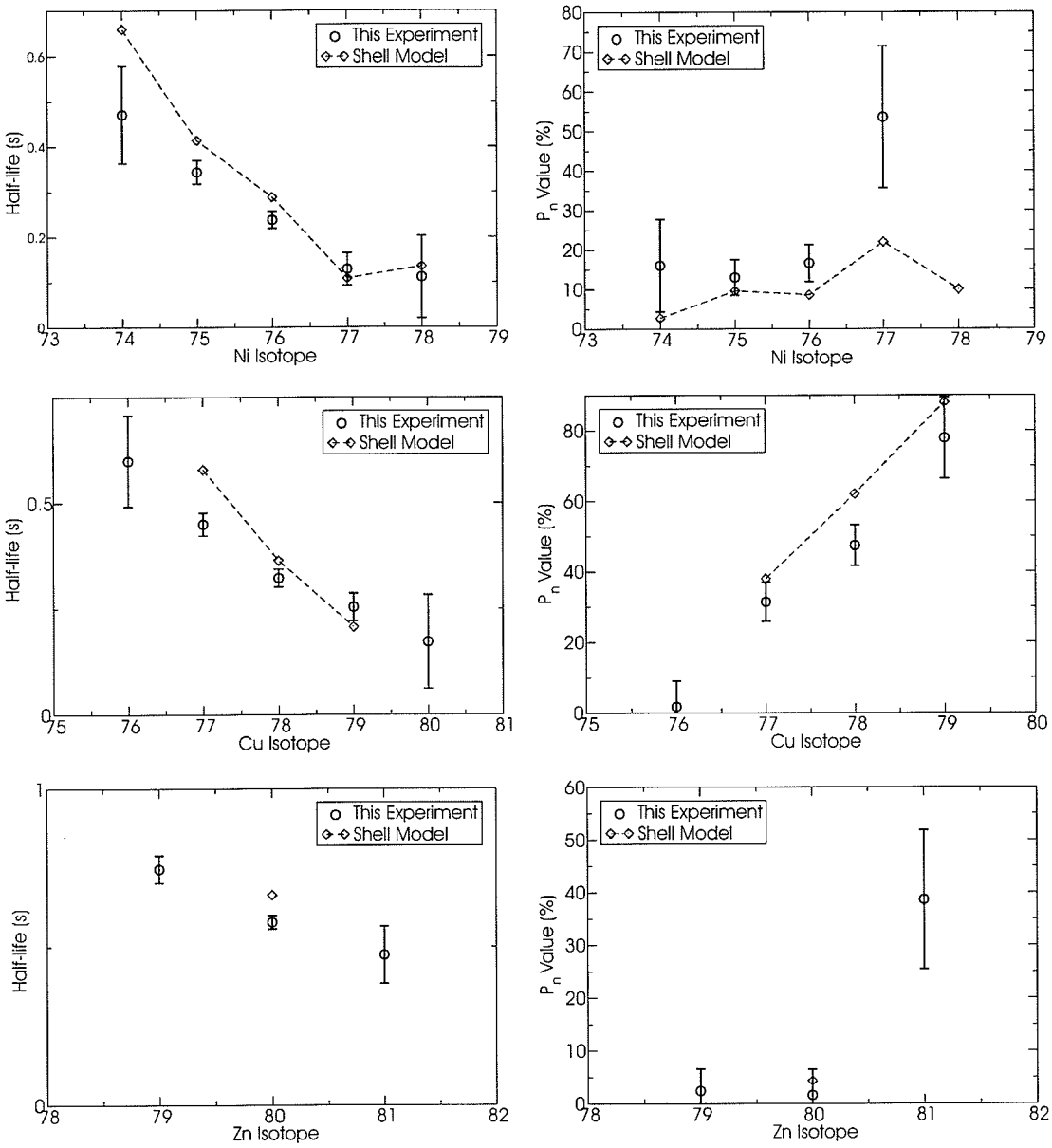

Figure 6.6: Comparison of half-lives and P_n values from this experiment to shell-model calculations.

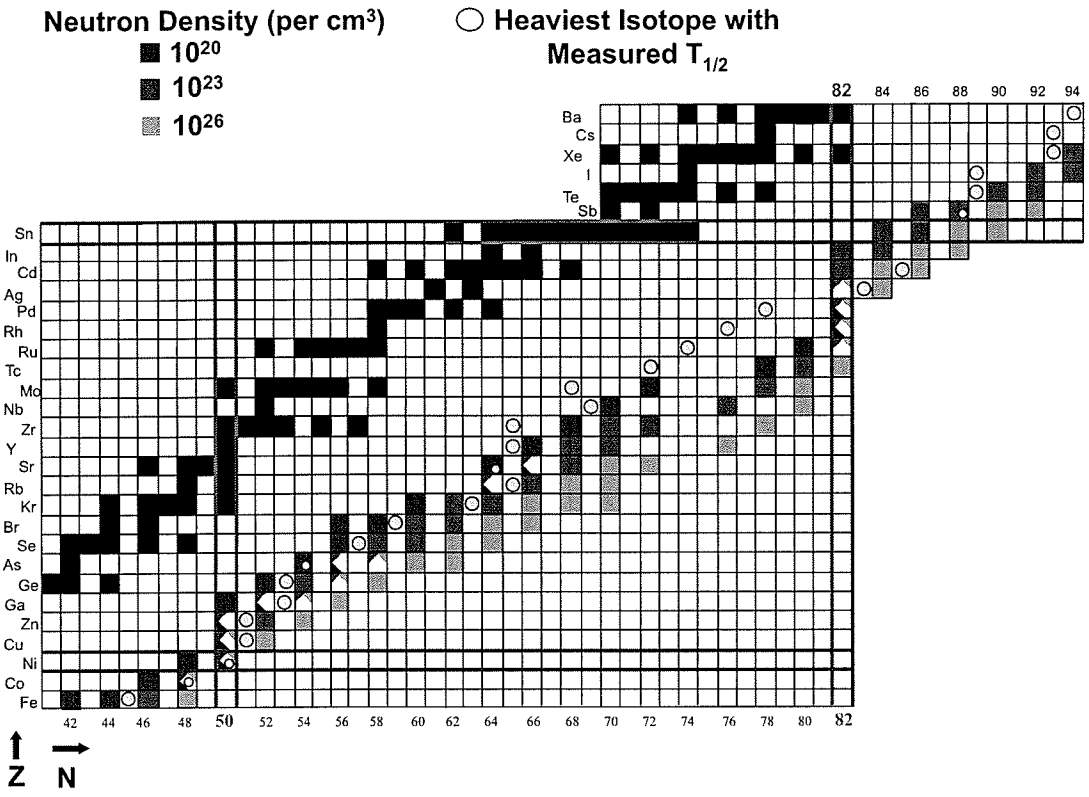

Figure 6.7: R-process waiting points for three different neutron densities [68].

6.4 The r-Process

6.4.1 Measurements Relevent to the r-Process

Figure 6.7 shows calculated r-process waiting points for three different neutron densities [68]. The waiting points whose half-lives were measured in this experiment are ^{73}Co and ^{75}Co, ^{76}Ni and ^{78}Ni,^{79}Cu, ^{80}Zn, and ^{81}Ga, with new half-life measurements for ^{75}Co and ^{78}Ni. According to this calculation, all the P_n values measured in this experiment will be relevant in the r-process freeze-out. The new relevant P_n value measurements from this experiment are $^{73\text{-}75}$Co and $^{74\text{-}76}$Ni. (P_n values are not important *during* the r-process as they are reversed by neutron capture.)

6.4.2 r-process code

To test the impact of the new measurements a classical r-process code was used (see for example Ref [11]). Inputs into the code include the astrophysical conditions of temperature T and neutron density n_n, and a time duration τ for those conditions. The nuclear structure inputs include the neutron seperation energies S_n, decay constants (half-lives) λ, and neutron emission probabilities P_n. Given a temperature T, neutron density n_n, and set of neutron separation energies S_n, the code calculates the relative abundance distribution across an isotopic chain as described in Chapter 1:

$$\frac{Y(Z,A+1)}{Y(Z,A)} = n_n \frac{G(Z,A+1)}{2G(Z,A)} \left(\frac{A+1}{A}\frac{2\pi\hbar^2}{m_u kT}\right)^{3/2} exp\left(\frac{S_n}{kT}\right) \tag{6.1}$$

where $Y(Z,A)$ is the abundance of nucleus with proton number Z and mass number A and G are the partition functions, which are set equal to 1. Given the decay constants for the isotopes in this chain, the code then follows the movement of mass up to higher mass. Finally, the abundance distribution at the end of time τ is adjusted to account for decay processes during freezeout using the input neutron emission probabilities P_n.

6.5 Effect of ^{78}Ni Half-life

In order to test the sensitivity of the calculated r-process abundances to the half-life of ^{78}Ni, the code was run for a given set of measured and theoretically calculated half-lives, and astrophysical parameters were set to match the calculated abundance pattern to the solar system r-process pattern. The decay data used was from Möller *et al* 97 [71]. The neutron seperation energies were taken from experimental masses and the ETFSI-Q mass model where experimental or extrapolated masses were not available in Ref [69]. The fit to the observed abundance pattern required three weighted components shown in Table 6.1.

Table 6.1: r-process parameters.

Temperature (10^9 K)	Neutron Density (cm^{-3})	Time (s)	Weight Factor
1.35	1.0×10^{20}	2.00	9
1.35	5.0×10^{22}	1.80	1
1.35	1.5×10^{25}	1.65	0.75

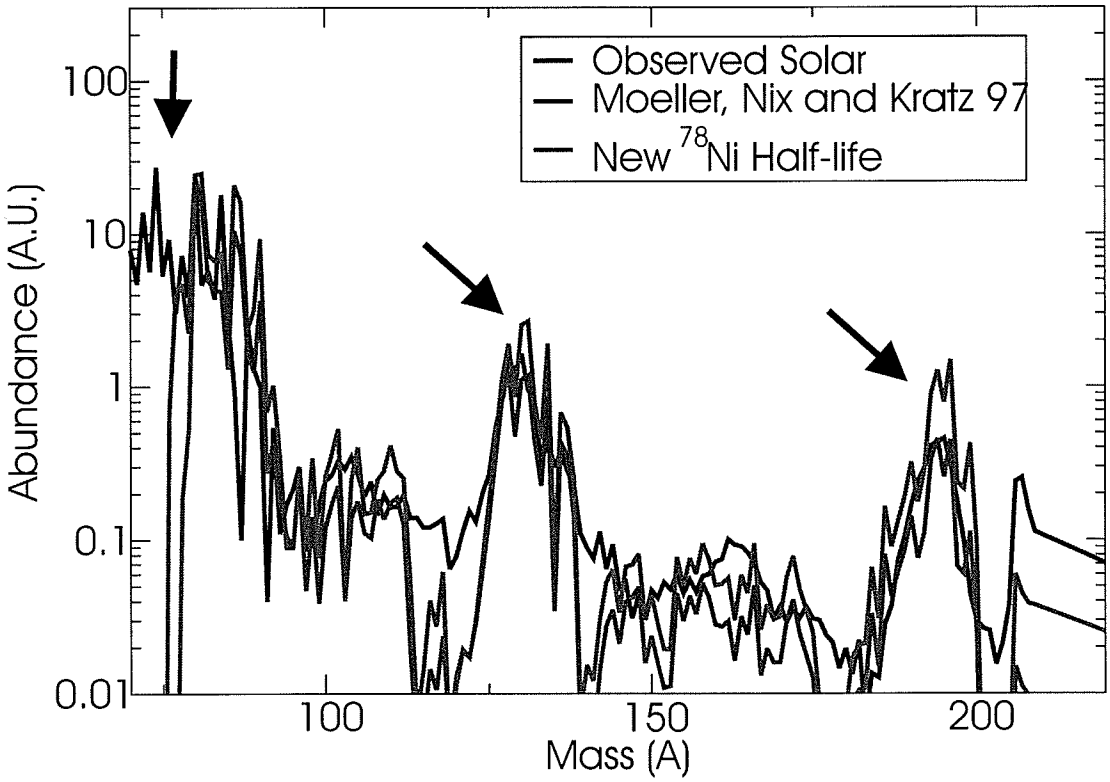

Figure 6.8: Observed Solar Abundance, abundances using the half-lives according to Moller, Nix and Kratz 97, and abundances using the same half-lives except changing only the ^{78}Ni half-life to the new experimental value.

The half-life of only ^{78}Ni was then changed from the value from Möller *et al* 97 [71] of 477 ms to the new experimental value of 110 ms. Then the r-process calculation was run again with the same astrophysical parameters as before. The results are shown in Figure 6.8. One can clearly see that the different ^{78}Ni half-life has affected the abundance pattern all the way up to the highest r-process peak. At and around the $A = 78$ region there is less material, whereas at higher masses there is more material. Because the half-life of ^{78}Ni is shorter than expected, for the same amount of time the material has more time to process up to higher masses.

The astrophysical parameters now have to be adjusted, so that calculations with the new experimental data fit the observed abundance curve. For instance, some component should be shorter in time duration so as not to allow build-up of material at the higher mass peaks. This in essance means an acceleration of the r-process. With a shorter half-life, the material can move through the $N = 50$ bottle-neck faster. The fact that a change in only ^{78}Ni affects abundance throughout the process is a reflection of the fact that ^{78}Ni is indeed a bottle neck to the process for the assumed astrophysical parameters.

It must be stressed that the above discussion assumes that the r-process starts at Fe or lighter nuclei. This is currently not expected to be the case in some r-process scenarios as discussed in Chapter 1. However, these scenarios have problems producing the heaviest r-process nuclei as well as the abundance pattern in the $A = 80 - 90$ region, where they assume the seed. Models that try to address this problem have seeds below Fe and are characterized by neutron-capture flow through $N = 50$. In addition, in discussion of the possibility of a weak r-process which is responsible for the lighter r-process abundances this mass region would also play an important role.

6.6 Summary

In summary, we present the first results for the half-life of the r-process bottle neck ^{78}Ni as well as half-lives and P_n values for several other r-process waiting points. The P_n value measurements were made possible by the development of the low-energy neutron detector NERO. With these results, experimental half-lives are available for all but one (^{48}Ni) classical doubly-magic nuclei. Also, the half-lives of all important $N = 50$ waiting points in the r-process are now known experimentally. This will make r-process model predictions of the nucleosynthesis more reliable and comparison with observational data more meaningful. It will also put the overall delay that the $N = 50$ mass region imposes on the r-process flow towards heavier elements on

a more solid experimental basis. In this respect the half-life of ^{78}Ni is of special importance as during the initial stages of the r-process when the heavier nuclei are synthesized the r-process path passes through ^{78}Ni and ^{79}Cu rather than through the more stable $N = 50$ nuclei [72]. The delay timescale for the buildup of heavy elements beyond $N = 50$ is therefore set by the sum of the lifetimes of ^{78}Ni and ^{79}Cu. Our experimental data clearly favor the short timescale of 450 ms obtained with the prediction of Langanke and Martinez-Pinedo [70], or 233 ms predicted by the new shell-model calculations by Lisetskiy, over the much longer delays of 960 ms predicted for example by Möller *et al.* [71] leading to an acceleration of the r-process. This is in line with recent improvements in theoretical β-decay half-life predictions along the entire r-process path that also tend to result in shorter half-lives thereby speeding up the r-process [67].

In addition to the astrophysical implications, it was shown how these measurements of the gross β-decay properties of half-life and P_n value together can serve as first indicators of nuclear structure. In particular, the results suggest that the lack of first-forbidden transitions does not seem to answer the problem of the discrepency between these calculations and the experimental half-lives in this region, since although they improve the half-life results, the P_n results actually get worse, and the shell-model calculations which only assume allowed GT transitions reproduce well both half-lives and P_n values.

In addition, the measurements of β-decay properties in this region give shell-model calculations benchmarks in this neutron-rich region of the nuclear chart against which to test interactions which will help predict properties of these and other exotic nuclei.

Bibliography

[1] B.A. Brown. *Nucl. Phys. A*, **704**:11c, 2002.

[2] F.-K. Thielemann et al. *Phys. Rep.*, **227**:269, 1993.

[3] B. Pfeiffer et al. *Nucl. Phys. A*, **693**:282, 2001.

[4] S. E. Woosley and R. D. Hoffman. *Ap. J.*, **395**:202, 1992.

[5] C. Freiburghaus et al. *Ap. J.*, **525**:121, 1999.

[6] K. Takahashi, J. Witti, and H.-T. Janka.

[7] T. Terasawa et al. *Ap. J.*, **562**:470, 2001.

[8] S. Wanajo et al. *Ap. J.*, **593**:968, 2003.

[9] B. Pfeiffer et al., 1999. "The First Stars" Proceedings of the MPA/ESO Workshop held at Garching, Germany, 4-6 August 1999. Eds A. Weiss, T. G. Abel, and V. Hill. Springer, p148.

[10] C. Travaglio et al. *Ap. J.*, **601**:864, 2004.

[11] K.-L. Kratz et al. *Hyperfine Int*, **129**:185, 2000.

[12] K.-L. Kratz et al. *Z. Phys. A*, **325**:489, 1986.

[13] R.L. Gill et al. *Phys. Rev. Lett.*, **56**:1874, 1986.

[14] B. Ekström et al. *Physica Scripta*, **34**:614, 1986.

[15] E.M. Burbidge, G.R. Burbidge, W.A. Fowler, and F. Hoyle. *Rev. Mod. Phys.*, **29**:547, 1957.

[16] P.L.Reeder et al. *Phys. Rev. C*, **31**:1029, 1985.

[17] P.L. Reeder et al. Proceedings of the Specialists Meeting on Delayed Neutron Properties, edited by D.R. Weaver (Birmingham, England, 1986),p.37 ISNB 07044 03267.

[18] P. Armbruster et al. *Europhys. Lett.*, **4**:793, 1987.

[19] M. Bernas et al. *Z. Phys. A*, **336**:41, 1990.

[20] J.A. Winger et al. *Phys. Rev. C*, **36**:1976, 1989.

[21] J.A. Winger et al. *Phys. Rev. C*, **42**:954, 1990.

[22] E. Lund et al. Proceedings of the Fifth International Conference on Nuclei Far from Stability, Rosseau Lake, Ontario. AIP Conf.Proc. No. 164, edited by I.S. Towner (AIP, New York, 1988), p. 578.

[23] K.-L. Kratz et al. *Z. Phys. A*, **340**:419, 1991.

[24] M. Weber et al. *Z. Phys. A*, **343**:67, 1992.

[25] Ch. Engelmann et al. *Z. Phys. A*, **352**:351, 1995.

[26] M. Bernas et al. *Phys. Lett. B*, **415**:111, 1997.

[27] M. Bernas et al. *Nucl. Phys. A*, **616**:352c, 1997.

[28] F. Ameil et al. *Eur. Phys. J. A*, **1**:275, 1998.

[29] S. Franchoo et al. *Phys. Rev. Lett.*, **81**:3100, 1998.

[30] Glenn F. Knoll. *Radiation Detection and Measurement, 3rd. Ed.* Wiley, New York, 2000.

[31] T. Mehren et al. *Phys. Rev. Lett.*, **77**:458, 1996.

[32] J.C. Wang et al. *Phys. Lett. B*, **454**:1, 1999.

[33] P.L.Reeder, J.F. Wright, and L.J. Alquist. *Phys. Rev. C*, **15**:2108, 1977.

[34] P.L.Reeder et al. *Phys. Rev. C*, **44**:1435, 1991.

[35] P.R. Wrean and R.W. Kavanagh. *Phys. Rev. C*, **62**:055805, 2000.

[36] H. Franz et al. *Nucl. Instr. and Meth.*, **144**:253, 1977.

[37] P.L.Reeder, J.F. Wright, and L.J. Alquist. *Phys. Rev. C*, **15**:2098, 1977.

[38] P.L.Reeder and R.A. Warner. *Nucl. Instr. and Meth.*, **180**:173, 1981.

[39] A.B. Smith, P.R. Fields, and J.H. Roberts. *Phys. Rep.*, **108**:411, 1957.

[40] J. K. Blair and F. X. Haas. *Phys. Rev. C*, **7**:1356, 1973.

[41] T. R. Wang, R. B. Vogelaar, and R. W. Kavanagh. *Phys. Rev. C*, **43**:883, 1991.

[42] Kenneth S. Krane. *Introductory Nuclear Physics.* Wiley, New York, 1988.

[43] C.E. Rolfs and W.S. Rodney. *Cauldrons in the Cosmos.* University of Chicago Press, Chicago, 1988.

[44] C. R. Brune, I. Licot, and R. W. Kavanagh. *Phys. Rev. C*, **48**:3119, 1993.

[45] E. Lund et al. *Z. Phys. A*, **294**:233, 1980.

[46] E. Ramström and T. Wiedling. *Nucl. Phys. A*, **272**:259, 1976.

[47] K. Debertin and R.G. Helmer. *Gamma- and X-ray Spectrometry with Semiconductor Detectors.* Elsevier, New York, 1988.

[48] J.H. Hubbell and S.M. Seltzer, 1996. http://physics.nist.gov/PhysRefData/XrayMassCoef/cove

[49] S. Liddick. private communication.

[50] D. J. Morrissey et al. *Nucl. Instr. and Meth. B*, **204**:90, 2003.

[51] W.F. Mueller et al. *Nucl. Instr. and Meth. A*, **466**:492, 2001.

[52] Grzywacz et al. *Phys. Rev. Lett.*, **81**:766, 1998.

[53] J. I. Prisciandaro et al. *Nucl. Instr. and Meth. A*, **505**:140, 2003.

[54] N. Iwasa et al. *Nucl. Instr. and Meth. B*, **126**:284, 1997.

[55] K. Sümmerer and B. Blank. *Phys. Rev. C*, **61**:034607, 2000.

[56] John R. Taylor. *An Introduction to Error Analysis: The Study of Uncertainty in Physical Measurements, 2nd Ed.* University Science Books, Sausalito, 1997.

[57] R. Schneider et al. *Nucl. Phys. A*, **588**:191, 1995.

[58] K. Summerer et al. *Nucl. Phys. A*, **616**:341, 1997.

[59] T. Faestermann et al. *Eur. Phys. J. A*, **15**:185, 2002.

[60] A. Stolz, 2002. A Method of Maximum Likelihood for Analyzing Half-lives.

[61] P. Möller and J. Randrup. *Nucl. Phys. A*, **514**:1, 1990.

[62] B. Pfeiffer et al. *Prog. Nucl. Energy*, **41**:39, 2002.

[63] A.F. Lisetskiy. private communication.

[64] A.F. Lisetskiy et al. *Phys. Rev. C*, **70**:044314, 2004.

[65] U. Koester, 2000. Ph.D. Thesis, Munich.

[66] G. Rudstam et al. *ADNDT*, **53**:1, 1993.

[67] P. Möller, B. Pfeiffer, and K. L. Kratz. *Phys. Rev. C*, **67**:055802, 2003.

[68] K.-L. Kratz and B. Pfeiffer. private communication.

[69] G. Audi et al. *Nucl. Phys. A*, **729**:3, 2003.

[70] K. Langanke and G. Martinez-Pinedo.

[71] P. Möller, J. R. Nix, and K. L. Kratz.

[72] S. Wanajo. r-process movie at http://www.ph.sophia.ac.jp/ shinya/research/research.html.